SYNTHESIS OF METAL ORGANIC FRAMEWORK (MOF) IN SELECTIVE SENSOR DEVELOPMENT FOR TRACE DETECTION OF ARSENIC AND SOME MICROPOLLUTANTS

A THESIS SUBMITTED IN PARTIAL FULFILMENT OF THE REQUIREMENTS FOR THE DEGREE OF DOCTOR OF PHILOSOPHY

RICKY LALAWMPUIA

MZU REGISTRATION NUMBER: 4645 of 2013

Ph.D. REGISTRATION NUMBER: MZU/Ph.D./1247 of 09.08.2018

DEPARTMENT OF CHEMISTRY

SCHOOL OF PHYSICAL SCIENCES

JANUARY, 2025

SYNTHESIS OF METAL ORGANIC FRAMEWORK (MOF) IN SELECTIVE SENSOR DEVELOPMENT FOR TRACE DETECTION OF ARSENIC AND SOME MICROPOLLUTANTS

BY

RICKY LALAWMPUIA
Department of Chemistry

Under the supervision of
Prof. DIWAKAR TIWARI

Submitted

In partial fulfilment of the requirement of the Degree of Doctor of Philosophy in Chemistry of Mizoram University, Aizawl

MIZORAM UNIVERSITY
Department of Chemistry
(A DST-FIST Supported Department)
Tanhril, Aizawl, Mizoram. PIN: 796004

Thesis Certificate

This is to certify that the thesis entitled **'*Synthesis of metal organic framework (MOF) in selective sensor development for trace detection of arsenic and some micropollutants*'** submitted by ***Mr. Ricky Lalawmpuia*** for the degree of ***Doctor of Philosophy*** in the Mizoram University, Aizawl, Mizoram, embodies the record of original investigations carried out by her under my supervision. She has been duly registered and the thesis presented is worthy of being considered for the award of the Ph.D. degree. This work has not been submitted for any degree in any other university.

Dated: (Prof. DIWAKAR TIWARI)

Supervisor

Tanhril Campus, Aizawl 796004 Phone: 9862323015
Fax: (0389) 233 0834 E-mail: diw_tiwari@yahoo.com

DECLARATION OF THE CANDIDATE
Mizoram University
January, 2025

I, RICKY LALAWMPUIA, hereby declare that the subject matter of this thesis is the record of work done by me, that the contents of this thesis did not form basis of the award of any previous degree to me or to the best of my knowledge to anybody else, and that the thesis has not been submitted by me for any research degree in any other University/Institute.

This is being submitted to the Mizoram University for the degree of Doctor of Philosophy in Chemistry.

Dated: (RICKY LALAWMPUIA)
Candidate

(Prof. N. MOHONDAS SINGH) (Prof. DIWAKAR TIWARI)
Head Supervisor

ACKNOWLEDGEMENT

I give thanks to Almighty God for giving me the health, fortitude, and wisdom I need to do my task. This work would not have been feasible without his love and mercy.

I have great pleasure to express my heartfelt gratitude to my mentor and supervisor, *Prof. Diwakar Tiwari,* Department of Chemistry, Mizoram University. His dedication, genuine interest, and, most of all, his overwhelming attitude to assist his students had been solely responsible for the completion of my work. I admire his timely advice, scrutiny, and scientific approach, which have greatly aided me in completing this work.

I sincerely extend my thanks and grateful to *Prof. N. Mohondas Singh, Head, Department of Chemistry, MZU,* and other faculty members *viz., Prof. Muthukumaran, R., Dr. Zodinpuia Pachuau, Dr. A. Bimolini Devi, Dr. Manjeet Singh, Dr. Joydeep Das* and *Dr. R. Lalrempuia,* Dr. Lalhmunsiama for their unwavering support and insightful counsel throughout my time as a University Ph.D student. My heartfelt thanks go to *Dr. Lalhmunsiama* for his incentive and helpful suggestions in completing my research works.

I am grateful to acknowledge the close cooperation and support I received from all of my colleagues in the Department of Chemistry. I'd like to thank *Dr. J. Lalmalsawmi, Dr. R. Malsawmdawgnzela, Dr. Levia Lalthazuala, Dr. CVL Hmingmawia, Dr. Himangshu Dihingsia, Dr. Sarikokba, Dr. Ngainunsiami, Mr. Ricky Lalawmpuia, Ms. Melody Lalhruaitluangi, Ms. Swagata Goswami, Mr. Lalruatkima Ralte, Ms. Barsha Rabha, Ms. Hmingsangzuali Mr. Vanhmingliana, and Ms. Laldintluangi Khiangte,* for assisting me with my laboratory work. It is my pleasure to mention the assistance of *Mr. Brojendro Singh Shagolsem,* Sr. Laboratory Technician, and *Mr. John Vanlalhruaia,* Technical Assistant, Chemistry Department.

Lastly, my deepest gratitude to my parents and every member of my family for their love and support throughout my time pursuing the degree, as well as for their consolation and prayers, I truly love and appreciate them from the bottom of my heart.

(RICKY LALAWMPUIA)

TABLE OF CONTENTS

CHAPTER 4

LIST OF FIGURES

Scheme

Figure

3.10. Scan rate studies for redox couple $[Fe(CN)_6]^{3-/4-}$ (0.002 M; 0.1 M KCl) using the (a) bare GCE; (b) Ti-MOF/GCE; and (c) Zr-MOF/GCE.

3.11. Plots of the square root of scan rate ($v^{1/2}$) *vs* I_p (peak current; anodic peak current) using different electrodes (bare GCE, Ti-MOF/GCE, and Zr-MOF/GCE) [0.002 M $[Fe(CN)_6]^{3-/4-}$ (0.1 M KCl)].

3.12. Nyquist plots of bare GCE, Ti-MOF/GCE, and Zr-MOF/GCE with Z_{fit} modified GCE using the standard probe of $[Fe(CN)_6]^{3-/4-}$ (0.002 M; 0.1 M KCl) [Inset: Fitted equivalent circuit].

3.13. DPASV curves obtained for As(III) [25.0 µg/L at pH 3; acetate buffer (0.1 M)] using the bare GCE; and Ti-MOF/GCE.

3.14. Parametric studies carried out for the detection of As(III) (25.0 µg/L As(III)) and the oxidative peak current is represented as a function of (a) the pH; (b) Speciation of arsenic species; (c) deposition potential; and (d) the deposition time.

3.15. The differential pulse anodic stripping voltammograms are obtained for the As(III) concentration range (a) 0.2 to 1.0 µg/L; and (b) 5.0 to 25.0 µg/L; Insets: Calibration lines obtained for the oxidative peak current of As(III) at a concentration range of (a) 0.2 to 1.0 µg/L; and (b) 5.0 to 25.0 µg/L.

3.16. The detection of As(III) in the presence of several co-existing ions using the Ti-MOF/GCE ([As(III): 25.0 µg/L; [Interfering ion]: 250.0 µg/L).

3.17. The detection of As(III) for different time intervals using the Ti-MOF/GCE (As(III): 25.0 µg/L, pH 3.0).

3.18. Real water sample spiked with As(III) having concentrations from 5.0 to 25.0 µg/L (Acetate buffer 0.1 M; pH 3), DPASV of As(III) using the groundwater; Inset: Calibration lines obtained for groundwater samples.

3.19. (a) DPASV curves obtained for Pb(II) (25.0 µg/L at pH 4.5; acetate buffer (0.1 M)) using the bare GCE and Ti-MOF/GCE; (b) DPASV curves obtained for

Cd(II) (25.0 µg/L at pH 4.5; acetate buffer (0.1 M)) using the bare GCE and Ti-MOF/GCE.

3.20. (a) Effect of pH in the electrochemical detection of Pb(II) and Cd(II) (each 25.0 µg/L) in the Pb(II) & Cd(II) in 0.1 M acetate buffer; (b) Speciation of Cd(II); (c) Speciation of Pb(II).

3.21. The dependence of oxidative peak current for Pb(II) and Cd(II) (each 25.0 µg/L in 0.1 M acetate buffer; pH 4.5) as a function of deposition potential.

3.22. Parametric studies carried out at 25.0 µg/L Pb(II) & Cd(II) (0.1 M acetate buffer; pH 4.5); The oxidative peak current of Pb(II) & Cd(II) as a function of time.

3.23. The DPASV of Pb(II) as a function of Pb(II) concentrations; [Inset: Calibration line obtained for the oxidative peak current of Pb(II) as a function of Pb(II) concentration].

3.24. The DPASV of Cd(II) as a function of Cd(II) concentrations; Inset: Calibration line obtained for the oxidative peak current of Cd(II) as a function of Cd(II) concentration.

3.25. The simultaneous detection of Pb(II) and Cd(II) at varied concentrations of Pb(II) and Cd(II) concentrations; [Inset: Calibration lines obtained for the oxidative peak currents of Pb(II) and Cd(II) vs Pb(II) and Cd(II) concentrations].

3.26. The detection of Pb(II) and Cd(II) in the presence of several co-existing ions using the Ti-MOF/GCE probe ([Pb(II) and Cd(II)]: 25.0 µg/L; [Interfering ion]: 250.0 µg/L.

3.27. Real water sample spiked with Pb(II) and Cd(II) concentrations from 5.0 to 25.0 µg/L; Inset: Calibration line obtained for the oxidative peak current of Pb(II) and Cd(II) using the Tlawng river water.

3.28. (a) DPASV curves for (a) CFX; and (b) CBZ ((CFX/CBZ): 50.0 µg/L at pH 7.0; phosphate buffer (0.1 M)) using the bare GCE and Zr-MOF/GCE.

3.29. Parametric studies carried out for the detection of CFX and CBZ (50.0 µg/L) (a) the pH values; (b) Speciation of CFX; (c) Speciation of CBZ; (d) deposition potential; and (e) deposition time.

3.30. (a)The DPASV of CFX as a function of CFX concentrations; Inset: Calibration line obtained for the oxidative peak current of CFX as a function of CFX concentration; (b) The DPASV of CBZ as a function of CBZ concentrations; [Inset: Calibration line obtained for the oxidative peak current of CBZ as a function of CBZ concentration].

3.31. The detection of CFX and CBZ in the presence of several interfering ions using the Zr-MOF/GCE

3.32. The detection of (a) Ciprofloxacin; and (b) Carbamazepine for different time intervals using the Zr-MOF/GCE.

3.33. (a) DPASV of CFX using the groundwater; (Inset) Calibration lines obtained for groundwater; (b) DPASV of CBZ using the groundwater; and (Inset) Calibration lines obtained for groundwater.

LIST OF TABLES

Table

CHAPTER 1

INTRODUCTION

1. INTRODUCTION

1.1 BACKGROUND

A report states that the consumption of deleterious quality water afflicts *Ca.* 2.4 billion individuals around the globe, and poses greater (Hendon et al., 2013) threats of waterborne diseases such as cholera, typhoid fever, and other waterborne ailments (du Plessis, 2022). Additionally, more than 1.1 billion people are deprived of accessing the clean drinking water (Qamar et al., 2022). Annually, *Ca.* 2 million individuals suffer from diarrheal illnesses, with the majority of victims being children (Paraschiv et al., 2023). Water is susceptible to contamination, leading to various environmental and ecological concerns. However, natural water contains several essential minerals or substances which are known to be essential for sustaining life. However, exceeding the permissible limit of these substances led to detrimental effects on human health and the ecology (Samsudin et al., 2020).

The swift escalation of industrialization, uncontrolled urbanization, and global population expansion caused various global concerns, which have detrimental effects on the environment and pose a serious threat to human health (Werber et al., 2016). Water contamination is attributed to both natural and anthropogenic sources. Human activities have significantly contributed to the detrimental of water quality (Wu et al., 2021). Broadly water contamination consists of three categories of toxins: inorganic, organic, and microbiological pollutants. Inorganic pollutants include harmful heavy metals, acid-base salts, and radioactive compounds. Organic pollutants consist of pesticides, medications, and chemical commodities. Microbiological pollutants refer to the bacteria and viruses (Wu et al., 2021). Topographical, lithological, hydrological, atmospheric, and climatic factors are examples of natural variables that affect water quality (Magesh et al., 2013). The extent of contamination and pollution varies on the use of water. Water bodies close to the heavy metal industrial zone especially receive the discharge of hazardous chemicals including heavy metals in their industrial processes (Yousefi et al., 2018). Wetlands and water sources close to agricultural areas receive the fertilizers and chemical remnants. Statistics indicate that 25% of the global

population does not have access to clean water, while 50% lacks access to fundamental sanitation services (Chowdhury et al., 2012).

Industrial growth in developing-countries releases a large amount of wastewater containing heavy metals, which are typically received into the neighbouring surface water, endangering human health and environmental sustainability (Rahim et al., 2021). Because of their hazardous effects, endurance in the environment, and bio accumulative nature, heavy metals are considered potential environmental contaminants. Cr, Ni, Cu, Zn, As, Pb, Hg, and Cd are the most dangerous heavy metals and metalloids in the environment. These heavy metals pollute surface water, potential for ecological imbalances (Ali et al., 2019). Heavy metals in the environment, particularly the surface water, are poisonous and harmful to agriculture, animals, and humans even in trace quantities. The level of heavy metals beyond threshold levels causes bioaccumulation in the biota of riverine habitats, which harms animals and the human population consuming this contaminated water (Kubra et al., 2022). Heavy metals are also reported to be potent neurotoxins in fish species, causing abnormalities in both laboratory and natural populations (Hossain et al., 2020). Depending on the quantity and length of exposure, several heavy metals have carcinogenic, mutagenic, and teratogenic effects on various species. As a result, these metals penetrate the food chain and represent an important source of human exposure. The “lifeblood of the biosphere” is water. However, both inorganic and organic pollutants endanger the biosphere’s lifeblood, as water is a universal solvent that dissolves these pollutants (Kubra et al., 2022).

Substances or molecules that are synthetic and endanger the environment, and animal and human health, are known as emerging pollutants. Synthetic organic compounds and heavy metals interfere the natural biological processes and show detrimental physiological impacts on both humans and animals. Emerging toxins mostly come from chemicals that are essential to the expansion and development of modern society, and they lack established health standards (Madivoli et al., 2020). Antibiotics, steroids, and antiviral drugs pose a major threat to the environment and human health. These growing micropollutants, particularly antibiotics, help to spread antimicrobial resistance among environmental bacteria (Ngumba et al., 2016). According to research, current wastewater treatment procedures are unbale to

completely remove these compounds and the effluents of these wastewater treatment plants contain minute quantities of these micro-pollutants. Therefore, the escaped micro-pollutants through the effluents contaminates the water bodies. Hence, the newer solutions for effectively and efficiently removing these pollutants from surface waterways are needed, as they constitute an existential threat to the human civilizations (Rogowska et al., 2020).

A wide range of methods, such as high-performance liquid chromatography, gas chromatography, electrochemical method, fiber-optical chemo-sensing method, inductively coupled plasma mass spectrometry, chemiluminescence, atomic absorption spectrometry, and micro-solid phase extraction is employed in the detection of these organic micropollutants and toxic metal ions. Nevertheless, the majority of these procedures require complex sample pre-treatment, expensive instrumentation, time-consuming, etc. (Liang et al., 2023). Moreover, these techniques are seemingly inappropriate for on-site detection of these pollutants. On the other hand, the electrochemical methods are cost-effective and offer several advantages, including rapid detection, quick analysis time, good selectivity, exceptional sensitivity, and a wide range of outputs. To develop a cost-effective, sensitive, and selective electrochemical method for the determination of a target analyte, suitable materials are preferred for miniatured device development (Yadav et al., 2016).

Metal-Organic Framework (MOF) constitutes ordered porous materials that are potential materials in diverse applications *viz.*, catalyst, sensing and imaging, optoelectronics, drug storage and delivery, gas separation, and energy storage. In general, MOFs possess a large interior surface area with structured pores and are derived using simple and high-yielding methods (Hosseini et al., 2013). MOFs exhibit several advantages compared to traditional porous materials, primarily due to their high surface area, efficient pore functionality, tuneable form, and precise pore size achieved through the employment of appropriate organic linkers during their synthesis (Li et al., 1999). MOFs have shown potential in electrochemical sensing techniques for detecting micro-pollutants and heavy metals in aquatic environments (Sohrabi et al., 2023). Initially, the divalent cations of transition metals such as zinc, cobalt, and copper derive the MOF's structure using a variety of linkers. This included MOF-5, HKUST-1, ZIF-8, etc. Alkaline earth metals, transition metals, lanthanides, and other

metal ions (Mg, Ca, Al, Ti, Cr, Mn, Fe, Co, Ni, Cu, Zn, Zr, Cd, Pr, La, and Bi) serve as inorganic nodes in the synthesis of various MOFs. The commonly utilized organic ligands (POLs) are imidazole, triazoles, and bi- and tridentate carboxylic acids. MOF structures constitute the metallic bonds with oxo, carboxylate, and non-metallic sites, which are referred to as secondary building units (SBUs) (Ha et al., 2019). The coordination geometry of MOF is determined by the type of building units in the MOF frame, and classified as square, pyramidal, trigonal, bipyramidal, tetrahedral, or octahedral geometry (Fan et al., 2022; Yuan et al., 2018). The use of divalent transition metals facilitates the crystallization process of the MOF. However, the divalent cations exhibit various drawbacks, including limited hydrothermal stability, and restricted the annealing of materials (Chui et al., 1999). On the other hand, the thermodynamic investigations revealed that metal cations with larger charges exhibit robust metal-ligand interactions, hence greatly improving the hydrothermal stability of MOFs (Devic & Serre, 2014). The stability of the MOF is enhanced in the presence of metal ions with higher valency, such as iron (Fe), aluminum (Al), zirconium (Zr), and titanium (Ti). This suggests that metal ions with higher valency states exhibit stability compared to divalent metal cations like zinc (Zn), copper (Cu), and cobalt (Co) (Jomova et al., 2022).

The utilization of MOFs in electroanalytical techniques is meager. Nevertheless, the MOFs are, perhaps, useful materials in the detection of several analytes or biomolecules in diverse matrices (Jung et al., 2018). The MOFs allow the creation of tailored materials that have a wide range of uses in various research fields. Therefore, the MOFs and MOF-derived materials are suitable modifiers of electrodes for detecting different water contaminants (Kajal et al., 2022). Moreover, using suitable organic linkers in the material synthesis makes the material a flexible framework for the target analyte molecules. Therefore, potential lies in creating MOF ’s-based sensing devices by enhancing the materials' sensitivity and stability. Further, the use of MOFs in the development of sensor devices encounters several challenges such as:

I. The synthesis of intricate materials to manipulate the form and dimensions of MOFs; might lead to the consistent development of nanostructures with a notable augmentation in surface area.

II. It is still challenging to distribute active metals evenly on the surface of carbons made from MOFs.

III. Although many MOFs employed fabricating the electrodes for heavy metal detection, the insights into electrochemical sensing mechanisms could enable greater implications for device development.

IV. MOF stability in an aqueous media remains challenging; studies on coupling hydrophobic ligands with high valence metal ions could provide newer research areas for suitable applications.

V. Since MOF's pore width and geometry play crucial roles in the highly selective determination of various contaminants, synthesizing functionalized MOFs could enable the required selectivity towards the target analyte species in complex matrices.

1.2. FATE OF POLLUTANT AND THEIR TOXICITY

Heavy metals are the major source of pollution in aquatic habitats since they easily enter into the food chain of aquatic ecosystems. Heavy metals are adversely impacting the aquatic ecosystem and pose a significant hazard due to their harmful effects on humans and livestock. Heavy metals entered the sediments by chemical and physical rock processing, soil percolation, and physiological processes of diverse plants. In addition to urbanization, industrial and agricultural activities contribute significantly to the heavy metal contamination of soil (Pandiyan et al., 2021). Emerging water contaminants primarily include pharmaceuticals, personal care items, endocrine disruptors, biocides, and poly-fluoroalkyl compounds. Long-term exposure to trace quantities of micropollutants has several harmful effects on human health (Ren et al., 2022). The occurrence and fate of heavy metal toxic ions like As(III), Cd(II), and Pb(II) and micro-pollutants such as ciprofloxacin (CFX) and carbamazepine (CBZ) are summarized in proceeding sections separately.

1.2.1 Arsenic

The bioaccumulation of heavy metal toxic ions in food chains is currently posing an increased health concern. Heavy metal pollution is primarily due to anthropogenic activities such as metal processing in refineries, coal combustion in power plants, petroleum combustion, wood preservation, nuclear power stations, high tension lines, plastics, textiles, microelectronics, and paper processing plants, along with the natural sources such as weathering and volcanic eruptions (Shi et al., 2020). These substances have immediate and severe health consequences, including cancer-causing effects such as squamous cell carcinoma, lung cancer, and bladder cancer, and some of the non-cancerous effects such as increased skin pigmentation, skin roughness, heart and brain diseases, diabetes, and respiratory difficulties (He et al., 2005).

Epidemiological studies demonstrate that arsenic exposure causes detrimental health impact that varies depending on the degree and duration of exposure. Arsenic toxicity affects *Ca.* 6 million people in India. The ground water of parts of Bangladesh, West Bengal, and Assam (India) is significantly contained with arsenic (Chowdhury et al., 2000). Prolonged exposure, even at lower amounts of arsenic in drinking water, leads to skin lesions such as hyperpigmentation, hyperkeratosis, and the growth of small warts or nodules. Moreover, arsenic exposure causes potential risks of numerous malignancies, including skin, lung, bladder, and kidney cancers. Moreover, arsenic causes cardiovascular illnesses such as hypertension and atherosclerosis (States et al., 2008). Severe arsenic poisoning occurs when individuals are exposed to high doses of arsenic, typically by ingestion or occupational exposure. Symptoms include intense abdominal discomfort, vomiting, diarrhea, cardiovascular complications, and, in severe cases, fatality. Chronic arsenic exposure causes neurological symptoms such as peripheral neuropathy, cognitive impairment, and developmental delays in children (Fatema et al., 2021). Therapeutic intervention, including the use of intravenous fluids to prevent dehydration and the injection of chelating medications to eliminate arsenic from the body, is commonly employed in its treatment. Long-term monitoring and extensive medical care are required to manage and treat arsenic poisoning (Lakkis et al., 2023). Chronic exposure causes the accumulation of arsenic in many organs,

including the liver, kidney, and lung, causing vital organ damage. Exposure to arsenic causes an increased risk of some malignancies, and tests may detect malignant growths in afflicted organs (Kaur et al., 2024).

1.2.2 Cadmium

The research shows that hazardous metal concentrations interfere with the function of the hepatic, renal, and central nervous systems via physiological processes and irreversible cellular alterations that culminate in necrosis (Callan et al., 2012; Liu et al., 2013). Elevated levels of heavy metals impact immune function, alter fertility, and induce endocrine disruption. Moreover, certain metals, like arsenic (As), cadmium (Cd), mercury (Hg), and lead (Pb), possess carcinogenic properties (Godt et al., 2006; Keil et al., 2011; Plum et al., 2010).

Cadmium is a common environmental contaminant that has harmful effects on various tissues and organs. Cadmium exposure occurs via eating contaminated food or drink, or by inhalation and smoking cigarettes (Genchi et al., 2020). The proximal tubule damage and chronic kidney diseases are commonly known as cadmium poisoning in humans and animals (Rafati-Rahimzadeh et al., 2017). The respiratory system is the primary route of cadmium absorption, with the gastrointestinal tract accounting for a minor portion of the absorption through the skin. Cadmium enters the body through the bloodstream, where it is absorbed by the kidneys, liver, and intestines after being carried there by erythrocytes and albumin (Satarug et al., 2018). The body excretes cadmium gradually through the kidneys, urine, saliva, and breast milk during breastfeeding. Exposure to cadmium causes a multitude of harmful effects in humans, including adrenal and hepatic dysfunction, testicular injury, and damage to the hemopoietic system and adrenal glands (Tinkov et al., 2018). There is a correlation between cadmium exposure markers (blood and urine) and peripheral artery disease, atherogenic lipid profile alterations, coronary heart disease, and stroke (Tellez-Plaza et al., 2013). The cadmium arsenite in yeast cells interferes with the folding of developing proteins, reducing cellular viability and likely contributing to several pathological circumstances, including age-related disorders, Alzheimer’s and Parkinson’s, and neurodegenerative diseases (Saturnino et al., 2014). Furthermore, cadmium exposure poses the risk of osteoporosis. It has also been shown that prenatal

cadmium exposure is linked to the development of the kidneys and cognitive function in fetuses (Buha et al., 2019). Studies examine the effects of cadmium on fetal kidney development or function, despite the evidence that this metal has nephrotoxic effects and can diffuse across the placenta through metal transporters such as DMT-1 (Divalent Metal Transporter-1), ZIP-14 (Zrt-Irt-like protein 14), and ZnT2 (Zinc Transporter-2). One of them shows that nephropathy and hypertension developed in rats at modest levels of cadmium in drinking water (Jacobo-Estrada et al., 2016).

1.2.3 Lead

Lead is ubiquitous in the environment, and has been an extremely poisonous element since ancient Roman times (Thompson et al., 2012). Lead possesses strong malleability, weak conductivity, ductility, a low melting point, softness, and corrosion resistance (Oprea et al., 2002). These features attracted for its widespread use in everyday activities (Liu et al., 2013). Due to its toxicity, the utilization of lead has been discontinued in various countries. However, it is still being used in many applications such as leaded pipe, solders, grids, battery manufacturing and recycling, and refining, which leads to a significant exposure of lead to humans. Lead exposure poses physiological problems in both adults and children. Children are extremely vulnerable to lead exposure due to the greater susceptibility of their soft tissues. Moreover, lead exposure to children results in behavioral issues, cognitive impairment, and a decline in IQ levels (Flora et al., 2012).

The Environmental Protection Agency (EPA) and World Health Organization (WHO) guidelines accept the maximum tolerable level of lead concentration in drinking water is 10.0 µg/L (Fort et al., 2015). Prolonged exposure to lead results in anemia, central nervous system impairment, hypertension in both elderly and middle-aged individuals, as well as kidney and liver damage. Excessive exposure to lead causes miscarriage and reduced fertility in humans (Abdel Moneim et al., 2011). Lead is absorbed into the body through ingestion or inhalation, which can disrupt biochemical function and accumulation in bones and kidneys, and causes severe damage to the central nervous system and renal function (Lin et al., 2003).

Most of the lead in the environment is concentrated in the uppermost humus layer of soil forming the organo-lead compounds. Lead largely immobilized toxic

metals in soil, regardless of soil pH. Furthermore, the emission of pollutants from industrial activities, the burning of fossil fuels, and the use of leaded gasoline in aviation contribute to the deposition of lead in the soil via the atmosphere. This phenomenon is particularly prevalent in urban soil (Masiol et al., 2014). Other sources of lead pollution include acid metal plating, old ammunition, leaded paints, ceramics, toys, tetraethyl lead production plants, dying industries, and glass industries (An et al., 2001).

1.2.4 Ciprofloxacin

In recent years, antibiotics have been extensively utilized in treating various diseases of humans and livestock (Yang et al., 2021). Furthermore, antibiotics are released into the environment by several means, including human and animal excretions, agricultural fertilizer, wastewater treatment plants, hospitals, and industrial emissions (Booth et al., 2020; Kraemer et al., 2019). As a result, the presence of pharmaceuticals in the waterbodies both surface and groundwater resources poses a health hazard to the marine ecosystem. Water-soluble antibiotics enter into the aquatic food chains, leading to the accumulation of these compounds in the biological system (Jin & Aslam, 2019). Nevertheless, the hospital and sewage wastewater contains a substantial quantity of persistent antibiotics that escape from the conventional treatment plants at low levels since not completely removed in such treatment plants and enter into the aquatic environment. Ciprofloxacin (CFX) is an extensively utilized antibiotic against both Gram-positive and Gram-negative bacteria (Li et al., 2023). In addition, ciprofloxacin inhibits DNA gyrase and exhibits a bioavailability rate ranging from 70% to 80%. However, the existence of industrial and pharmaceutical waste, presents substantial environmental hazards, leading to contamination of soil, air, and water (Balarabe et al., 2023).

The excessive build-up of antibiotics has adverse effects on both the environment and human health, including nephropathy and teratogenic mutations, and are classified as emerging contaminants (EC) (Chaturvedi et al., 2021). Under the existing regulatory system, there is inadequate monitoring of these pollutants, which creates a distinct threat to human health (Prieto-Rodriguez et al., 2012). Minimal concentrations of ciprofloxacin in drinking water induce symptoms such as nausea,

vomiting, and pain. Conversely, elevated levels of ciprofloxacin cause thrombocytopenia and kidney failure (Yoosefian et al., 2017).

1.2.5 Carbamazepine

Carbamazepine (CBZ) is widely prescribed anticonvulsant drug (Clara et al., 2004). CBZ residues enter into the surface waters via the discharge of wastewater treatment plants and leachates from landfills (industrial wastewaters) (Sörengård et al., 2019). CBZ is an effective drug in managing epilepsy, depression, and neurological disorders (He et al., 2020). The global consumption of CBZ is around 1000 tons per year and the *Ca.* 28% of administered doses of CBZ residue enter into the water bodies (Gao et al., 2018).

CBZ is an antiepileptic drug, often detected in wastewater treatment plants influents and effluents, surface waters, groundwater, and even in treated drinking water, with concentrations ranging from 0.03 to 11.6 μg/L (Xin et al., 2021). CBZ is a suitable anthropogenic marker of urban effluents because of its persistence (100 days) in both municipal wastewater and surface waters (Gao et al., 2024).

1.3 Review of Literature

Metal-organic framework (MOF) is a category of porous materials that has drawn greater interest in the recent past due to its widespread applications in diverse areas of research. The MOFs are primarily hybrid materials having organic and inorganic moieties. The organic linker comprises organic ligands in its structure, with the metal cluster acting as inorganic components. The MOF is designed with tenable porosity and functional groups at metal nodes using the functionalized organic linkers that enable the selectivity and reliability of materials for specific purposes, including electrochemical sensing (Ettlinger et al., 2022). The MOF shows varied applications in the area of gas adsorption, catalysis, optical storage media, drug delivery, sensing, separation, redox-active electrode materials, etc. due to its micro-to-meso porous structure, high surface area, and flexible structures (Zhang et al., 2017). Increasing the electrocatalytic signal by immobilizing the metal nanoparticles within the pores of

MOFs is advantageous, resulting in suitable and sensitive sensing of various analytes (Li et al., 1999).

The focus of research has gradually shifted from the studies on the structure and properties of MOFs towards the interaction between physical morphology, structure, and applications of these intriguing materials. Most MOFs are polydisperse microcrystalline powders and possess intrinsic limitations such as improper handling properties, slow mass transfer, and mechanical instability (Ren et al., 2015). A MOF packed in powder form within an adsorption column requires high pressure due to the gradual compression of MOF with pressure, and consequently an increase in mass resistance inside the column (Carrington et al., 2022). Moreover, using MOFs in powder form in catalysis frequently results in the recovery and recycling of catalysts. However, the MOFs showed numerous advantages over conventional porous materials because of their large surface area, pore working capabilities, regulated shape, and pore size due to using suitable organic linkers in material synthesis.

The MOFs are known hybrid materials with possible applications in electrochemical sensing techniques in detecting various micro-pollutants and heavy metals in aquatic environments (Ha et al., 2019). Initially, the MOFs are derived using the divalent cations of transition metals *viz*, zinc (Zn), cobalt (Co), copper (Cu), etc., which included MOF-5, HKUST-1, ZIF-8, etc. Alkaline earth metals (such as Mg, Ca, and Al), transition metals (Ti, Cr, Mn, Fe, Co, Ni, Cu, Zn, Zr, and Cd), lanthanides (such as Pr, La), and other metal ions (Bi) provide inorganic nodes in deriving a variety of MOFs. Organic ligands (POLs) such as imidazole, triazoles, and bi- and tridentate carboxylic acids synthesize the porous MOFs. Metal ions bind with the oxo, carboxylate, and non-metallic sites, known as secondary building units (SBUs) in the MOF structures (Li et al., 2023). According to the kind of building units in the MOF frame, the coordination geometry of MOFs defines the square, pyramidal, trigonal, bipyramidal, tetrahedral, and octahedral geometry (Yuan et al., 2018). The use of divalent transition metal ions makes easy crystallization of MOF; however, divalent cations showed several disadvantages, such as low hydrothermal stability that impacts the annealing of materials. Therefore, the selection of metal cations in the synthesis of MOF is crucial.

Further, the thermodynamic studies indicated that higher-charge metal cations possess strong metal-ligand bonds, significantly enhancing the MOF's hydrothermal stability (Devic et al., 2014). The stability of the MOF increases with increase in valency such as iron (Fe), aluminum (Al), zirconium (Zr), and titanium (Ti) are more stable than those of divalent metal cations such as zinc (Zn), copper (Cu) and cobalt (Co). In addition, aluminum is abundant on the Earth's crust, cheap, and lightweight, enabling large-scale production of MOF utilizing aluminum for varied applications such as adsorbent for pollutants removal, sensors, and storage material for gases (Loiseau et al., 2015).

Voltammetry and amperometry are the most reliable and efficient electroanalytical techniques for the qualitative and quantitative determination of several analytes at trace levels due to their reasonably high sensitivity, robust instrumentation, and relatively cost-effective compared to other spectroscopic or chromatographic techniques. In recent years, trace-level detection and measurements have drawn more attention using robust electrochemical techniques. With inexpensive instrumentation, it offers quick and reliable detection at ppb (parts per billion) to sub-ppb levels (Lee et al., 2016). Literature shows that these methods offer newer perspectives producing a straightforward device with many benefits like flexibility, biocompatibility, biodegradability, ease of use, a high surface-to-volume ratio, and affordability (Sarikokba et al., 2022). The core component of the electroanalytical techniques is the working electrode at which the analytes interact electrochemically. The electrodes fabricated with suitable materials enabled efficient oxidation or reduction of the analyte (Zirlianngura et al., 2017). The suitable and strategic electrode alterations enhance the sensing capabilities of the working electrodes (Tiwari et al., 2017). Many electrodes show poor surface kinetics and a significant decrease in selectivity and sensitivity, which causes difficulties in the detection of several analytes. Therefore, the fabrication of electrodes with high repeatability in their chemical and electrical properties and reproducible pre-treatment for a given target analyte are the parameters required for developing the miniaturized electrochemical sensor (Rana et al., 2019). The MOFs have a practical choice since it offers selective detection of analytes. However, designing an attractive and intriguing framework for detecting the target analytes or biomolecules in aqueous media is a challenging area of

research (Jung et al., 2018). The specific applications enable the design of suitable MOFs; hence, they are futuristic engineered materials with varied applications in diverse research areas.

Furthermore, MOF generally possesses unique properties such as large specific surface area, pore volume, molecular pore sizes, and flexibility of the framework that is accessible for the target ions/molecules. The application of MOFs in modifying carbon-based electrode studies for sensing and detecting several analytes in the literature. However, designing and fabricating the miniaturized device development utilizing the engineered metal-organic frameworks is the futuristic application of MOFs.

1.3.1 Synthesis of MOF

MOFs built from inorganic nodes and organic linkers attracted much interest because of their structural variety, rarity of properties, and capacity to customize for specific applications. The organic linkers and metal centers design the structure of MOFs appropriately; the organic linkers participate in shear connections, and the metal centers act as joints. There are several methods to synthesize MOFs, which are briefly discussed below:

(a) Hydrothermal/ Solvothermal Synthesis

Hydrothermal synthesis is typically adopted to produce sustainable metal-ligand bonds across the framework, which yields the most comprehensive dynamical products. Long-term heating of the reaction mixture at high pressure and temperature enables the hydrothermal synthesis of MOF (Abdelkareem et al., 2022). Based on the material's dissolution rate in hot water under intense vapor tension upheld at a temperature variation allying, the reactor's opposite nodes yield single crystals. Moreover, the 'solvothermal' process utilizes suitable solvents besides water in the material synthesis. The method results from the growth of high-quality crystals, but generally, hydrothermal/solvothermal processes necessitate elevated temperatures. The hydrothermal method synthesizes the Cu(4, 4′-bpy)NO_3(H_2O) crystals with

rectangular parallelepiped-shaped structure, utilizing the 4, 4′-bipyridine as a nitrogen donor aromatic ligand (Yaghi et al., 1995). Similarly, the hydrothermal method synthesizes the $[Cu_3(TMA)_2(H_2O)_3]_n$ complex known as HKUST-1 using the carboxylic functional group. The hydrothermal route by simple metal ions self-assembling at the adaptive bis-(imidazole) binding sites using the transition metals (cobalt, nickel, and zinc) synthesizes the MOFs having various applications (Qi et al., 2008). The hydrothermal reaction yielded a polycrystalline Fe-MIL-100 powder with a significantly large attainable and enduring porosity, demonstrating the Friedel-Crafts reaction with catalytic activity employing the redox properties of Fe(III) (Horcajada et al., 2007). Ni(II) is a typical transition metal ion with varied interest because of its inexpensive cost, high abundance, superior catalytic activity, and electrochemical characteristics. Ni-MOFs are synthesized by the hydrothermal process using Ni(II) and the 1,3,5-benzene tricarboxylate as a ligand (Liu et al., 2022). Nickel-based compounds with the proper design showed considerable potential for usage in the electrochemical industry as electrode surface modifications and electrocatalysts. The solvothermal method synthesizes the Mg-MOF-nNH_2 with double ligands. The metal center is magnesium, and the ligands are 2,5-dihydroxyterephthalic acid and 2-amino terephthalic acid. The micropore volume of Mg-MOF-1/8NH_2 measures 0.46 cm^3g^{-1} for these MOF samples. Additionally, the synthesized materials have a high specific surface area of 924.19 m^2g^{-1} (Lin et al., 2023). Similarly, a single-step solvothermal method obtains the Mn/Fe-MOF@Pd. The Mn^{2+} and Fe^{3+} are the metal sources of MOF, and Pd is doped within the MOF. The catalytic activity of Fe-MOF resembles that of an enzyme. Bimetallic active sites enhance the catalytic activity, and the presence of Pd further synergizes the acid tolerance and stability of the Mn/Fe-MOF solid (Deng et al., 2023).

(b) **Ultrasonic method**

Ultrasonic-assisted synthesis offers a relatively environment-friendly technique for MOF synthesis in an enclosed reaction condition (i.e., enclosed temperature and atmospheric pressure) with a shorter reaction time. Furthermore, the ultrasonication synthesis avoids safety concerns and follows the principle of green chemistry. Amongst some of the diverse MOF synthetic techniques, the ultrasonication method is affordable and environmentally benign. It could produce a high yield while operating under ambient temperature and pressure in a solvent-free reaction (Vinoth et al., 2017).

Compared to other methods, ultrasonic-aided MOF synthesis is containable and quickly produces the product with a significant yield. Ultrasonic cavitation for producing MOFs is relatively new and has attracted greater attention. In 2009, Khan et al. synthesized ultrasonically the $[Cu_3(TMA)_2(H_2O)_3]_n$ (also known as Cu-BTC MOF) (Khan et al., 2009). The ultrasonically assisted synthesis of MOFs significantly reduces the reaction time compared to the electronically controlled and microwave-irradiated methods. A limited sonication enables the shrinking of the size of the MOF particles; however, an increased sonication time from 6 to 45 min causes aggregation of the MOFs (He et al., 2021).

Sonochemical irradiation technique synthesizing the urea-containing metal-organic frameworks, i.e., TMU-31 and TMU-32. Further, various parameters, such as the initial reagent concentrations and irradiation periods, determine the morphology of MOF. The results reveal that these MOFs are homogeneous plate shapes at 0.005M concentration with a maximum power supply of 360W. Furthermore, phenol sensing was assessed and compared using these MOFs. The results indicate that hydrogen-bonding and packing interactions have a substantial role in detecting the phenol. Incorporating urea into the MOF structure is crucial for the framework's ability to detect phenol (Esrafili et al., 2017). Further, a sonochemical synthesis produces the high-purity uniform-sized Zr-based porphyrinic MOF-525 and MOF-545 using the tetrakis (4-carboxyphenyl) porphyrin and zirconyl chloride octahydrate (K. Yu et al., 2021).

Similarly, benzoic acid-modulated MOF-525 was obtained using the trifluoroacetic acid modulation (K. Yu et al., 2021). Solvothermal and sonochemical techniques synthesize the zinc-based MOF using adipic acid as an aliphatic diptotic linker. Ultrasonic irradiation enables MOF formation efficiency; also, the particle sizes shrunk due to ultrasonic irradiation. The samples' catalytic effectiveness was assessed using the electrochemical reduction of CO_2, with the only by-products being carbon monoxide and hydrogen (Vaitsis et al., 2022).

(c) Microwave-aided synthesis

Microwave-aided synthesis is an efficient approach that carries several chemical reactions. Compared to conventional solvothermal synthesis, microwave irradiation reduces the reaction time and enhances the crystal growth of porous materials that take several days or weeks in conventional methods (Joseph et al., 2021). The microwave irradiation energy, time of exposure, solvent concentration, and solvent choices are the key parameters regulating the yield and crystal growth of the MOFs. Microwave-assisted synthesis acknowledges rapid heating, fast kinetics, phase purity, improved dependability, and repeatability over hydrothermal synthesis (Jin et al., 2007). Additionally, it offers an effective method to regulate the distribution of macroscopic morphology, particle size, and phase selectivity during the synthesis of inorganic solids and nanocomposite materials (Škoda et al., 2019). Although the synthesis is much faster, the properties of the crystals produced by microwave-assisted methods are comparable to those produced by the conventional solvothermal process (Haque et al., 2011). Microwave-assisted approaches received interest in studying the effects of irradiation period, power, temperature, solvent concentration, and metal ion/organic linker ratio (Choi et al., 2008). The microwave-assisted synthesis produces the Zr-based MOF (Zr-fum-fcu-MOF), which has an octahedral shape at the reaction temperature of 100°C (Liu et al., 2021).

(d) Electrochemical synthesis

The electrochemical process of MOF synthesis possesses several advantages over other methods, including relatively short reaction time, robust equipment setup,

real-time MOF structure modification, quick synthesis, no necessity of precursor metal salts, and direct accumulation of MOFs on the preferred substrates, etc. (Ameloot et al., 2009). In addition to its simple process, the electrochemical synthesis of MOFs has provided numerous favorable pre-conditions, such as random and quick synthesis with lesser use of linker and solvent, excellent yield, and low energy consumption (Al-Kutubi et al., 2015). The mild reaction conditions, which perform at ambient temperature and pressure, are the most attractive feature of electrochemical synthesis. Despite these advantages, it is a less utilized approach, particularly in synthesizing functionalized framework materials. This approach also constantly altered the real-time response, enabling the direct output of crack-free nanostructures without a pre-treated surface at high temperatures.

On the other hand, relatively high reaction temperatures, longer reaction time, and thermal-induced cracking on the films are shown in the solvothermal or hydrothermal techniques. Electrochemically synthesized Zn-based MOF, and the physicochemical parameters, *viz*., reaction time, electrolyte quantity, current, and voltage, are optimized for greater solid yield. The results indicated that both reaction time and current density significantly impacted the purity and yield, and at an applied current of 60 mA and a reaction time of 2 h, yielded 87% of the product (Neto et al., 2019).

(e) Mechanochemical synthesis

Mechanochemical synthesis is an exciting chemical modification employed in obtaining high-purity MOFs (Du et al., 2021). Most coordination polymerization processes involving multisite ligands with metal ions proceed readily in a suitable solution environment. The solvent-free or solid-state formation of MOFs without any toxic or hazardous solvents has progressively received attention in recent years due to significant advances in mechanochemical synthesis (Chen et al., 2019). Coordination polymerization, broadly, involves the reaction in the presence of solution, multisite ligands, and metal ions. However, the mechanochemical synthesis of MOFs utilizes minimal solvents (Cheng et al., 2023).

Furthermore, compared to the diffusion and solvothermal methods, this technique is advantageous for large-scale MOF manufacturing in a shorter reaction

time and at room temperature. The solid-solid reaction has the potential to synthesize large-scale production of materials and provides simplicity in handling since it directly produces the products in powdered forms. Although mechanochemical synthesis is solvent-free or solvent-less, a solvent-based purification step is required. Despite this, the mechanochemical synthesis is reasonably environmentally friendly and commercially exciting for MOF production (Kaur et al., 2023). The liquid-assisted mechanochemical synthesis produces the MOF-5, showing that the solid possesses a relatively low BET surface area and contains many amide precursor by-products (Głowniak et al., 2021). A copper-based MOF with a product yield of 97% was synthesized in the mechanochemical process using the $Cu(OAc)_2.H_2O$ and H_3BTC at 30 Hz and 20 min of reaction time (Prochowicz et al., 2015). The framework structures produced by the mechanochemical method are easily separable from the host molecules, providing repeatable free pore access for additional uses. The mechanochemical synthesis of HKUST-1 and MOF-14 showed the method's applicability in efficient MOF production (Kujawa et al., 2021).

(f) Slow evaporation method

In the slow evaporation approach, reagent solutions are blended and allowed to undergo gradual evaporation. A critical concentration produces the crystals, facilitating deposition and subsequent crystal development. Since slow evaporation requires no external energy, it is a simple process for preparing MOF compounds. Nonetheless, this approach occasionally designs the MOF, but the primary disadvantage is that the crystal takes a long time to form. Slow evaporation may involve using a solvent combination to increase the starting material's solubility or a low-boiling solvent for faster evaporation (Halper et al., 2006).

A two-dimensional coordination polymer, denoted as CP-1, was synthesized using the slow evaporation technique. A reaction involving copper sulfate, 2-pyridine-methanol (hmpH), sodium thiocyanate, and sodium hydroxide in water is conducted (Khan et al., 2019).

(g) Diffusion method

In the diffusion method, the reagent solutions are either stacked atop one another with a solvent layer in between or undergo a gradual diffusion process facilitated by physical barriers. Occasionally, gels serve as both the medium for crystallization and diffusion. At the interface of these layers, crystals emerge following the gradual dissipation of the precipitating solvent into the subsequent layer. In particular, the diffusion approach is practical for limited soluble compounds. A technique combining ultrasonic and vapor phase diffusion was used for the rapid synthesis of $[Tb(1,3,5\text{-}BTC)]_n$, a terbium-based metal-organic framework (Min et al., 2020).

Compared to existing solvothermal and ultrasound-assisted approaches, this combined ultrasound-vapour phase diffusion strategy produces a nanoscale of $[Tb(1,3,5\text{-}BTC)]_n$ MOF crystals at a significantly higher rate. The nanocrystals exhibited remarkable specificity in detecting picric acid (PA), without any interference from other nitroaromatic compounds such as nitrobenzene, 2-nitrotoluene, 4-nitrotoluene, 2,4-dinitrotoluene, and 2,6-dinitrotoluene (Xiao et al., 2013).

(h) Template strategy

An alternative approach to MOF synthesis involves incorporating template molecules into the reaction mixture, a practice seldom seen in conventional synthetic methods, and this template synthesis technique is an effective tool for studying hierarchical porous materials (Zhang et al., 2015). Organic solvents are common template molecules that are often used in synthesis. Each template molecule exerts distinct influences on MOF's crystallization and synthesis processes. The solubility and polarity of the solvent are the primary factors influencing the crystallization of MOF (Chen et al., 2015). Organic amines influence the reaction's pH and make it easier for organic ligands to deprotonate. Using carboxylate groups as ligands allows the filling of MOF pores, while heterocyclic compounds act as counterions (Cohen, 2012). Surfactants produce micelles within solvents, controlling the shape and size of

the final MOFs, while ionic liquids serve as solvents and counterions (Feng et al., 2020).

(i) Microemulsion method

This method is widely employed in the production of nanoparticles and has recently found application in synthesizing MOFs. Water microemulsions having nanometre-sized water droplets sustained within the organic phase by a surfactant. The micelles in these microemulsions act as nanoreactors, regulating nucleation and crystal growth rates. The water-surfactant ratio and the surfactant type regulate the microemulsion's size and number of micelles. This approach provides exact control over the size of nanoscale materials. However, it comes with notable drawbacks, including high costs and the use of surfactants that are often environmental pollutants (Zhang et al., 2014). The microemulsion method synthesizes the zeolitic imidazolate framework-8 (ZIF-8), employing mild reaction conditions at standard temperature and pressure and a short reaction time. ZIF-8's amine groups react with the epoxy group, producing exceptional adhesion between ZIF-8 and the epoxy matrix. This prevented the overall ZIF-8 clustering and resulted in increased cross-linking densities (Duan et al., 2021).

1.3.2 Applications of MOF in electrochemical sensing

In electrochemical sensors, using MOF-modified electrodes in amperometric and voltammetric methods gained greater attention, particularly for detecting several pharmaceuticals, heavy metals, biomolecules, and other micro-pollutants. The MOF-based sensors showed a significantly low detection limit (LOD) and enhanced selectivity compared to several other advanced materials.

(i) Biomolecules sensing

The utilization of MOF-based biosensors showed greater interest in the field of biosensing for different diseases and biological disorders (Pandey et al., 2020). The Cu-MOF@Pt detects efficiently the glucose level in human serum samples with excellent recovery and repeatability (Zhou et al., 2022). Similarly, the nickel-based

MOF modifies the glassy carbon electrode and detects efficiently the glucose. NiO and Ni/NiO/CNTs display well-defined NiO redox peaks in the absence of glucose and increased peak currents in the presence of glucose. Furthermore, in the presence and absence of glucose, Ni/NiO/CNTs exhibit significantly enhanced peak current than NiO, indicating enhanced electrochemical performance of nanocomposite material (Yin et al., 2018). A chromium-based metal-organic framework (MIL-101) modified with platinum nanoparticles (PtNPs) simultaneously detects the xanthine, uric acid, and dopamine in spiked serum samples using the differential pulse voltammetry. The sensor has an extensive linear range (0.50 – 162.0 μM), a low detection limit (0.420 μM), and excellent selectivity. The simultaneous presence of dopamine, uric acid, and hypoxanthine in the detection of xanthine at working potentials of 0.130, 0.280, 0.680, and 1.050 V (*vs.* 3 M KCl saturated Ag/AgCl), estimating the concentration of xanthine in spiked blood specimens (Zhang et al., 2018).

(ii) Hydrogen peroxide sensing

A novel electrochemical sensing platform for hydrogen peroxide (H_2O_2) was developed using the Pt/$MoSe_2$ nanomesh, which offers an increase in active sites and a larger specific surface area. The Pt/$MoSe_2$ nanomesh sensors showed exceptional sensitivity and specificity towards H_2O_2. The correlation coefficient (R^2) and the limit of detection (LOD) were determined to be 0.9983 and 2.56 μM, respectively, at a signal-to-noise (S/N) ratio of 3. In addition, the Pt/$MoSe_2$ nanomesh exhibited excellent resistance to interference, even when exposed to potentially interfering tiny molecules found within cells, such as ascorbic acid (AA), glucose (Glc), and others (Wu et al., 2023). A poly(amidoamine)-dendrimer/poly (PAMAM/PNR) modified electrode was created and utilized to concurrently detect the electrochemical oxidation of L-dopa and the reduction of H_2O_2. The sensor electrode modified with PAMAM/PNR demonstrated a linear response ranging from 0.08 to 2400 μM for L-dopa, with a lower limit of detection (LOD) of 0.026 μM (Chakkarapani et al., 2024). Cobalt-based MOF ($Co(pbda)(4,4\text{-}bpy)\cdot 2H_2O]_n$) was incorporated on GCE and used for the detection of hydrogen peroxide (H_2O_2) at 0.1 M NaOH solution employing cyclic voltammetry (Yang et al., 2015).

(iii) Organic pollutant sensing

A cerium-based metal-organic framework has been utilized as a sensing material to detect metal by voltammetry. The detection method achieved a linear range spanning from 0.1 to 200 μM, with a detection limit of 30 nM (Hasani et al., 2020). Chlorophenols, an organic pollutant, are widely present in several industries and have been extensively utilized as pesticides, fungicides, herbicides, dyes, and solvents. Chlorophenols, which are found in many places, are extremely poisonous organic contaminants that have raised serious environmental worries. Chlorophenols possess toxicity towards people and can accumulate in the food chain, thereby impacting human beings. The electrochemical data demonstrated the excellent electrochemical capabilities of the modified GCEs in detecting chlorophenol, including a low limit of detection (LOD = 0.328 μM), a wide linear detection range from 10 to 160 μM, and strong stability and selectivity. Furthermore, the results of the recovery studies have demonstrated the suitability of the electrochemical sensor for detecting genuine samples. The findings indicate that the HP-UiO66@Ni-BDC MOF has the potential to be used as a sensor for the immediate and continuous detection of chlorophenol (Mohan et al., 2023; Stentiford et al., 2022).

(iv) Heavy metals sensing

The hydrothermal process synthesizes a zinc-based metal-organic framework (Zn-MOF), and exhibits high selectivity, sensitivity, and a low limit of detection (4.10 μM for $Cr_2O_7^{2-}$ and 6.63 μM for CrO_4^{2-}) in aqueous solution (Yang et al., 2023). A Eu-MOF, $\{[Eu_2(L)(phen)_2(ox)_2(H_2O)_2]\cdot 10H_2O\cdot phen\}_n$ was synthesized by hydrothermal methods, exhibiting excellent water stability and pH stability. The Eu-MOF has good sensitivity and selectivity in detecting gas/liquid benzaldehyde, Hg^{2+}, and $Cr_2O_7^{2-}$ /CrO_4^{2-} by luminescence quenching effects, making it a potential luminous sensor. Eu-MOF exhibits high adsorption capacities for Hg^{2+} and found useful materials for detecting the Hg^{2+} in tap water, green tea, and river water. The sensor demonstrated a recovery rate ranging from 99.88% to 102.66% for the detection of Hg^{2+} (Fan et al., 2024). Cd^{2+} and Pb^{2+} are simultaneously and selectively detected in water samples using the Yb-MOF-modified electrode. The Yb-MOF/GCE detects the Cd^{2+} and Pb^{2+} simultaneously in the 0 to 50 ppb concentration range (Zhang et al., 2001).

1.4 Scope of Present Investigation

The groundwater in some parts of the West Bengal and North Eastern states of India is contaminated with highly toxic arsenic. In this part, the ground is a major source of drinking water, hence causing arsenic poisoning to a large society residing in this region. Prolonged arsenic exposure causes different forms of malignancies, such as skin, lung, bladder, and kidney cancers. Moreover, the consumption of arsenic through drinking water increases the risk of heart disease. Similarly, lead is another highly toxic element and lead poisoning causes damage to the nervous system, particularly in children. Lead exposure affects kidney function and increases blood pressure, leading to cardiovascular problems. India has faced challenges with lead contamination, particularly from industrial emissions, lead-based paints, and improper recycling of lead-acid batteries. Cadmium is known to accumulate in the kidneys over time, causing severe damage and potentially leading to kidney disease. The Central Groundwater Board has revealed cadmium contamination in groundwater across several districts in Tamil Nadu. Notably, Tiruvallur district exhibited cadmium levels exceeding permissible limits, rendering the water unsafe for consumption. This contamination is often attributed to industrial effluents and inadequate waste management practices. On the other hand, micro-pollutants are emerging contaminants and pose severe environmental concerns. The micropollutants are partly degraded in the conventional wastewater treatment plants (WWTP) and the residues of these contaminants escape from these treatment plants and enter into the aquatic environment. Therefore, the levels of micropollutants are detected in the freshwater at the μg/L to ng/L. Ciprofloxacin is an antibiotic belonging to the fluoroquinolone class, and its presence in water bodies is hazardous to the environment and human health. In India, the concentrations of ciprofloxacin in surface waters reach the levels of 6.5 mg/L. Such contamination is attributed to pharmaceutical industries' effluents with inadequate wastewater treatment. The presence of ciprofloxacin in aquatic environments poses risks to non-target organisms and disrupts the ecosystems. Additionally, carbamazepine is a pharmaceutical drug commonly used to treat epilepsy, bipolar disorder, and certain types of nerve pain. Carbamazepine is toxic to aquatic organisms such as fish, algae, and invertebrates. It affects the physiological

processes, growth, and reproduction system. Therefore, the monitoring of these contaminants at low levels is inevitable to safeguard human and aquatic life. Although the advanced analytical tools detect these contaminants efficiently, the detection devices operate offsite and the high cost of the instruments restricted the widespread use of these analytical tools. However, the electrochemical methods are useful for miniaturized devices and enable the onsite detection of several contaminants in aqueous medium. Further, the use of advanced materials in fabricating microelectrodes provides the efficient and selective detection of several contaminants in aquatic environments.

The present research aims to establish a simple, economical, and portable electrochemical sensor for the reliable detection of emerging water contaminants, specifically As(III), Cd(II), and Pb(II), along with micropollutants such as ciprofloxacin (CFX) and carbamazepine (CBZ). The metal-organic frameworks are highly porous and functionalized materials that have wider applications in environmental engineering. The high specific surface area with tuneable porosity enhances the applicability of these materials. The titanium and zirconium-based metal-organic frameworks are synthesized in a robust synthetic route. Further, the thin film glassy carbon electrodes (Ti-MOF/GCE and Zr-MOF/GCE) are obtained by the drop-casting method.

These electrodes (Ti-MOF/GCE and Zr-MOF/GCE) are then employed to detect trace amounts of emerging water pollutants in an attempt to devise miniaturized detection systems. The stability, shelf life, and real implications of these probes are greater challenges. The present studies extensively utilize the Ti-MOF/GCE and Zr-MOF/GCE in the detection of As(III), Pb(II), Cd(II), CFX, and CBZ in an aqueous medium. Moreover, the stability of these electrodes and real implications enhance the practical applicability of the studies.

CHAPTER 2

METHODOLOGY

2. METHODOLOGY

2.1 CHEMICALS AND APPARATUS

Table 2.1 includes the complete list of chemicals/reagents used for the present work. The chemicals are not further purified unless specified in the methodology section.

Table 2.1: Complete list of chemicals/reagents used in the present investigation.

Sl. No	**Chemicals**	**IUPAC Name**	**Formula**	**Company**	**CAS No./ID**
1	Sodium Arsenite	Sodium (meta) arsenite	$NaAsO_2$	HiMedia Chemical, Mumbai India.	1847-14-8
2	Lead acetate	Lead acetate	$Pb(C_2H_3O_2)_2$	HiMedia Chemical, Mumbai India.	6080-56-4
3	Sodium phosphate dibasic heptahydrate	Disodium; dihydrogen phosphate; heptahydrate	$Na_2HPO_4•7H_2O$	HiMedia Chemical, Mumbai India.	7558-79-4
4	Sodium phosphate monobasic monohydrate	Sodium dihydrogen phosphate	$NaH_2PO_4•H_2O$	HiMedia Chemical, Mumbai India.	10049-21-5.

5	Ferric chloride	Iron trichloride hexahydrate	$FeCl_3.6H_2O$	HiMedia Chemical, Mumbai India.	10025-77-1
6	Sodium acetate anhydrous	Sodium acetate	CH_3COONa	HiMedia Chemical, Mumbai India.	127-09-3
7	Acetic acid	Acetic acid	CH_3COOH	HiMedia Chemical, Mumbai India.	64-19-7
8	Lead nitrate	Lead nitrate	$Pb(NO_3)_2$	Merck, Mumbai, India	10099-74-8
9	Potassium ferricyanide	Potassium hexacyanoferrate (III)	$K_3[Fe(CN)_6]$	Merck, Mumbai, India	13746-66-2
10	Potassium ferrocyanide	Potassium hexacyanoferrate (II) trihydrate	$K_4[Fe(CN)_6]\cdot 3 H_2O$	Merck, Mumbai, India	14459-95-1
11	Potassium chloride	Potassium chloride	KCl	Merck, Mumbai, India	7447-40-7

12	Copper sulphate	Copper sulphate	$CuSO_4$	Merck, Mumbai, India	7758-98-7
13	Ethyl alcohol	Ethanol	C_2H_5OH	Merck, Mumbai, India	64-17-5
14	Cadmium nitrate tetrahydrate	Cadmium nitrate tetrahydrate	$Cd(NO_3)_2.4H_2O$	Merck, Mumbai, India	10022-68-1
15	Zinc sulphate	Zinc sulphate	$ZnSO_4$	Merck, Mumbai, India	7446-20-0
16	Chromium chloride	Chromium chloride	$CrCl_3$	Merck, Mumbai, India	10049-05-5
17	Methanol	Methanol	CH_3OH	Merck, Mumbai, India	67-56-1
18	Sodium hydroxide	Sodium hydroxide	NaOH	Merck, Mumbai, India	1310-73-2
19	N,N-dimethylformamide (DMF)	N,N-dimethylformamide	C_3H_7NO	Merck, Mumbai, India	68-12-2

20	Nickel chloride	Dichloronickel	$NiCl_2$	Merck, Mumbai, India	7718-54-9
21	Oxalic acid	Oxalic acid	$C_2H_2O_4$	Merck, Mumbai, India	144-62-7
22	Sodium chloride	Sodium chloride	NaCl	Merck, Mumbai, India	7647-14-5
23	Sodium nitrate	Sodium nitrate	$NaNO_3$	Merck, Mumbai, India	7631-99-4
24	Magnesium sulphate	Magnesium sulphate	$MgSO_4$	Merck, Mumbai, India	7487-88-9
25	Sulphuric acid	Sulphuric acid	H_2SO_4	Merck, Mumbai, India	7664-93-9
26	2-Aminoterephthalic acid	2-Aminoterephthalic acid	NH_2-BDC	Sigma Aldrich, USA	24863783
27	Zirconium(IV) chloride	Zirconium(IV) chloride	$ZrCl_4$	Merck, Mumbai, India	10026-11-6

28	Fluoride low-range reagent	Fluoride	F^-	Hanna Instruments, India	Hi-93729
29	Chloride reagent	Chloride	Cl^-	Hanna Instruments, India	Hi-93753
30	Nitrate reagent	Nitrate	NO_3^-	Hanna Instruments, India	Hi-93728
31	Sulfate reagent	Sulphate	SO_4^{2-}	Hanna Instruments, India	Hi-93751
32	Phosphate reagent	Phosphate	PO_4^{3-}	Hanna Instruments, India	Hi-93713
33	Glassy carbon plate 1mm thick (Type 1)	Carbon	C	Thermofisher scientific, India	038021
34	Terephthalic acid	Terephthalic acid	C_6H_4-1,4-$(CO_2H)_2$	Sigma Aldrich, USA	100-21-0

The Arium Mini Plus UV Lab water purification system was utilized to get purified water with a water resistivity of 18.2 MΩ × cm and a conductivity of less than 20 µS/cm. All solutions are prepared using the purified water. Acetate buffer and phosphate buffer solutions are prepared as described by Hamed and wang (Hemed et al., 2018; Wang et al., 2013).

2.2 INSTRUMENTS

An electronic balance (HPB220, Wensar, India) was employed for all weighing the chemicals. pH of solutions was measured using a Microprocessor pH meter (Labtronics India Ltd., India; Model No.: LT-16). The centrifuge (REMI-23, Vasai, India) with a maximum rotational speed of 6900 revolutions per minute (RPM) is used for centrifugation purposes. A bath Sonicator (LMUS-4, Wensar, India) is employed for different sonication purposes.

The surface morphology and surface roughness of materials are obtained using an Atomic Force Microscope (AFM) (Ntegra Aura instrument from NT MDT, Russia). Field Emission Scanning Electron Microscope/Energy dispersive X-ray (FESEM/EDX: JEOL JSM 7100F; Oxford Xmax, Japan) are utilized with the operating parameters as 15 kilovolts (kV), magnification range of 10 to 1,000,000 with an accelerating voltage between 0.2 and 30 kV, and the probe current varied from 1 picoampere (pA) to 400 nanoamperes (nA). Similarly, the High-Resolution Transmission Electron Microscope (HRSTEM) (JEOL JEM 2100; Oxford Xtreme) was utilized with a 200 kV acceleration voltage and 40K magnification.

The X-ray diffraction (XRD) instrument (PANalytical X'Pert PRO MPD, manufactured in the Netherlands) is utilized for obtaining the powder diffraction pattern of MOF materials. The equipment was operated at a scan rate of 0.033 of 20 illumination, and the generator settings of 30 mA and 40 kV. The anode material consists of Cu $K_{\alpha 1}$ and $K_{\alpha 2}$ radiations, at the wavelengths of 1.5406 and 1.54443 Å, respectively. The XPS (ESCA 3500, Japan) analyzer determines the elemental composition of Ti-MOF and also identifies the oxidation states of the components in MOF. The Brunauer-Emmett-Teller (BET) analyzer (Micromeritics ASAP 2000 V2.04, USA) determines the surface volume, area, and pore dimensions of the MOF materials. The thermogravimetric analyzer (TGA; SDT Q600 V20.9 Build 20, USA) analyses the thermal stability of the material.

A TOC analyzer (TOC-VCPH/CPN, Shimadzu, Japan) was used to measure the non-purgeable organic carbon (NPOC) and inorganic carbon (IC) content of water samples. An Atomic Absorption Spectrometer (AAS) (Shimadzu, Inc AA-7000, Japan) is used. A Multiparameter photometer (Hanna, model: Hi83300, USA) is used

for obtaining various parametric data of water samples. Similarly, a Multiparameter waterproof meter (probe) obtained by Hanna, USA (model: HI98194) was employed to obtain the pH, ORP (Oxidation-Reduction Potential), conductivity, resistivity, TDS (Total Dissolved Solid), and salinity of the natural water samples. The electrochemical studies were conducted using an electrochemical workstation (Biologic Instruments electrochemical workstation (Model SP-200, France)). The reference electrode (Ag/AgCl/KCl (3.5M)) obtained by BaSi, USA (Model: RE-5B), and a platinum counter electrode (outer diameter-6 mm, inner diameter 1.6 mm; Model: A-002013, Allum, USA), and a glassy carbon working electrode (GCE) (outer diameter – 6 mm, inner diameter - 3 mm; Model: A-002421, Allum, USA). The electrochemical data were analyzed using the integrated computer program EC-Lab. EC-Lab is a comprehensive software platform specifically designed for BioLogic Potentiostat/Galvanostat/FRA instruments used for entire electrochemical analyses.

2.3 MATERIALS PREPARATION

2.3.1 Synthesis of Titanium Metal-Organic Framework

An accurate 3.8404 g of 2-amino terephthalic acid (21.2 mmol) was dissolved in 50 mL of anhydrous N, N-dimethylformamide (DMF) (Purity(GC) $\geq$ 99.8 %) by agitating it in a 500 mL round bottom flask at 110°C for 1 hrs. Subsequently, 14 mL of dehydrated methanol was added to the solution and stirred for one hrs under reflux at 120^{o}C. Further, 4.2 mL (12.3 mmol) of $Ti(BuO)_4$ was introduced into the flask and agitated for 3 days at 120^{o}C under reflux. After 3 days the solution mixture was kept at room temperature to cool down. The solution mixture was filtered using Whatman filter paper (pore size 11μm) and yielded a yellow crystalline substance. The product was washed with 5 mL of DMF to eliminate any remaining unreacted substances, followed by 5 mL of methanol. The solid product was dried at 155°C for 24 hrs in a vacuum to receive golden-colored MOF and the measured product yield was 4.34 g.

2.3.2 Synthesis of Zirconium Metal-Organic Framework

A solution of terephthalic acid (1.514 g) in 30 mL of DMF is prepared by simple mixing at room temperature. Further, separately the zirconium chloride (2.236 g) is dissolved in 10 mL of DMF at room temperature. Further, the zirconium chloride solution is slowly mixed with the terephthalic acid solution and the resulting solution is continuously agitated for 1 hr at 60°C. The solution mixture was kept on reflux for 48 hrs at 120^{o}C. Subsequently, it was cooled at room temperature and filtered using a filter paper (11μm). The solid was then washed with 5 mL of DMF and 5 mL of methanol, and dried at 150^{o}C for 3 hrs to obtain the Zr-MOF solid.

2.3.3 Determination of pH_{PZC} of solids

The pH at which the total charge on the solid surface equals zero is known as the point of zero charge (pH_{PZC}). At pH < pH_{PZC}, the solid surface has a positive charge, while at pH > pH_{PZC}, it has a negative charge. The drift approach was utilized to determine the pH_{PZC} (Saha et al., 2020). The pH_{PZC} is obtained as: in 1 L Erlenmeyer flask, 500 mL of purified water was added, capped with cotton, and slowly and continuously heated till boiling for 20 minutes to remove dissolved CO_2. The flask was immediately closed to prevent the reabsorption of CO_2 from the air. Then, 50 mL of 0.01 mol/L NaCl solutions were made from CO_2-free water, and the pH of each solution in each flask was adjusted to 2.0, 4.0, 6.0, 8.0, 10.0, and 12.0 by adding 0.1 mol/L HCl or 0.1 mol/L NaOH solutions. 100 mg of the solid sample was added to each vial, which was tightly sealed and shaken for 24 hrs at 25^{0}C. The final pH of the solutions was recorded, and a graph was drawn between $pH_{Initial}$ and pH_{Final}. The point of zero charges was determined by the intersection of these curves, where $pH_{Initial}$ = pH_{Final}.

2.3.4 Speciation studies

The speciation experiments for As(III), Pb(II), and Cd(II) were conducted using the Visual MINTEQ (Version 3.1), a freeware chemical equilibrium model used to calculate metal speciation studies in an aqueous medium. The input parameters were set to an initial concentration of 10 mg/L of As(III), Pb(II), and Cd(II) at a constant

temperature of 25°C. The input thermodynamic equilibrium constants utilized are given in Tables 2.2, 2.3, and 2.4. Further, the percentage speciation of different species of these metal ions is obtained as a function of pH.

Table 2.2: Equilibrium constants used for the speciation of As(III) in aqueous solutions at 25^0C.

Equilibrium	**Log K**
$AsO_3^{3-} + H^+ \longleftrightarrow HAsO_3^{2-}$	13.41
$AsO_3^{3-} + 3H^+ \longleftrightarrow HAsO_3$	34.74
$AsO_3^{3-} + 2H^+ \longleftrightarrow HAsO_3^-$	25.45
$AsO_3^{3-} + 4H^+ \longleftrightarrow HAsO_3^+$	34.43

Table 2.3: Equilibrium constants used for the speciation of Pb(II) in aqueous solutions at 25^0C.

Equilibrium	**Log K**
$Pb^{2+} + 2H_2O \longleftrightarrow Pb(OH)_2 + 2H^+$	-16.91
$2Pb^{2+} + H_2O \longleftrightarrow Pb_2(OH)^{3+} + H^+$	-6.36
$3Pb^{2+} + 4H_2O \longleftrightarrow Pb_3(OH)_4^{2+} + 4H^+$	-23.86
$4Pb^{2+} + 4H_2O \longleftrightarrow Pb_4(OH)_4^{4+} + 4H^+$	-20.88
$Pb^{2+} + 3H_2O \longleftrightarrow Pb(OH)_3^- + 3H^+$	-28.08

Table 2.4: Equilibrium constants used for the speciation of Cd(II) in aqueous solutions at 25^0C.

Equilibrium	**Log K**
$Cd^{2+} + 3H_2O \longleftrightarrow Cd(OH)_3^- + 3H^+$	-33.30
$Cd^{2+} + 4H_2O \longleftrightarrow Cd(OH)_4^{2-} + 4H^+$	-47.28
$Cd^{2+} + H_2O \longleftrightarrow Cd(OH)^+ + H^+$	-10.09
$Cd^{2+} + 2H_2O \longleftrightarrow Cd(OH)_2 + H^+$	-20.29
$2Cd^{2+} + H_2O \longleftrightarrow Cd(OH)^{3+} + H^+$	-9.39

2.4 REAL WATER SAMPLES

Water samples are collected from three different locations *viz*., the Chite River in Falkland Veng (N23.73916, E092.74136), the Tlawng River (N23.814238 and E92.651924), and two samples from the groundwater of Tanhril village (N23.737959 and E92.675085) and (N23.744126 and E92.674198) within the Aizawl City, Mizoram, India. These water samples were filtered using the Whatman filter paper (0.45 μm) to eliminate any silt or suspended particles before utilizing them. These samples are subjected to various physicochemical parametric analyses using the multiparameter probe, a TOC analyzer, and an atomic absorption spectrometer. These water samples were spiked with known concentrations of arsenic (III), cadmium (II), lead (II), ciprofloxacin, and carbamazepine for their electrochemical studies.

2.5 MATERIALS CHARACTERIZATION

The X-ray diffraction pattern of the MOFs, allows us to obtain the crystalline structure of the MOFs. The BET analyses of Ti-MOF and Zr-MOF are performed using the N_2 adsorption and desorption isotherms. The results determine the pore volume, surface area, and pore size of the materials. The surface morphology and elemental mapping of the materials, viz., bare glassy carbon plate and Ti-MOF or Zr-MOF coated glassy carbon plates. The plate was first polished with an alumina slurry, which then underwent washing with double distilled water, polished with a 1 μm diamond rubbing solution, and subjected to sonication for 120 seconds. The cleaned carbon plate was dried in a hot air oven at 35°C for 15 minutes and cooled at room temperature. Further, the plate was coated with a 0.02 mL casting solution which was prepared by mixing 5 mg of MOF (Ti-MOF/Zr-MOF) and 4 mL of mixed solvent (1:1 ratio of DMF and De-ionized water). The plate was then dried in a hot air oven at 40°C for 30 mins. The Ti-MOF or Zr-MOF glassy carbon sheets were subsequently subjected to the field emission scanning electron microscope/energy dispersive X-ray analysis (FE-SEM/EDX). The HRSTEM micrographs of Ti-MOF and Zr-MOF were acquired utilizing powder samples of these materials. In addition, the average particle

size was measured using the Image J program, and the d-spacings of the MOFs were determined using GDM software. The surface roughness was determined by atomic force microscopy and the thermal stability of the pristine MOFs was observed using the thermo-gravimetric analyzer.

2.6 FABRICATION OF ELECTRODES

The drop-casting method fabricates the working glassy carbon electrode using the MOFs. Scheme 2.1 shows the schematic of the fabrication of glassy carbon electrodes utilizing the MOF materials. The GCE electrode was first polished using the polishing pad, which contained the 0.005 µm alumina slurry solution. Subsequently, the electrode was washed with purified water followed by rubbing with 1 µm diamond solution. Finally, the electrode is again cleaned with purified water. The electrode is washed with ethanol and purified water separately under sonication for 2 mins each. Afterward, the GCE surface is cleaned again with purified water and dried at 35°C for 15 min. The casting solution is prepared by mixing 5 mg of MOF (Ti-MOF/or Zr-MOF) and 4 mL of mixed solvent (1:1 ratio of DMF and De-ionized water). The cleaned and dried GCE is subjected to drop-casting using 0.02 mL of the casting solution at the electrode surface using a micropipette. The electrode is dried at 40°C for 30 min followed by cooling at room temperature. The dried electrode is ready for the electrochemical studies.

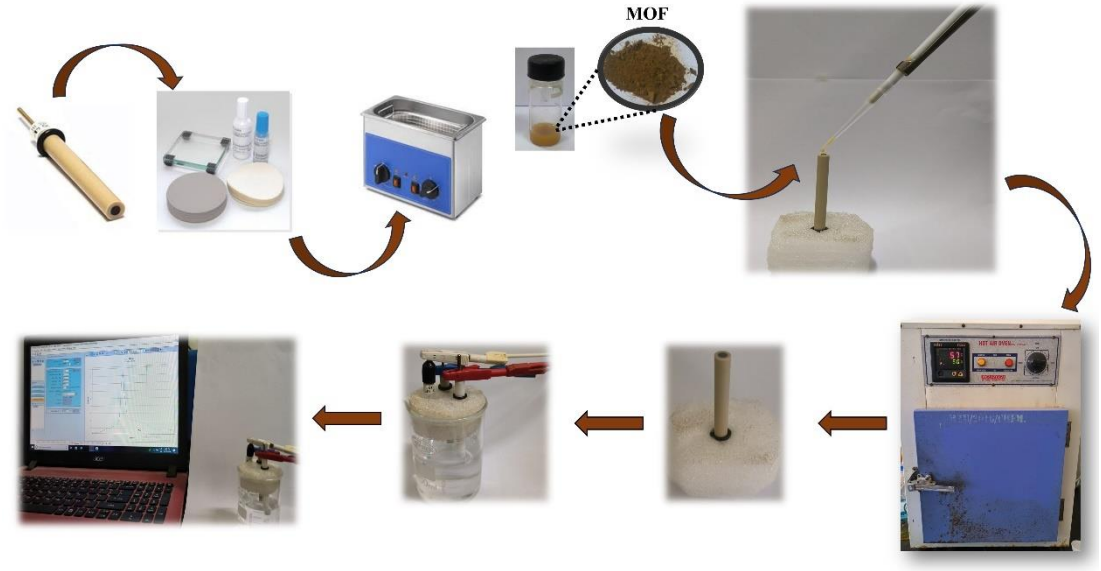

Scheme 2.1: (a) Polishing the GCE surface; (b) Sonication of GCE; (c) Drop casting of GCE; (d) Drying of fabricated GCE at 35°C; (e) The fabricated GCE utilized for experimentation.

2.7 PROCEDURES FOR ELECTROCHEMICAL METHOD

2.7.1 Electrochemical characterization of fabricated working electrodes

The standard solution of 0.002 M $[Fe(CN)_6]^{3-/4-}$ in 0.10 M KCl characterizes the bare glassy carbon electrode (GCE), Ti-MOF/GCE and Zr-MOF/GCE under the cyclic voltammetry. The potential window was kept at -0.1 to 1.0 V (Ag/AgCl), and the scan rate was set at 100 mV/s. The working electrodes were bare GCE, Ti-MOF/GCE, and Zr-MOF/GCE. The scan rate was increased from 50 to 150 mV/s, at a potential window of -0.5 to 0.1 V. The study uses a 0.002 M standard redox couple $[Fe(CN)_6]^{3-/4-}$ in 0.10 M KCl as a supporting electrolyte. Usually, the diffusion-controlled electrochemical processes showed a linear increase in the peak oxidative/or reductive peak current against the square root of the scan rates as followed by the Randles-Sevcik equation (2.1).

$$I_p = 2.69 \times 10^5 \times n^{2/3} \times \nu^{1/2} \times D^{1/2} \times C \times A \quad \text{..... (2.1)}$$

where, I_p: oxidative/or reductive peak current (mA)

n: number of electrons involved in the redox process

ν: scan rate (mV/s)

D: diffusion coefficient of $[Fe(CN)_6]^{3-/4-}$

C: concentration of electroactive species

A: electroactive surface area of working electrode (mm^2)

The electrodes Ti-MOF/GCE and Zr-MOF/GCE, as well as the bare GCE, were examined for EIS characterization. The impedance spectra were measured for all the participants within the frequency range of 85 kHz to 105 MHz in the redox couple solution. The measurements were taken at a rate of 6 points per decade, with a sinusoidal amplitude of 10.0 mV. The most accurate equivalent circuit, $R_1+Q_2/(R_2+W_2)$, was derived for all the working electrodes. In this equation, R_1 represents the solution resistance (R_s), Q_2 represents the double-layer capacitance (C_{dl}) at the solution and electrode interface, R_2 represents the charge transfer resistance (R_{ct}), and W_2 represents the Warburg impedance (Z_W) in the Randle's circuit. This circuit provided the best fit for the obtained Nyquist plot. The EC-lab program is utilized to perform equivalent circuit fitting and electrical parameter evolution for each impedance spectrum using the least square fitting approach.

2.7.2 Electrochemical determination of pollutants

The study utilized Ti-MOF material fabricated on a GCE (glassy carbon electrode) to detect hazardous As(III) ions. The GCE was then used in a study involving differential pulse anodic stripping voltammetry. The electrolyte used was a 0.1 M acetate buffer solution. Before executing the detection experiment, the experimental conditions were optimized, including pH, deposition potential, and deposition time. An investigation was conducted on the pH range of 2.0 to 7.0 in an acetate buffer solution that included 25.0 µg/L of As(III). A study was undertaken to investigate the deposition potential ranging from -0.9 to -1.3, while the deposition time was varied from 30.0 to 180.0 seconds. The experimental parameters, including a pulse

amplitude of 50 mV, a scan increment of 10 mV, and a pulse width of 50 ms, were kept constant throughout all the experiments. The study examined the behavior of various manufactured electrodes, including bare GCE and Ti-MOF/GCE, under optimized conditions. A concentration study was conducted within the range of 0.2 to 25.0 µg/L. An interfering study was also performed by introducing interfering ions at a 10-fold increase compared to the concentration of 25.0 µg/L As(III). The interfering ions were Ca^{2+}, Mg^{2+}, F^-, Cl^-, and NO_3^-. A reproducibility investigation was conducted by repeatedly detecting 25.0 ug/L of As(III) five times. A stability study was also conducted by detecting the detection after every 12 hrs within a period of 0 to 48 hrs. The produced electrode was held at room temperature during the study. An examination was performed on actual water samples utilizing groundwater and spring water that were artificially contaminated with different concentrations of As(III) ranging from 5.0 to 25.0 µg/L. A recovery rate investigation was undertaken by measuring the spiked concentration in an actual water sample.

The work utilized Ti-MOF material to create a GCE for the simultaneous detection of Pb(II) and Cd(II) by the DPV technique. The electrolyte used was a 0.1 M acetate buffer solution. Before executing the detection experiment, the experimental conditions were optimized, including pH, deposition potential, and deposition time. An investigation was conducted on the pH range of 3.5 to 5.5 in an acetate buffer solution that contained 50.0 µg/L of Pb(II) and Cd(II). A study was undertaken to investigate the deposition potential, ranging from -1.0 to -1.4, and the deposition time, ranging from 30.0 to 160.0 seconds. The pulse amplitude of 50 mV, scan increment of 10 mV, and pulse width of 50 ms were kept constant throughout the entire experiment. The study investigated the behavior of various manufactured electrodes, including bare GCE (glassy carbon electrode) and Ti-MOF/GCE (titanium metal-organic framework modified glassy carbon electrode), under optimized conditions. An investigation was conducted to determine the concentration range of 5.0 to 25.0 µg/L. A study was done to investigate the impact of a 10-fold increase in interfering ions, including Ca^{2+}, Mg^{2+}, F^-, Cl^-, and NO_3^-, compared to a concentration of 25.0 µg/L Pb(II) and Cd(II). Analyzed water samples consisted of groundwater and spring water that was intentionally contaminated with different concentrations of Pb(II) and Cd(II) ranging from 5.0 to 25.0 µg/L. A recovery rate investigation was undertaken by measuring the

spiked concentration in an actual water sample. The supporting electrolyte used for the determination of micropollutants is a 0.1 M phosphate buffer solution.

The Zr-MOF/GCE electrode was used to detect Ciprofloxacin (CFX) and Carbamazepine (CBZ). The electrochemical behavior of the Zr-MOF/GCE was analyzed using a cyclic voltammetry (CV) study to determine the reversibility of the pollutant. The electrochemical behavior of contaminants was investigated using differential pulse anodic voltammetry on both a bare glassy carbon electrode (GCE) and a zirconium-based metal-organic framework modified GCE (Zr-MOF/GCE). The study focused on optimizing the experimental parameters for CFX and CBZ at a concentration of 25.0 µg/L. The process of pH optimization was conducted using a PHB at various pH levels ranging from 5.0 to 9.0. The deposition potential range for CFX was investigated from -0.5 to -1.0 V, while for CBZ it was researched from -1.3 to -0.9 V. The time study for CFX ranges from 60.0 to 240.0 seconds, while for CBZ it ranges from 30.0 to 210.0 seconds. The electrochemical determination of CFX and CBZ was conducted within the concentration range of 10.0 to 250.0 µg/L, under optimized experimental conditions. To disrupt the investigation, a tenfold increase in the concentration of interfering ions was used to measure the levels of CFX and CBZ. The interfering ions include As(III), Cu(II), Ca(II), Mg(II), F^-, Cl^-, and NO_3^-. The stability of CFX and CBZ was investigated by continuously measuring their concentrations at a level of 50.0 µg/L for a period of 0 to 168 hrs. An investigation was carried out on a real matrix by using river water that was artificially contaminated with different quantities of CFX and CBZ. The recovery rate investigation was performed by analyzing the spiked concentration in an actual water sample.

The equations employed to determine the limit of detection (LOD) and limit of quantification (LOQ) are as follows: the limit of detection (LOD) is calculated as three times the standard deviation (SD) divided by the slope (m) displayed in equation (2.2), whereas the limit of quantification (LOQ) is calculated as ten times the SD divided by the slope (m). The equation involves the standard deviation (SD) of six replicated blank samples and the mean slope ('m') of the calibration line displayed in equation (2.3).

$$\mathrm{LOD} = 3.3\frac{\mathrm{SD}}{\mathrm{m}} \qquad \text{..... (2.2)}$$

$$\mathrm{LOQ} = 10\frac{\mathrm{SD}}{\mathrm{m}} \qquad \text{..... (2.3)}$$

In addition, the relative standard deviation (RSD) was calculated using the equation (2.4)

$$\%\mathrm{RSD} = \frac{\mathrm{s}\times 100}{\mathrm{m}} \qquad \text{..... (2.4)}$$

where 's' denotes the standard deviation and 'm' represents the mean of the replicate data.

CHAPTER 3

RESULTS AND DISCUSSION

3. RESULTS AND DISCUSSION

3.1. MATERIALS CHARACTERIZATION

3.1.1 Surface Morphology of Solid

An Atomic Force Microscope (AFM) accurately measures the topography of a thin film surface. Figure 3.1 depicts the AFM images of the bare glassy carbon plate along with Ti-MOF and Zr-MOF-coated glassy carbon sheets. Figure 1(a) shows a relatively smooth surface of glassy carbon except few surface roughness. However, the Ti-MOF and Zr-MOF thin film glassy carbon plates show heterogeneous and rough surfaces. The Ti-MOF and Zr-MOF are aggregated on the surface forming fine grains on the surface (*Cf* Figure 3.1(b-c)). Similar morphological results are obtained for Ti-MOF and Zr-MOF using AFM (Yang et al., 2019; Yusof et al., 2023). Further, the average surface roughness (R_a) of the bare glassy carbon sheet, Ti-MOF, and Zr-MOF thin film glassy carbon plates is 1.18 nm. 8.03 nm and 22.44 nm, respectively. The results clearly show that the MOF-coated carbon plate possesses significantly higher surface roughness compared to the bare carbon plate. Previously it was shown that the Ti-MOF deposited on the pristine cotton fabric showed a R_a value of 38.6 nm (Yang et al., 2019). Also, the Zr-MOF deposited on the hollow fiber membrane showed a R_a value of 69.68 nm (Yusof et al., 2023).

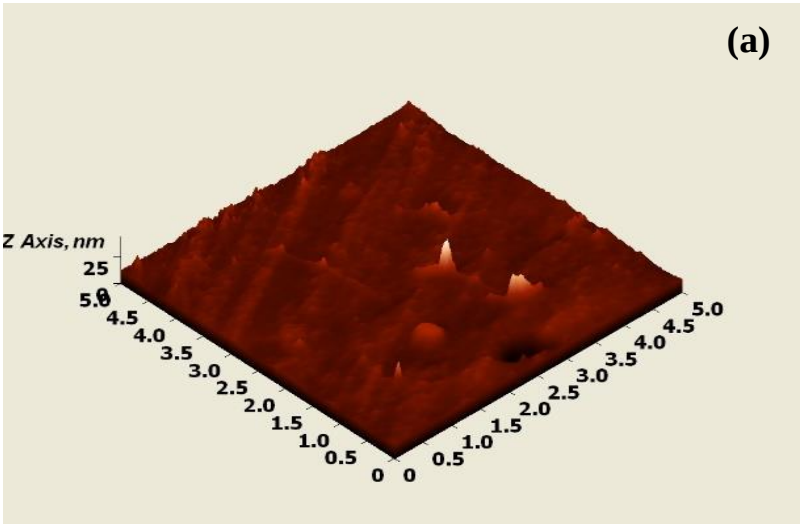

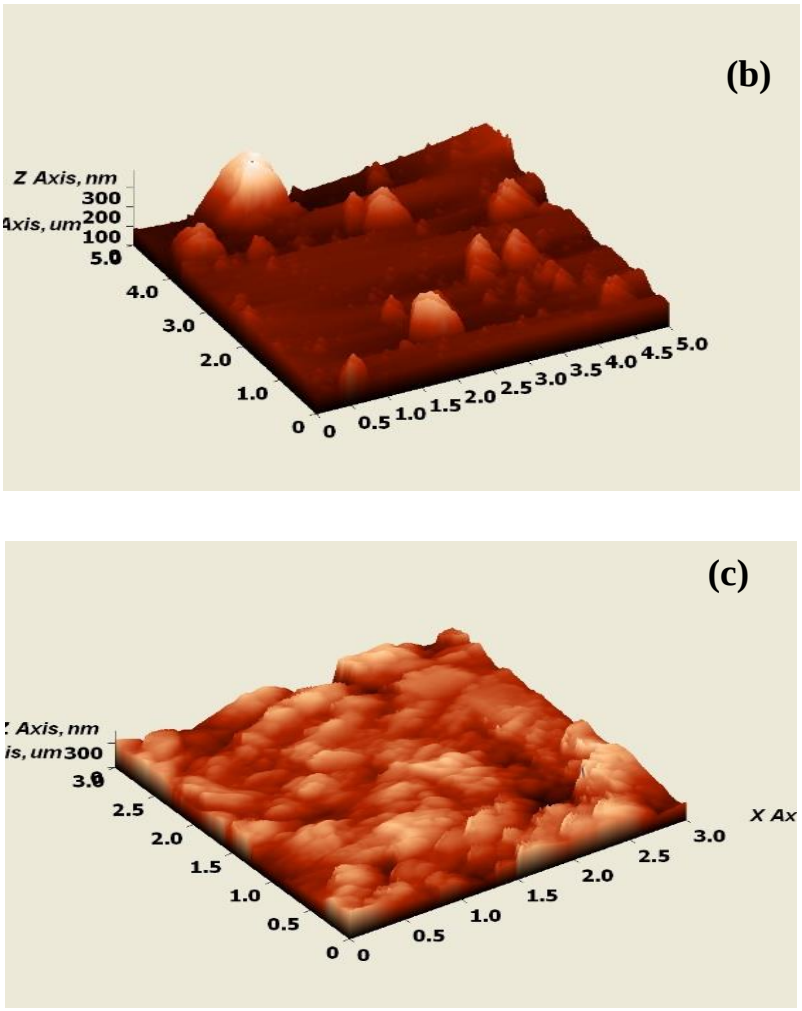

Figure 3.1. AFM images of (a) bare glassy carbon plate; (b) Ti-MOF coated glassy carbon plate; and (c) Zr-MOF coated glassy carbon plate.

The surface morphology of these metal-organic framework thin-film glassy carbon plates is obtained by scanning electron microscopic (SEM) analyses. Figure 3.2 (a, b & c) shows the SEM images of the bare glassy carbon sheet, Ti-MOF, and Zr-MOF coated glassy carbon plates. Figure 3.2 (a) shows that the bare carbon sheet possesses a very smooth surface structure. On the other hand, the SEM images of the Ti-MOF and Zr-MOF coated glassy carbon plates show heterogeneous surface structure as shown in figure 3.2 (b & c). The Ti-MOF particles with varied sizes are dispersed on the surface of the carbon plate. The particles are not aggregated on the surface. A similar heterogenous surface structure is obtained for the Ti-MOF as synthesized by the solvothermal process (Hendon et al., 2013). Similarly, the Zr-MOF

forms a heterogeneous surface structure; however, the Zr-MOF particles are aggregated on the surface. Further, interesting to observe that the Zr-MOF forms a flower-like structure. The SEM images of Zr-MOF (calcined) are found to be heterogeneous with aggregates of small crystallites resulting from the direct reaction of $ZrOCl_2$ with terephthalic acid (Carneiro et al., 2022).

Figure 3.2 (b & c[Insets]) depicts the EDX spectra of Ti-MOF and Zr-MOF coated plates. The EDX spectra reveal that Ti-MOF shows very distinct peaks of Ti, C, N, and O elements having atomic percentages of 6.81, 60.21, 10.22, and 22.76, respectively. Similarly, the Zr-MOF shows the EDX peaks of Zr, C, and O with atomic percentages of 3.42, 66.62, and 29.96, respectively. These results show that the Ti-MOF and Zr-MOF contain significant contents of Ti and Zr elements, respectively, possibly with its oxide forms.

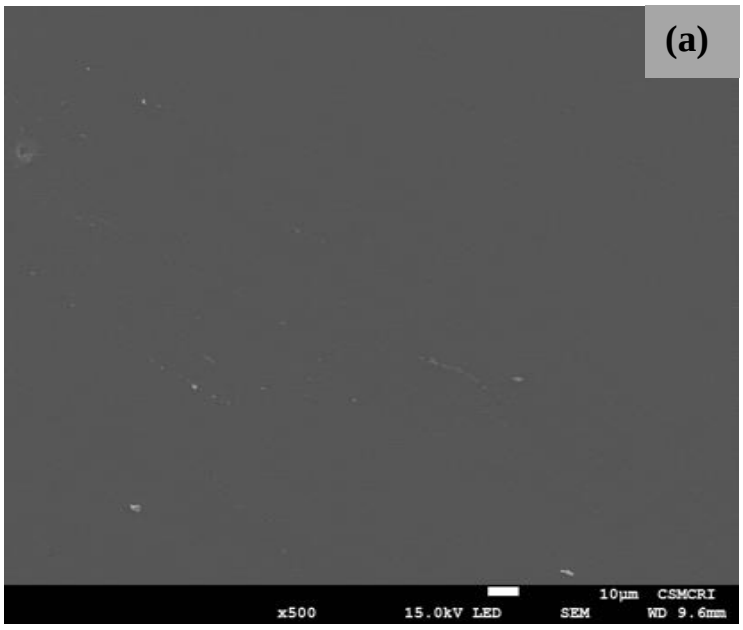

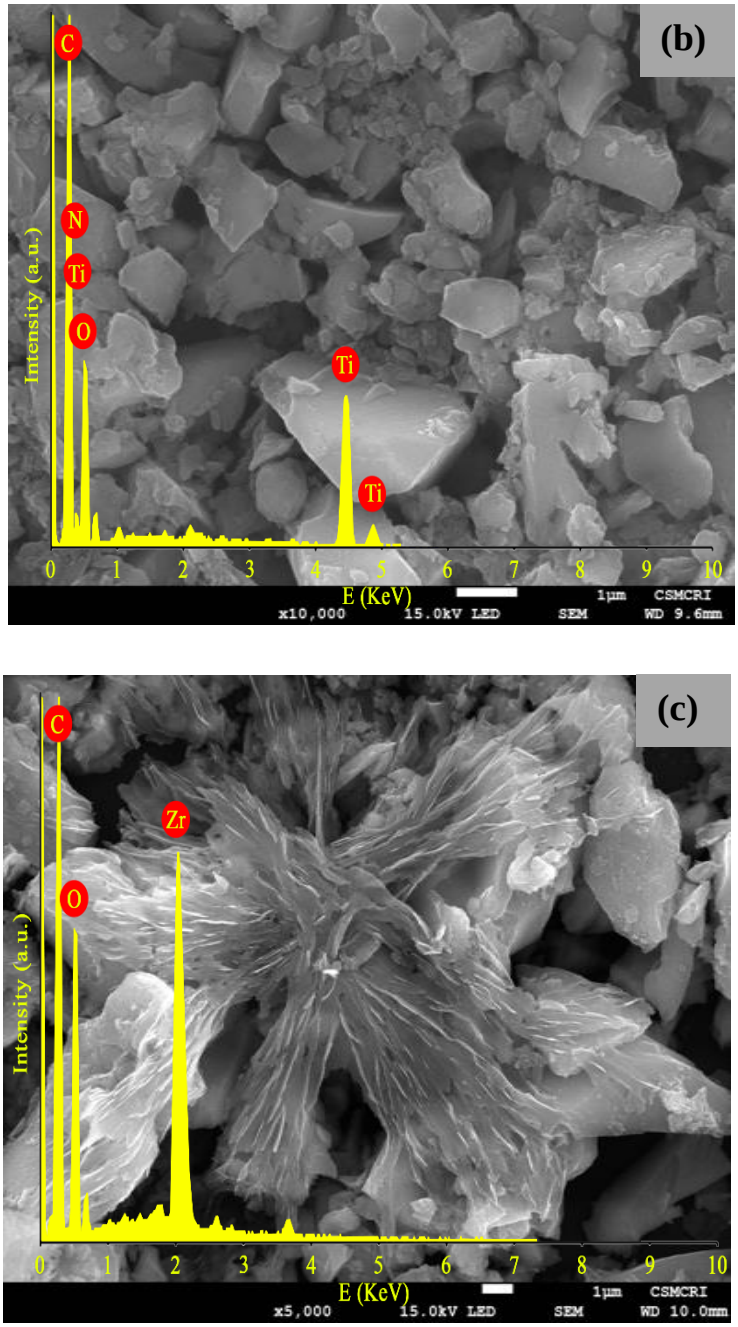

Figure 3.2. SEM image of: (a) Bare glassy carbon sheet; (b) Ti-MOF coated glassy carbon sheet, inset: EDX elemental spectrum for Ti-MOF; (c) Zr-MOF coated glassy carbon sheet, inset: EDX elemental spectrum for Zr-MOF.

Figure 3.3 shows the transmission electron microscopic (TEM) images of Ti-MOF and Zr-MOF solids. The Ti-MOF and Zr-MOF form the small-sized particles. Further, the TEM images show the fringes of the nanoparticles and Gatan Digital

micrograph which was utilized to obtain the d-spacings of the Ti-MOF and Zr-MOF and are found to be 0.86 nm and 0.28 nm, respectively (*Cf* Figure 3.3 (a & c)). These d spacings refer to the (110) lattice of TiO_2 and (111) lattice plane of ZrO_2, respectively, for the Ti-MOF and Zr-MOF solids. Moreover, the Image J software quantifies the mean particle size distribution of Ti-MOF and Zr-MOF as shown in Figure 3.3(b & d). The mean particle size diameter is 6.36 nm and 5.70 nm, respectively, for the Ti-MOF and Zr-MOF solids.

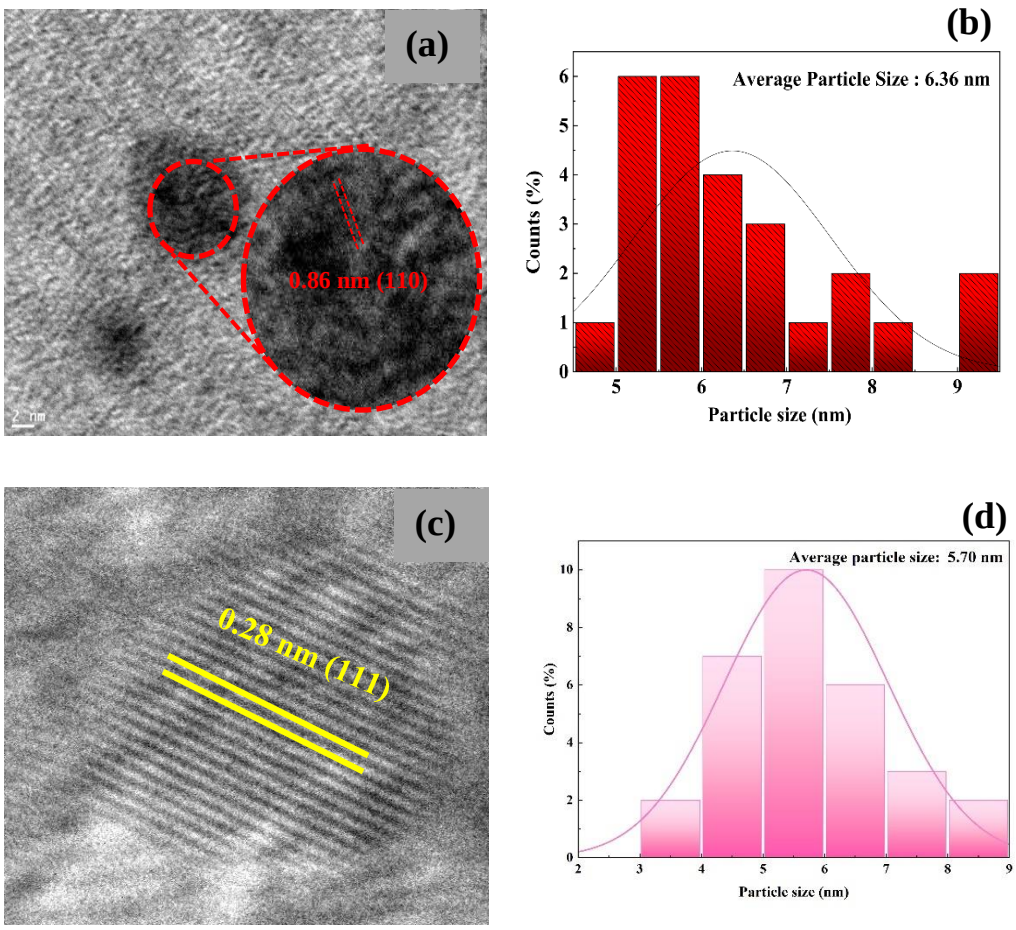

Figure 3.3: TEM micrographs of (a) Ti-MOF; (b) Average particle size distribution of Ti-MOF solid; (c) TEM micrograph of Zr-MOF; (d) Average particle size distribution of Zr-MOF solid.

Figure 3.4 shows the X-ray diffraction patterns of the Ti-MOF and Zr-MOF solids. The diffraction peaks at 24.71º, 36.75º, 47.49 º, 53.21º, 55.11º and 61.34º correspond to (101), (004), (200), (211), (105), and (204) plane respectively, confirms the presence of TiO_2 anatase phase (JCPDS card no. 21-1272) (El-Desoky et al., 2020). Similarly, the diffraction peaks of Zr-MOF occurred at 2θ values of 7.32° and 8.51° referring to the (111) and (200) crystal planes of ZrO_2, respectively (JCPDS no. 73-3458). The results indicate that the ZrO_2 possesses a face-cantered cubic lattice structure in the Zr-MOF (Li et al., 2024).

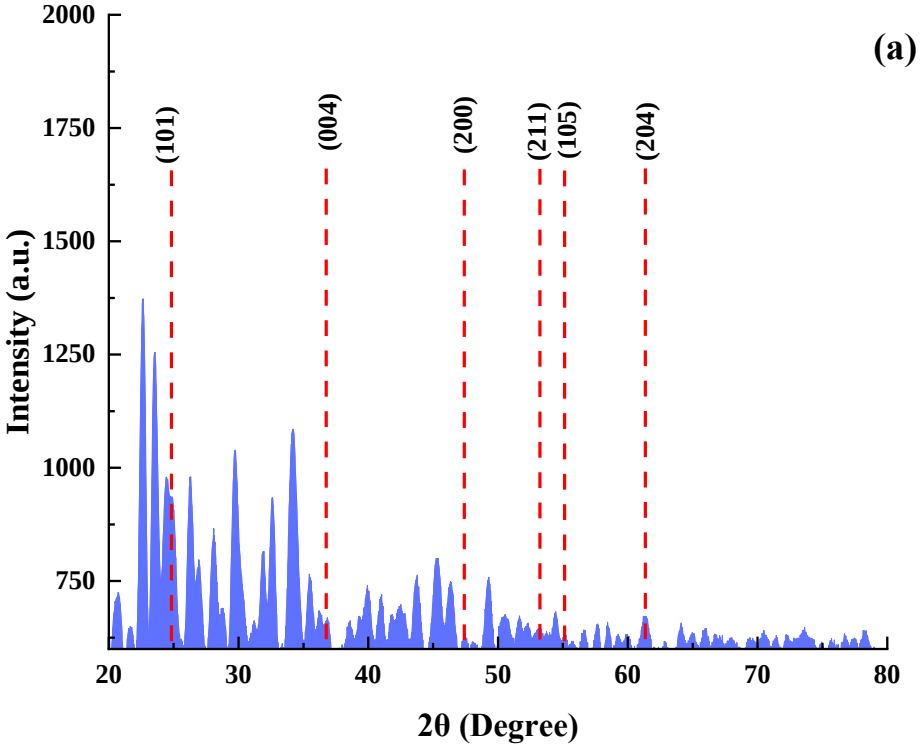

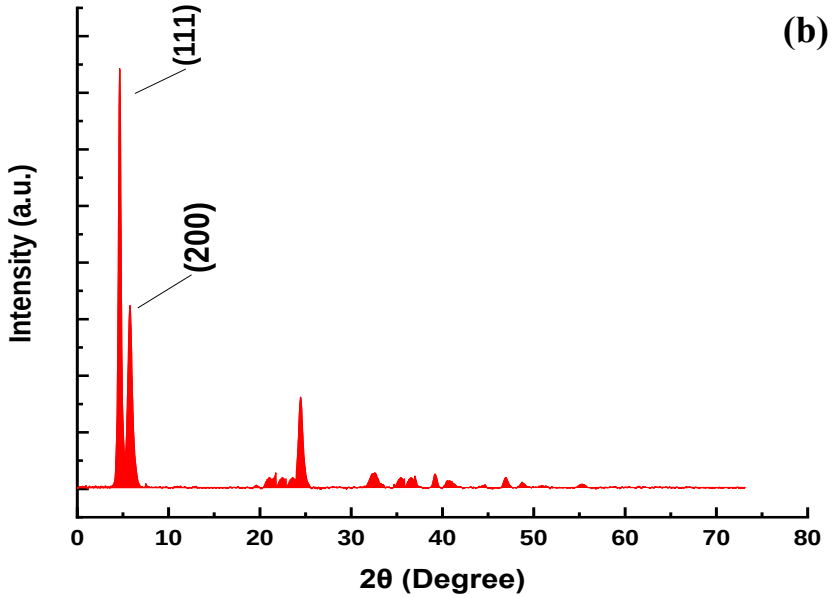

Figure 3.4: XRD pattern of (a) Ti-MOF; and (b) Zr-MOF.

The N_2 adsorption-desorption isotherms are shown in Figure 3.5. The figure showed the characteristics of isotherms and the pore diameter (BJH method) for these solids. The Ti-MOF exhibits type (IV) isotherm having an H3 hysteresis loop which indicates that Ti-MOF has a mesoporous surface (Ahmed et al., 2021). Similarly, the Zr-MOF exhibits type (I) isotherm having an H3 hysteresis loop indicating the microporous Zr-MOF with relatively small external surfaces (Motegi et al., 2017).

The specific surface area of the Ti-MOF and Zr-MOF is 1040.83 m^2g^{-1} and 840.98 $m^2\ g^{-1}$, respectively. Moreover, the pore volume and pore diameter of Ti-MOF are 0.31 cm^3g^{-1} and 3.30 nm, respectively. Similarly, the pore volume and pore diameter of Zr-MOF are 0.21 cm^3g^{-1} and 2.42 nm, respectively. These results are supported by the pore distribution curves of both Ti-MOF and Zr-MOF which are shown in Figure 3.5 (a & b [Insets]). These results showed that these MOF solids possess relatively very high specific surface area which is attributed to the formation of the framework with the linker molecules (Ahmed et al., 2021). The microwave-assisted synthesis of Ti-MOF gives the BET surface area of 620 $m^2\ g^{-1}$ (Solís et al., 2021). The BET surface area of Zr-MOF synthesized using the solvothermal approach was 876 $m^2\ g^{-1}$ with a pore volume of 0.38 $cm^3\ g^{-1}$, whereas the BET surface area of

Zr-MOF synthesized using the sonochemical method was 993.1 m^2 g^{-1} with a pore volume of 0.14 cm^3 g^{-1}. Furthermore, the increased surface area of the solid favors the enhanced sorption of sorbate species (Kazemi et al., 2023).

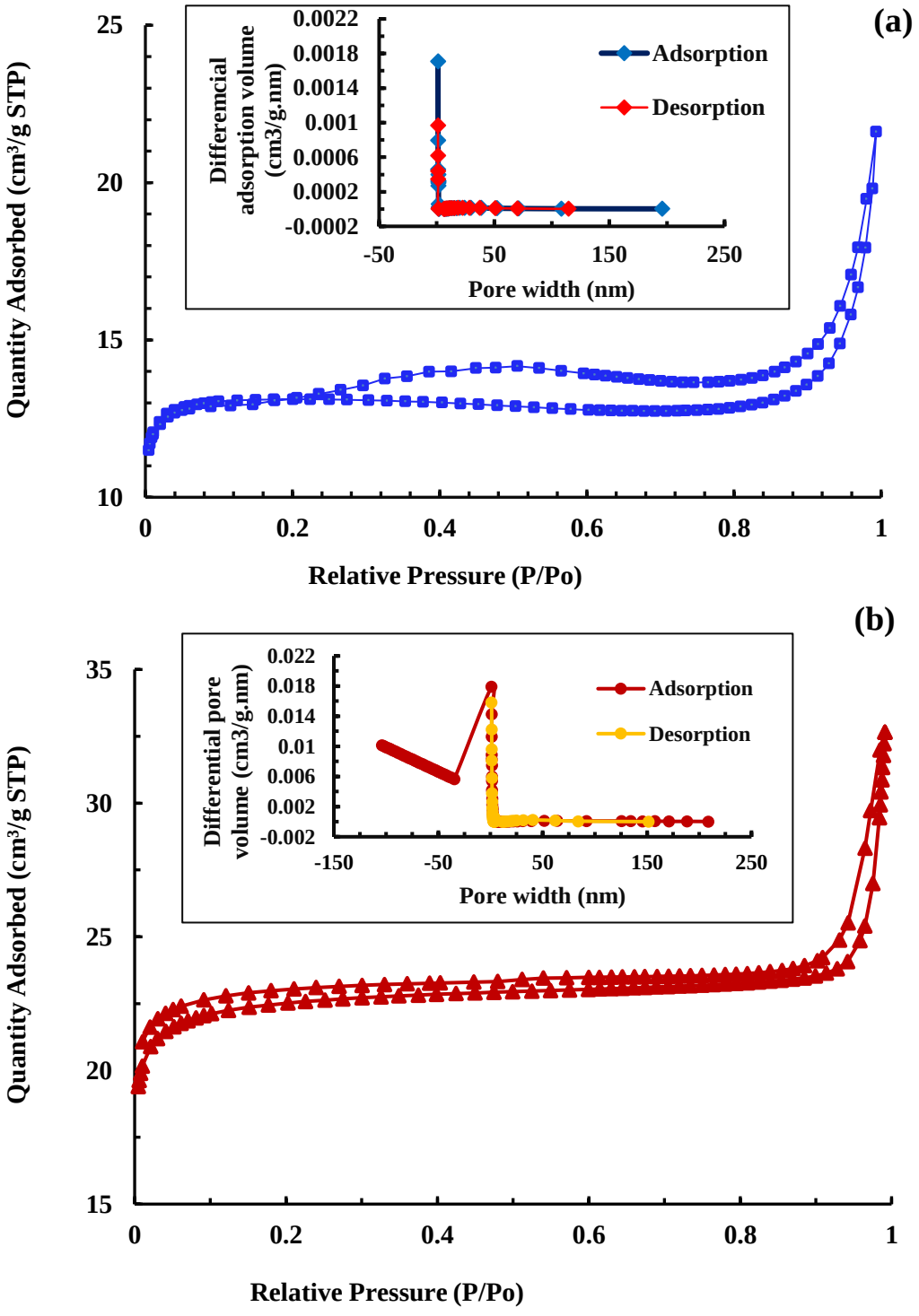

Figure 3.5: N_2 adsorption-desorption isotherm curves for (a) Ti-MOF, inset: Pore distribution curve of Ti-MOF; and (b) Zr-MOF materials, Inset: Pore distribution curve of Zr-MOF.

Thermo gravimetric analysis of Ti-MOF and Zr-MOF are displayed in Figure 3.6. The TGA curve of Ti-MOF reveals that below 200^0C, the solid loses its weight *Ca.* 10%, which is due to the elimination of remaining solvent molecules (DMF) from the pores, along with the removal of surface-absorbed moisture (H_2O). A substantial reduction in weight occurs within temperatures 350^0C to 470˚C, which is ascribed to the breakdown and thermal decomposition of the organic linkers that constitute the MOF structure of the solid. Further, temperatures *Ca.* 600˚C, the remaining component, TiO_2 exhibits high resistance to heat with almost no weight loss. (*Cf* Figure 3.6(a)). On the other hand, the Zr-MOF displays three stages of weight loss. (*Cf* Figure 3.6(b)). The first stage of weight loss (8.34%) occurred within a temperature range of 25-100^0C, which is due to the elimination of water or solvent from the solid. Further, a weight loss of 3.8% occurred within the temperature range of 100 to 420^0C due to the elimination of DMF and the dehydroxylation of the zirconium oxo-clusters (Yang et al., 2018). Moreover, the 41.6% weight loss of Zr-MOF occurred at temperature *Ca.* 500^0C, which is due to the thermal decomposition of organic linker molecules (Sun et al., 2019). Previously, it was reported that *Ca*. 500 °C the Ti-MOF and Zr-MOF networks lose their stability and the linker molecule seemingly decomposes (Sun et al., 2019; Yang et al., 2018). Specifically, TGA experiments indicate that benzene and CO_2 are the primary gas-phase decomposition products upon the breakdown of the framework (Solís et al., 2021; Valenzano et al., 2011).

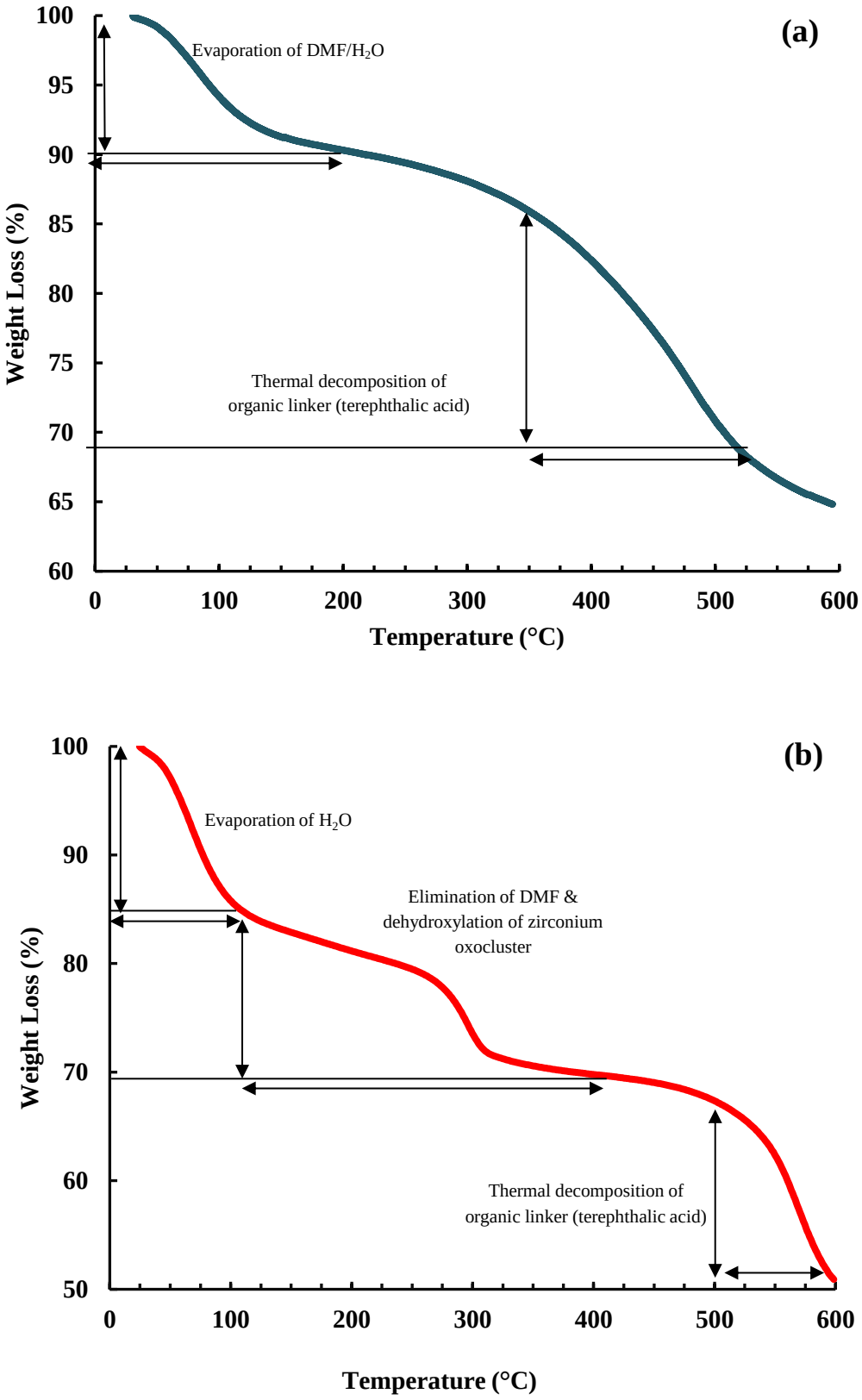

Figure 3.6: Thermo gravimetric analyses of (a) Ti-MOF; and (b) Zr-MOF materials.

X-ray photoelectron spectroscopy (XPS) is employed to investigate the elemental characteristics of the MOF. The XPS survey spectrum of Ti-MOF revealed the presence of Ti, O, C, and N elements in the Ti-MOF solid (*Cf* Figure 3.7(a)). Further, the XPS results demonstrate the chemical state of these elements. The deconvolution spectrum of Ti shows two distinct XPS peaks at the binding energies of 458.7 and 464.4 eV, referring to the Ti $2p_{1/2}$ and Ti $2p_{3/2}$, respectively, of the Ti(IV) (Solís et al., 2021) (Figure 3.7(b)). Moreover, the C1s shows four distinct peaks occurred at binding energies of 288.5, 286.8, 285.4, and 284.5 eV, referring to the C=O, C–C, C–N, and C=C, respectively, of the linker molecules (2-amino terephthalic acid) (*Cf* Figure 3.7(c)). The N1s peaks occurred at the binding energies of 399 and 401.2 eV, due to the presence of the amino ($-NH_2$) and positively charged nitrogen ($=NH^+$) (Song et al., 2019) (*Cf* Figure 3.7(d)). The deconvoluted peaks of O1s showed three distinct peaks appeared at 529.1, 531.5, and 532.8 eV, which are attributed to the titanium-oxo clusters, C=O bond, and OH group, respectively (Figure 3.7(e)) (Muelas-Ramos et al., 2021).

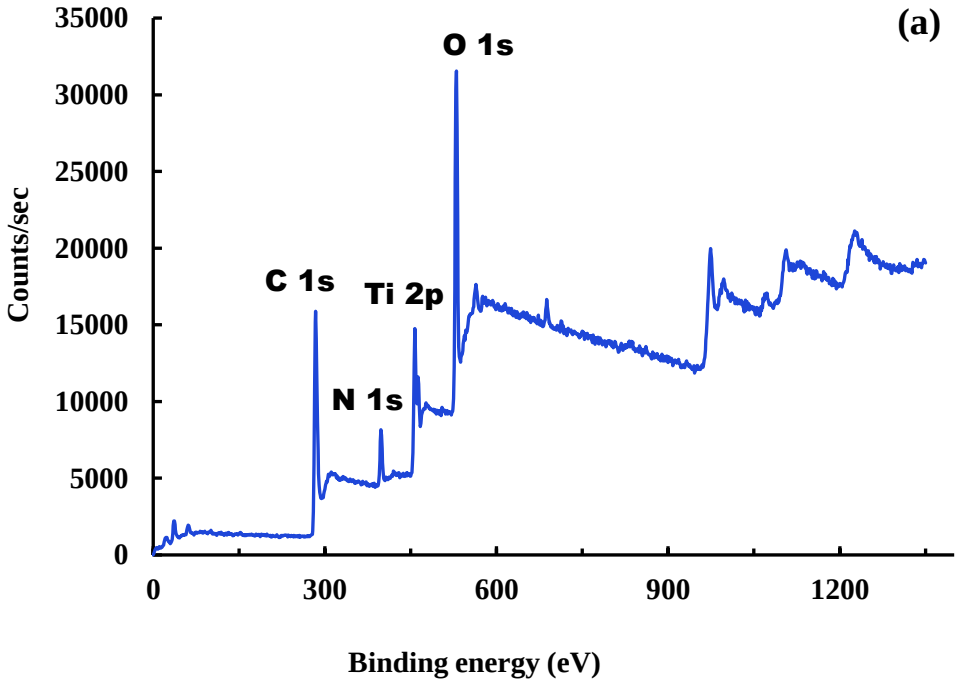

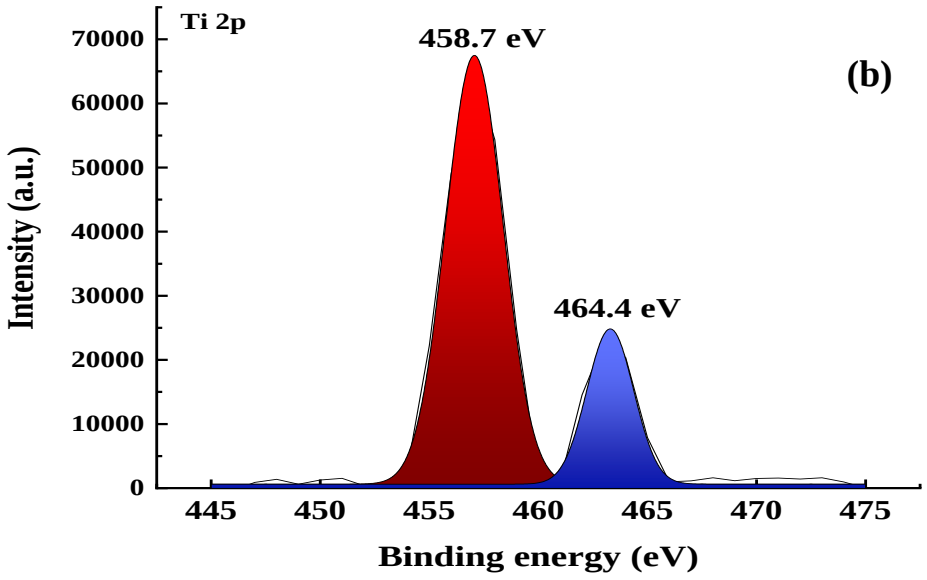
Ti 2p
458.7 eV
464.4 eV
(b)
Intensity (a.u.)
70000
60000
50000
40000
30000
20000
10000
0
445
450
455
460
465
470
475
Binding energy (eV)

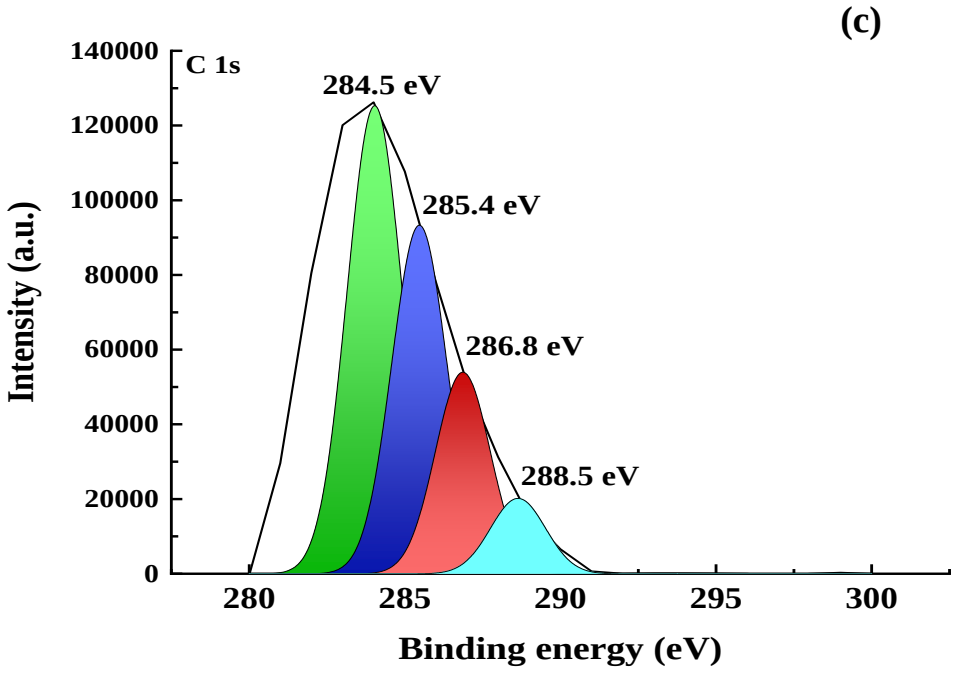
(c)
C 1s
284.5 eV
285.4 eV
286.8 eV
288.5 eV
Intensity (a.u.)
140000
120000
100000
80000
60000
40000
20000
0
280
285
290
295
300
Binding energy (eV)

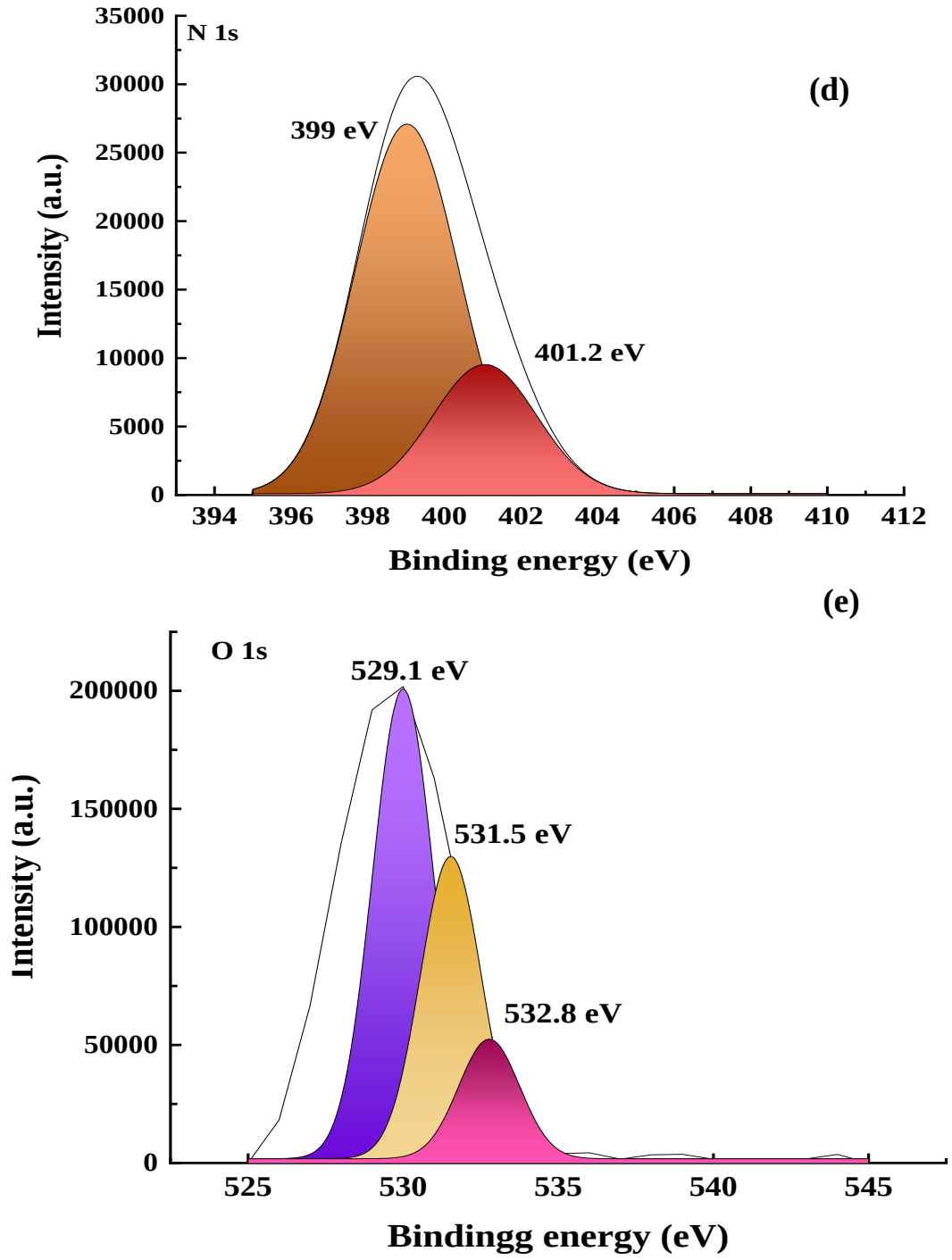

Figure 3.7: X-ray photoelectron spectrum of (a) Ti-MOF survey; deconvolution spectrum of (b) Ti; (c) C; (d) N; and (e) O elements in the Ti-MOF material.

Figure 3.8(a) displays the analysis of the XPS spectra of Zr-MOF. The comprehensive spectrum confirmed the presence of Zr, C, and O in the synthesized substance. The Zr 3d spectra (Figure 3.8(b)) exhibit two distinct peaks at 182.8 and

185.2 eV, which have been identified as Zr $3d_{5/2}$ and $3d_{3/2}$, respectively. This signifies the accomplished formation of Zr-O bonds within the metal cluster (Solís et al., 2022). The high-resolution spectra of C 1s (Figure 3.8(c)) indicate the presence of carbon species that are linked to the linker units. The deconvolution analysis revealed the presence of distinct aliphatic sp^3 C-C and C-H (284.3 eV), aromatic sp^2 C = C (285.5 eV), and O = C (288.7 eV) bonds (Yang et al., 2019). The deconvolution of the O 1s spectra (Figure 3.8(d)) demonstrates the existence of C = O (530.6 eV) and Zr-O (531.7 eV) species (Fang et al., 2020).

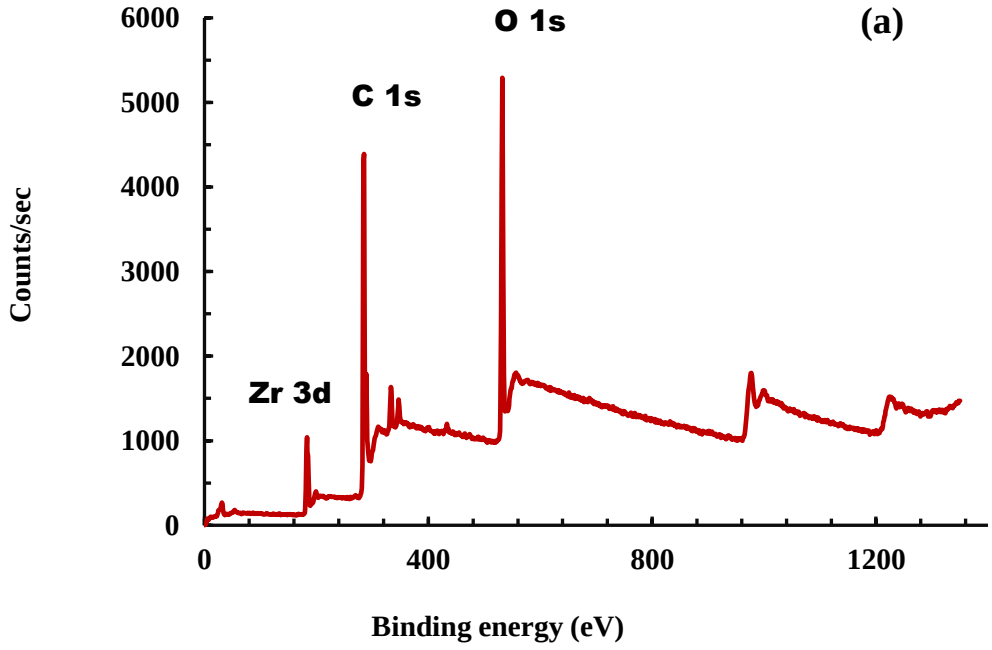

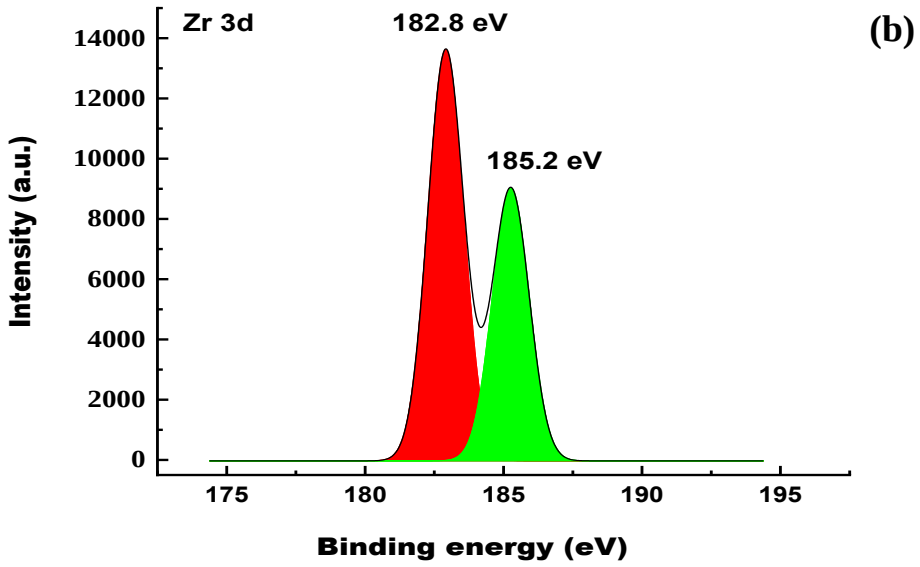
(b)
Zr 3d
182.8 eV
185.2 eV
Intensity (a.u.)
Binding energy (eV)
0
2000
4000
6000
8000
10000
12000
14000
175
180
185
190
195

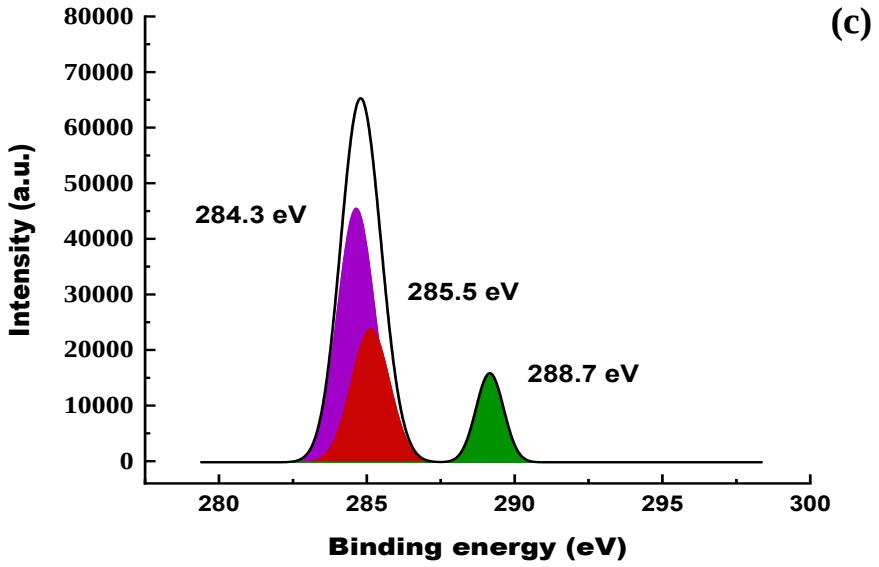
(c)
284.3 eV
285.5 eV
288.7 eV
Intensity (a.u.)
Binding energy (eV)
0
10000
20000
30000
40000
50000
60000
70000
80000
280
285
290
295
300

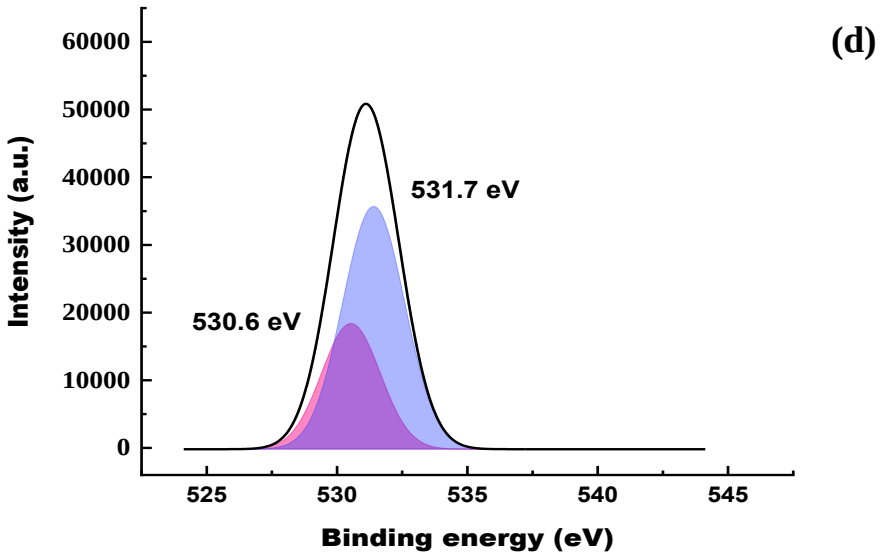

Figure 3.8: XPS Spectra of (a) Zr-MOF; Deconvolution spectra of (b)Zr3d, (c)C1s and (d) O1s.

3.2. ELECTROCHEMICAL CHARACTERISATION OF FABRICATED GLASSY CARBON ELECTRODES

3.2.1. Cyclic voltammetry (CV) studies

The electrochemical characterization of these thin film electrodes and bare glassy carbon electrodes was performed using cyclic voltammetry and electrochemical impedance spectroscopy. The cyclic voltammograms were obtained by measuring the electrical current as a function of the applied voltage using a conventional redox probe consisting of a 0.002 M solution of $[Fe(CN)_6]^{3-/4-}$ in 0.1 M KCl. The cyclic voltammograms (CV) are obtained at a scan rate of 100 mV/s and an excitation potential window ranging from -1.0 to 1.5 V. Figure 3.9 shows the cyclic voltammograms using the three different probes i.e., bare GCE, Ti-MOF/GCE, and Zr-MOF/GCE. The Ti-MOF/GCE and Zr-MOF/GCE probes show sharp and intense redox peaks for the $[Fe(CN)_6]^{3-/4-}$ redox couples. Nevertheless, the unmodified GCE exhibits redox peaks however, the redox peak currents are significantly decreased for

the $[Fe(CN)_6]^{3-/4-}$ redox couples. The higher redox peak current observed for the Ti-MOF/GCE and Zr-MOF/GCE is attributed to the enhanced electrical conductivity and the functional groups present with the MOFs facilitating the sorption of iron ions, which undergoes efficient oxidation and reduction of these ions (Yang & Gates, 2024) Moreover, the high specific surface area of these MOFs facilitate the sorption and oxidation-reduction of iron ions at the MOFs surface (Zhang et al., 2022). Further, the relatively higher peak current for the Ti-MOF/GCE than the Zr-MOF is, perhaps, due to the higher electrical conductivity of the Zr-MOF than the Ti-MOF solid. The redox peak potential difference (ΔE_p) values for the bare GCE, Ti-MOF/GCE, and Zr-MOF/GCE are 0.316, 0.285, and 0.254 V, respectively. Zr-MOF/GCE shows a relatively higher redox peak current with the lowest ΔE_p value. The lower ΔE_p value indicated an enhanced electron conductivity of the Zr-MOF/GCE (Luo et al., 2023). The titanium-based metal-organic framework modified with reduced graphene oxide (NH_2-MIL-125/RGO/GCE) revealed a notable redox peak current, accompanied by a potential difference of (ΔEp) of 0.094 V (Shu et al., 2023).

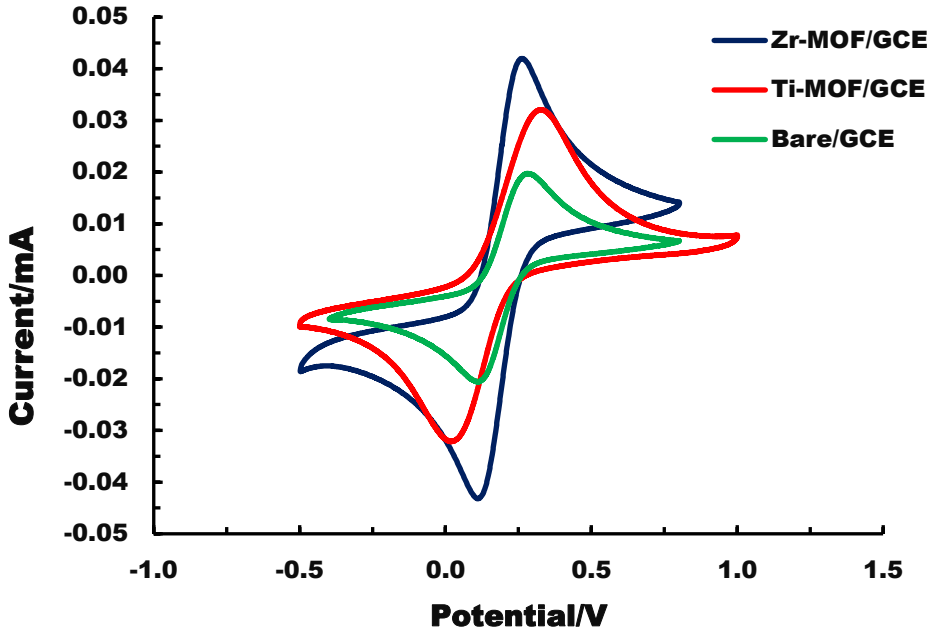

Figure 3.9: Cyclic voltammograms of $[Fe(CN)_6]^{3-/4-}$ (0.002 M; 0.1 M KCl) at a scan rate of 100 mV/s using the bare GCE, Ti-MOF/GCE, and Zr-MOF/GCE.

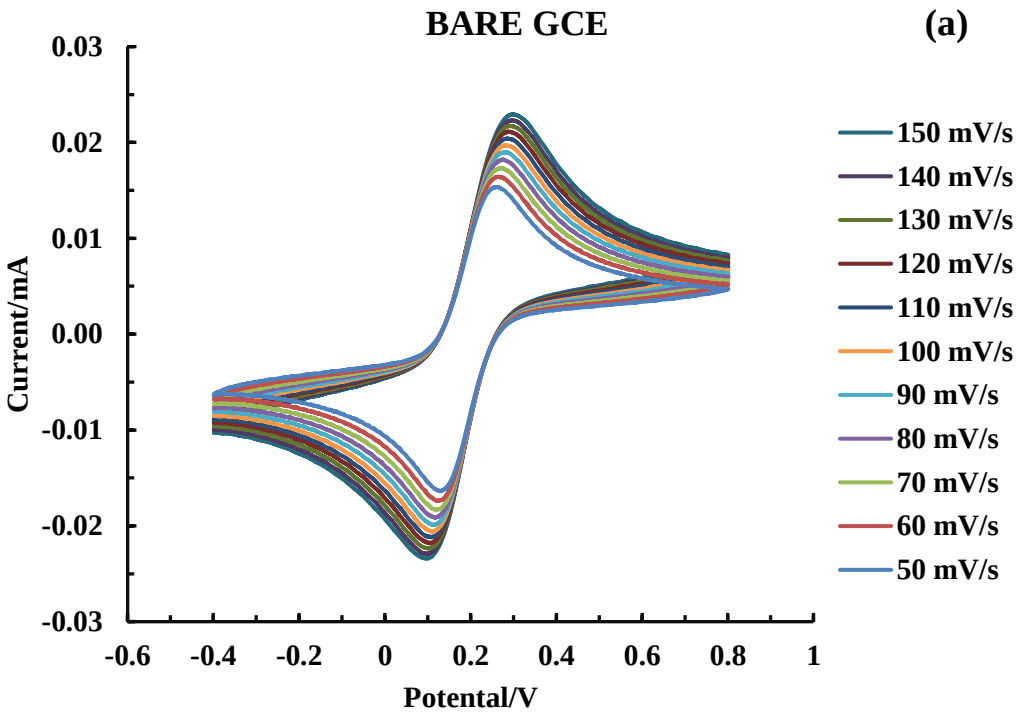
BARE GCE
(a)
0.03
0.02
0.01
0.00
-0.01
-0.02
-0.03
Current/mA
-0.6
-0.4
-0.2
0
0.2
0.4
0.6
0.8
1
Potental/V
150 mV/s
140 mV/s
130 mV/s
120 mV/s
110 mV/s
100 mV/s
90 mV/s
80 mV/s
70 mV/s
60 mV/s
50 mV/s

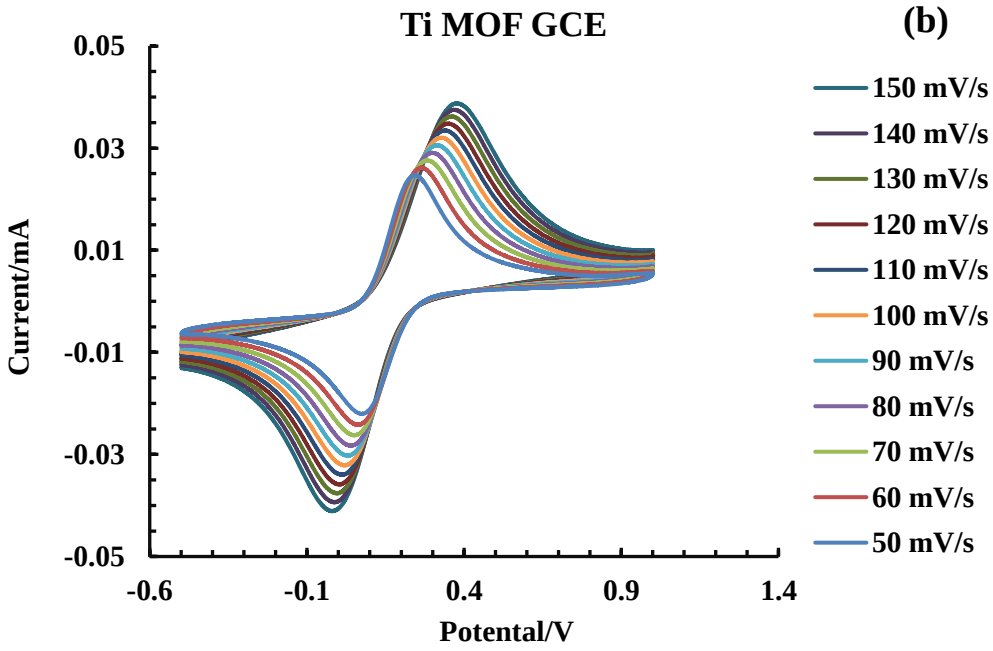
Ti MOF GCE
(b)
0.05
0.03
0.01
-0.01
-0.03
-0.05
Current/mA
-0.6
-0.1
0.4
0.9
1.4
Potental/V
150 mV/s
140 mV/s
130 mV/s
120 mV/s
110 mV/s
100 mV/s
90 mV/s
80 mV/s
70 mV/s
60 mV/s
50 mV/s

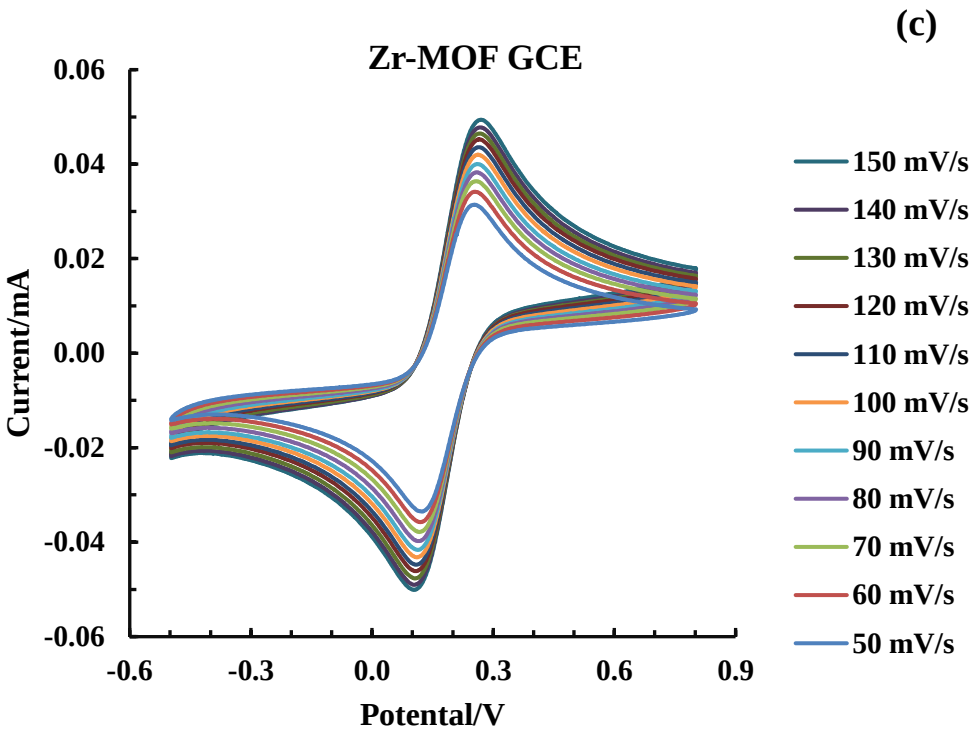

Figure 3.10: Scan rate studies for redox couple $[Fe(CN)_6]^{3-/4-}$ (0.002 M; 0.1 M KCl) using the (a) bare GCE; (b) Ti-MOF/GCE; and (c) Zr-MOF/GCE.

In addition, the scan rate studies are performed employing these electrodes for the standard redox couple $[Fe(CN)_6]^{3-/4-}$. The scan rate is varied from 50 mV/s to 150 mV/s at a constant concentration of 0.002 M $[Fe(CN)_6]^{3-/4-}$ in a 0.1 M KCl. Figure 3.10 shows the scan rate dependence cyclic voltammograms of these three different probes *viz*., GCE, Ti-MOF/GCE, and Zr-MOF/GCE. These results show that the redox peak currents of $[Fe(CN)_6]^{3-/4-}$ are dependent on the applied scan rates. Increasing the scan rate caused an increase in the redox peak currents. Figure 3.11 shows that increasing the square root of the scan rate ($v^{1/2}$) causes for linear increase in the peak current (I_p) using the bare GCE, Ti-MOF/GCE, and Zr-MOF/GCE. The linear relationship between the $v^{1/2}$ against the I_p indicates that the redox process is mainly controlled by diffusion and follows the Randle-Sevcik equation (Equation 2.2) (Zirlianngura et al., 2017). Further, using these straight lines the electroactive surface area of these electrodes is obtained using the Randle-Sevcik equation (eqn. 2), and the results are illustrated in Table 3.1. It is evident from the results that the electroactive surface area

of Ti-MOF/GCE and Zr-MOF/GCE is significantly increased compared to the bare GCE. The surface area of the Ti-MOF and Zr-MOF is increased by *Ca.* 1.5 and 2 times, respectively compared to the bare GCE. The electroactive surface area of the glassy carbon electrode, enhanced by the zeolitic imidazolate framework (ZIF-8), is twice as large as that of the unmodified electrode (Chu et al., 2019). An enhanced surface area provides more available electroactive sites on the surface of modified electrodes, which facilitates efficient electrochemical processes (Lalmalsawmi et al., 2020). The higher electroactive surface area of these MOFs modified GCEs could help in efficiently detecting the analytes at trace levels.

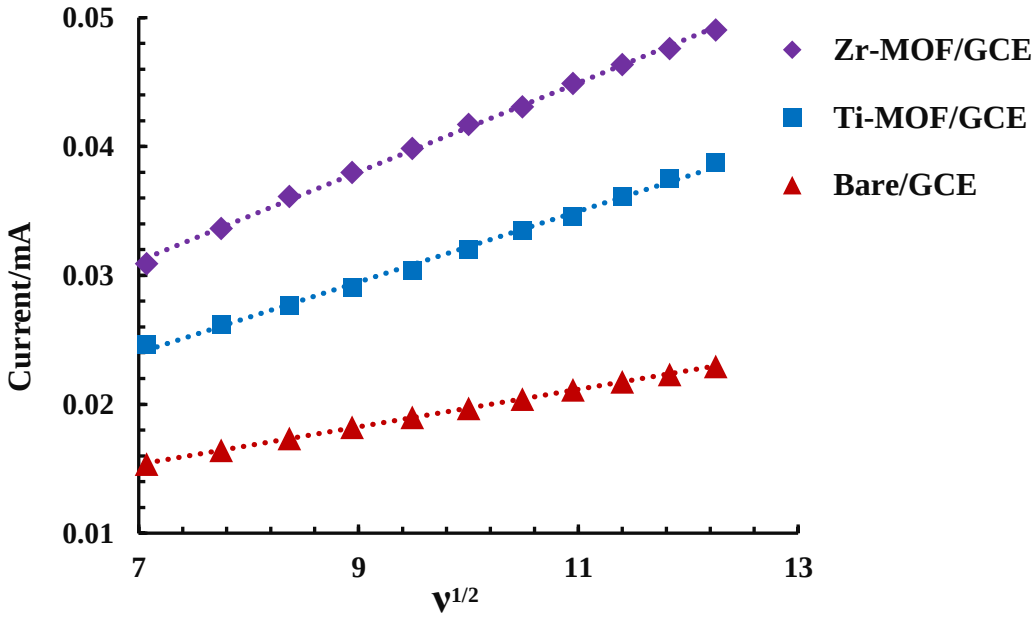

Figure 3.11: Plots of the square root of scan rate ($v^{1/2}$) *vs* I_p (peak current; anodic peak current) using different electrodes (bare GCE, Ti-MOF/GCE, and Zr-MOF/GCE) [0.002 M $[Fe(CN)_6]^{3-/4-}$ (0.1 M KCl)].

Table 3.1: Electroactive surface area of GCE, Ti-MOF/GCE, and Zr-MOF/GCE obtained by using the Randle-Sevick equation.

Electrodes used	Deduced Linear Equation	R^2	Electroactive Surface Area (mm^2)
Bare GCE	y = 0.0015x +0.0052	0.9997	8.95 x 10^{-4}
Ti-MOF/GCE	y = 0.0027x + 0.0048	0.9963	14.55 x 10^{-4}
Zr-MOF/GCE	y= 0.0035x + 0.0069	0.9989	18.90 x 10^{-4}

3.2.2. Electrochemical impedance spectroscopic (EIS) analyses of fabricated electrodes

The electron transfer behavior at the electrode surface is studied using these probes under electrochemical impedance spectroscopy. The study intends to utilize the redox pair of 0.002 M $[Fe(CN)_6]^{3-/4-}$ (0.1 M KCl) utilizing the frequency range from 80.0 kHz to 100.0 MHz, at a constant ratio of 6.0 per decade, and a sinusoidal potential of 10.0 mV peak to peak. Figure 3.12 shows the Nyquist plots of these electrodes having the imaginary impedance ($-I_m(Z)$/Ohm) *vs.* the real impedance ($R_e(Z)$/Ohm). Moreover, the figure 3.12 shows the Randles equivalent circuit of as:

$$R_s + \frac{C_{dl}}{R_{ct} + Z_W}$$

Where Z_w is the Warburg impedance, which is in series with the charge transfer resistance (R_{ct}), R_s is the solution resistance and the double layer capacitance (C_{dl}) occurs at the electrode surface and electrolyte interface region of each electrode (Sarikokba et al., 2022). Electron transfer resistance arises from the charge transfer reactions at the interface between the electrode and electrolyte. On the other hand, Warburg diffusion is due to the diffusion of ionic species into the surrounding solution (Lalmalsawmi et al., 2021). Table 3.2 includes the optimized values of the R_s and R_{ct} for these three electrodes. The results show that the solution resistance (R_s) of these

electrodes *viz.*, bare GCE, Ti-MOF/GCE, and Zr-MOF/GCE are nearly identical. Nevertheless, the considerable reduction in the size of the semicircles observed in the Nyquist plots for the Ti-MOF/GCE and Zr-MOF/GCE leads to a significant decrease in the R_{ct} values compared to the bare GCE (*Cf.* Figure 3.12). The R_{ct} values for the bare GCE, Ti-MOF/GCE, and Zr-MOF GCE are 6696 Ω, 2198 Ω, and 539 Ω, respectively. The decrease in semicircle for the Ti-MOF/GCE and Zr-MOF/GCE is attributed to the presence of metals within the material, which enhances the efficiency of electron transfer reactions at the electrode surface. Additionally, the Zr-MOF/GCE resulted in a greater reduction in semicircle compared to Ti-MOF/GCE, attributed to an enhanced electrical conductivity of material. This enhanced conductivity promoted the charge transfer reactions at the electrode/electrolyte interface.

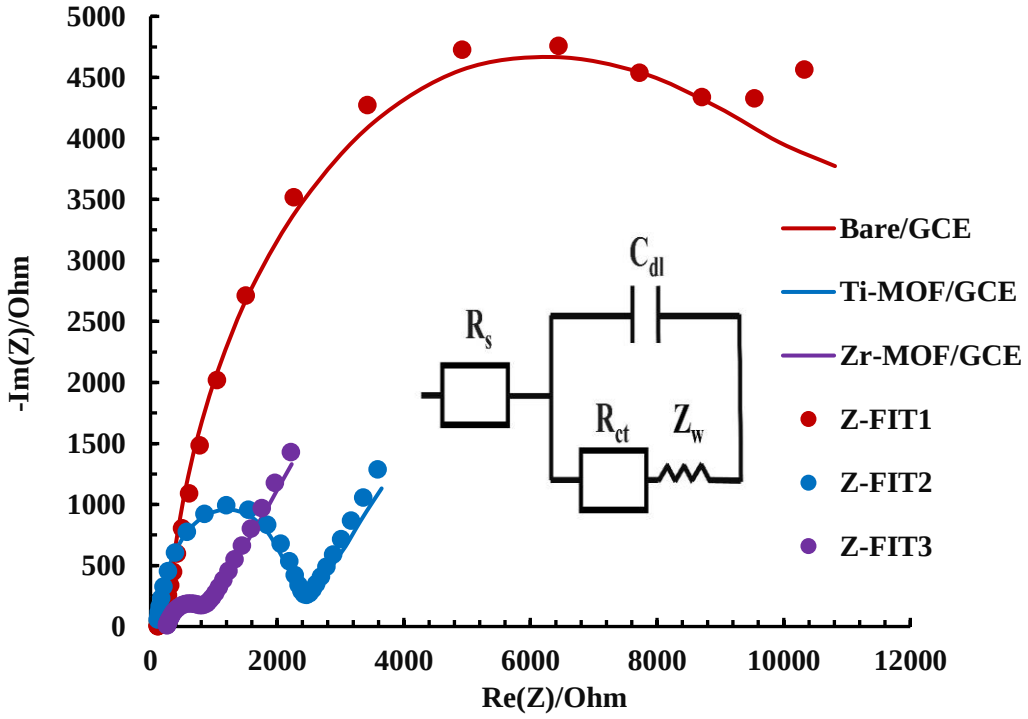

Figure 3.12: Nyquist plots of bare GCE, Ti-MOF/GCE, and Zr-MOF/GCE with Z_{fit} modified GCE using the standard probe of $[Fe(CN)_6]^{3-/4-}$(0.002 M; 0.1 M KCl) [Inset: Fitted equivalent circuit].

Table 3.2: The optimized EIS parameters for the best fitted electrical circuit for the Nyquist plots using the bare GCE, Ti-MOF/GCE and Zr-MOF/GCE probes.

Working Electrodes	Parameters	
	R_s (Ω)	R_{ct} (Ω)
Bare GCE	110	6696
Ti-MOF/GCE	103	2198
Zr-MOF/GCE	115	539

3.3. ELECTROCHEMICAL DETERMINATION OF As(III) USING METAL ORGANIC FRAMEWORKS

3.3.1. Electrochemical behaviour of As(III) using Ti-MOF/GCE under DPASV

The technique of differential pulse anodic stripping voltammetry (DPASV) is employed to analyze the presence of As(III) in aqueous solutions utilizing the Ti-MOF/GCE. The As(III) is analysed in 0.1 M acetate buffer solution (pH 3) having As(III) concentration of 25.0 µg/L. Further, the deposition potential and time are applied to -1.2 V, and 60 sec, respectively. Figure 3.13 displays the DPASV curves of As(III) using both the bare GCE and the Ti-MOF/GCE probes. The results demonstrate that the bare GCE exhibits no oxidative peak current, suggesting that it has little or no affinity for As(III). However, the Ti-MOF/GCE shows a significant peak current at around -0.091 V potential. This indicates that Ti-MOF has a strong affinity for As(III) and undergoes oxidation at the electrode surface. The Ti-MOF possesses amino and hydroxyl groups, which allows for forming bonds with the As(III) and leads to an increase in the oxidative peak current (Chen et al., 2020). Additionally, the high specific surface area of MOF with meso-porosity provides enhanced space for the sorption of As(III), which readily undergoes oxidation and shows enhanced oxidative current (Kuppusamy et al., 2023). The large surface area and higher electrical

conductivity of the Fe-MOF/MXene electrode detects efficiently the arsenite and the XPS analysis reveals that the As-hydroxyl bonded at the Fe-MOF/MXene surface (Xiao et al., 2022).

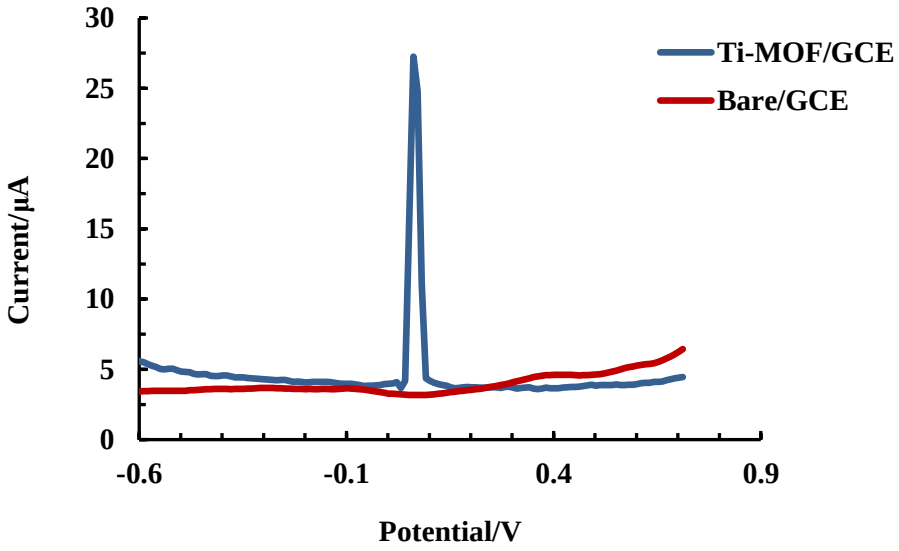

Figure 3.13: DPASV curves obtained for As(III) [25.0 µg/L at pH 3; acetate buffer (0.1 M)] using the bare GCE; and Ti-MOF/GCE.

3.3.2. Optimization of experimental parameters

Optimizing input parameters provides the sensitive, selective, and enhanced electrochemical signals of As(III) detection. An amplified and distinguishable signal facilitates the identification of analytes at trace detection. Consequently, the optimization and preconcentration experiments for the parameters *viz.*, pH, deposition potential, and deposition time are studied in the detection of As(III) in 0.1 M acetate buffer at an initial As(III) concentration of 25.0 µg/L. The other electronic controls, namely pulse amplitude (0.05 V), step potential (0.0001 V), modulation time (0.05 sec), and time interval (0.5 sec) are kept constant.

3.3.3. Effect of pH

The electrochemical behavior of analytes is significantly altered by solution pH, due to the protonation/deprotonation and hydrolysis of the analyte species. The oxidation of As(III) is studied over a broad pH range (2.0 to 7.0), while maintaining the deposition potential (-1.20 V), deposition period (60.0 sec), and As(III) concentration (25 µg/L). Figure 3.14(a) depicts differential pulse anodic stripping voltammetric (DPASV) peak current values against different pH values, which reveal that the stripping peak current (I_p) increases until pH 3.0 and decreases gradually with an increase in pH from 3.0 to 7.0. A slight decline in peak current at pH<3, which is primarily because at lower pH values the hydrogen evolution suppresses the oxidation of As(III). Hence, lower pH decreases peak current. Additionally, the active sites of the working electrode dominate with hydrogen ions and inhibit partly the accumulation of As(III) at the electrode surface, which causes for decrease in peak current at lower pH values. The As(III) ions sorb onto the electrode surface and engaged in redox processes upon anodic stripping. Figure 3.14(b) shows that As(III) exists to its uncharged species of H_3AsO_3 up to pH 8.0 and at pH>8.0 the acidic dissociation caused the negatively charged $H_2AsO_3^-$ and $HAsO_3^{2-}$ species. The higher affinity of MOF towards the As(III) species leads to an enhanced peak current. However, an increase in pH (pH>3.0) gradually caused for decrease in peak current. The decrease in peak current is due to the relatively less sorption of the arsenic species with the negatively charged Ti-MOF (pH_{PZC} = 4.2) surface. This feeble sorption of arsenic species at the electrode surface, caused for decrease in peak current. Consequently, pH 3.0 is an optimal pH for the ensuing electrochemical study.

3.3.4. Effect of deposition potential

The deposition potential is a crucial parameter in the stripping analysis since it enhances the sensitivity of detection. The deposition potential is investigated over a potential range of -1.3 to -0.9 V, while maintaining other parameters constant, such as pH (3.0), deposition period (60 sec), and As(III) concentration of 25.0 µg/L in a 0.1 M acetate buffer solution. The results depicting the dependence of deposition potential are shown in Figure 3.14 (c). Figure 3.14 (c) shows that the increase in deposition

potential from -1.3 to -1.0 V, the stripping peak current (Ip) increases from 15.36 to 22.06 µA, respectively. Nevertheless, a subsequent increase in deposition potential from -1.1 to -0.9 V resulted in a decrease in peak current from 22.06 to 12.02 µA, respectively. The reduction in stripping peak current is ascribed to the generation of hydrogen gas in the medium at higher applied potentials. Hence, an optimal deposition potential is -1.2 V.

3.3.5. Effect of deposition time

Similarly, the deposition time in the detection of As(III) is studied for a wide range of deposition time 30 sec to 180 sec at pH 3, deposition potential of -1.2 V, and As(III) concentration of 25.0 µg/L in a 0.1 M acetate buffer. Figure 3.14 (d) shows that increasing the deposition time from 30 to 60 sec caused an increase in the stripping peak current (Ip) from 14.42 to 22.48 µA, respectively. Nevertheless, a further increase in deposition time beyond 60 sec resulted in a decline in the peak current. The drop in peak current observed with longer deposition time is attributed to the saturation of active sites on the surface of Ti-MOF/GCE. Hence, a deposition period of 60 sec is selected for the electrochemical detection of As(III).

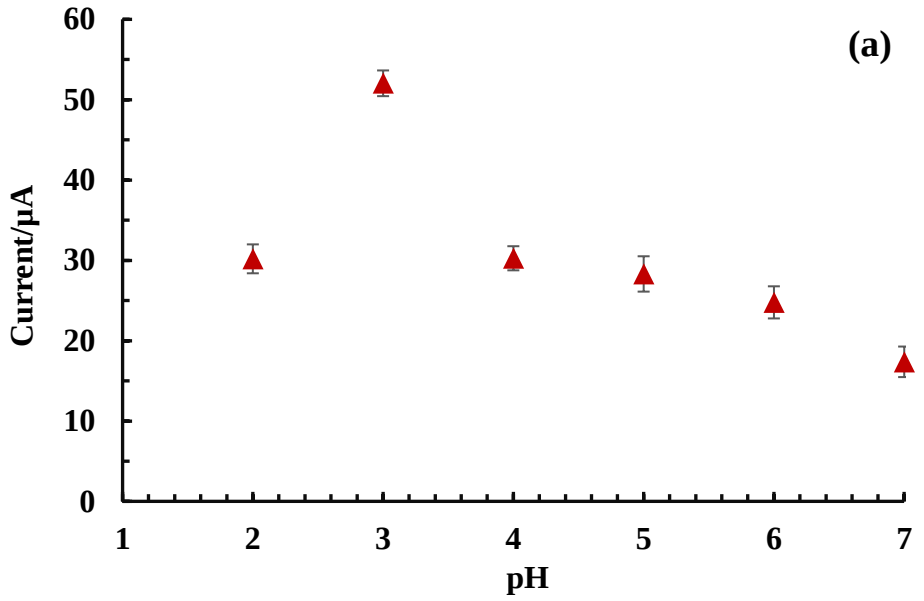

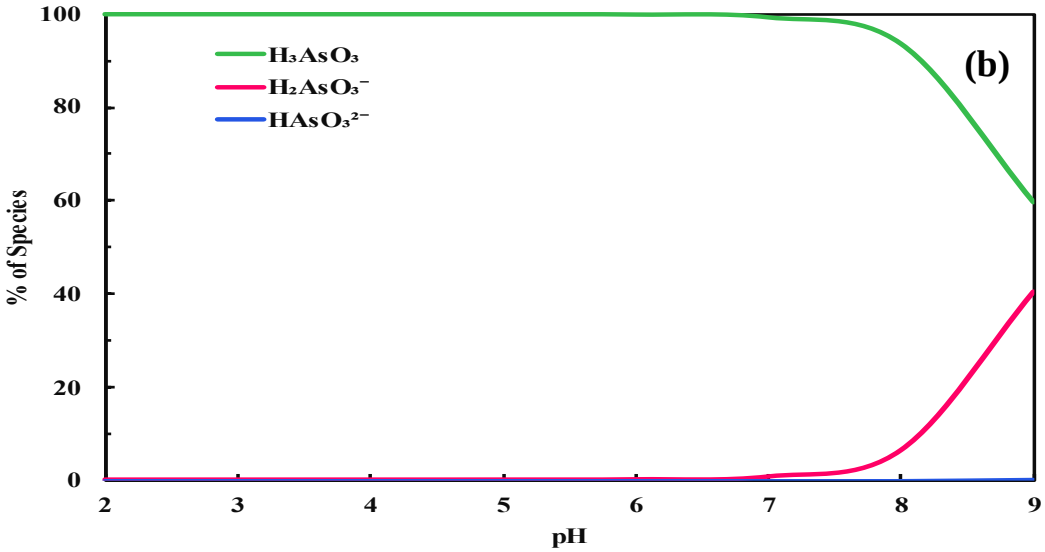
100
80
60
40
20
0
% of Species
H₃AsO₃
H₂AsO₃⁻
HAsO₃²⁻
(b)
2
3
4
5
6
7
8
9
pH

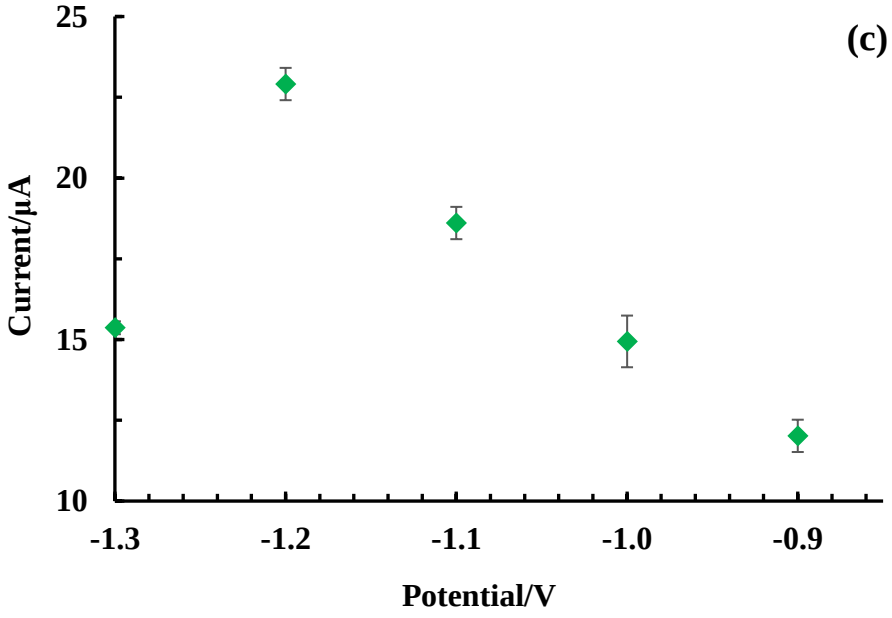
25
20
15
10
Current/μA
(c)
-1.3
-1.2
-1.1
-1.0
-0.9
Potential/V

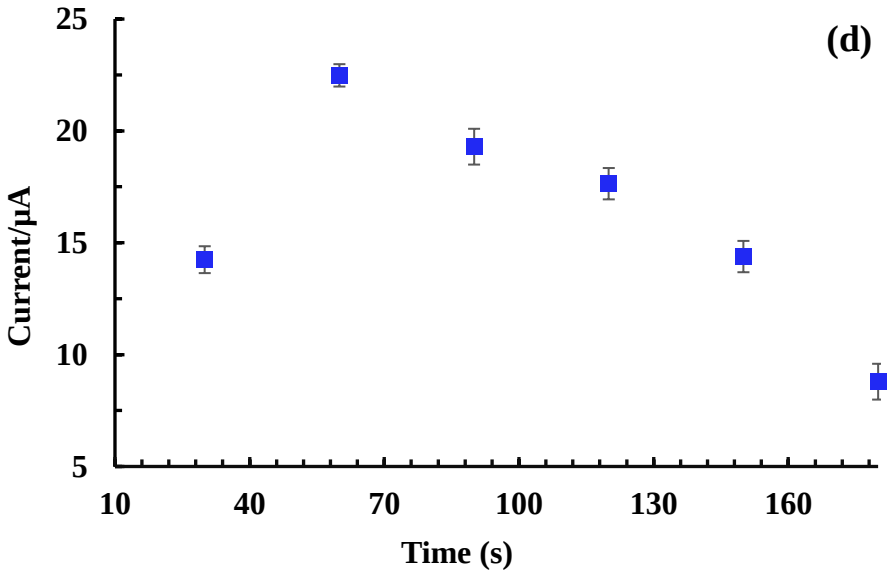

Figure 3.14: Parametric studies carried out for the detection of As(III) (25.0 µg/L As(III)) and the oxidative peak current is represented as a function of (a) the pH; (b) Speciation of arsenic species; (c) deposition potential; and (d) the deposition time.

3.3.6. Electrochemical determination of As(III)

The optimized parameters (pH 3; deposition potential -1.2 V, and deposition period 60.0 sec) were applied in the detection of As(III) in an aqueous medium using DPASV measurements. The Ti-MOF/GCE probe records the oxidative peak currents at different concentrations of As(III). An intense and well-defined oxidative peak of As(III) is obtained at an applied potential of -1.2 V. Moreover, figure 3.15(a & b) demonstrates that the gradual increase in As(III) concentration caused an increase in oxidative peak currents. Therefore, the peak current is primarily dependent on the bulk concentration of As(III), which implies that the oxidation of the As(III) at the electrode surface is diffusion-controlled (Shakkthivel & Singh, 2007). Hence, the oxidation peak current is a dependent parameter in obtaining the calibration curve for the detection of As(III).

Further, a linear relationship is obtained between the oxidative peak current and the corresponding As(III) concentrations for two different concentration ranges

viz., 5.0 to 25.0 µg/L and 0.2 to 1.0 µg/L (*Cf* Figure 3.15(a) and 3.15(b)). The calibration line is depicted in Figure 3.15 (a & b) (insets). The calibration line is represented by the equation y(µA) = 0.8908x(µg/L) + 4.824, with R^2 value of 0.9982 and y(µA) = 3.85x(µg/L) + 5.894, with a R^2 value of 0.9916 for the As(III) concentration range of 5.0 to 25.0 and 0.2 to 1.0 µg/L, respectively. The coefficient of determination (R^2) possesses a high value, indicating the fair relation of these dependent and independent parameters. The linear equations determine the LOD and LOQ values and are found to be 0.04 and 0.15 µg/L, respectively, for the As(III) concentration range 5.0 to 25.0. Similarly, for the As(III) concentration range 0.2 to 1.0 µg/L the LOD and LOQ values are 0.01 and 0.03 µg/L, respectively. These values are significantly below the permissible limit of lead in drinking water established by the World Health Organization (WHO), which is 10.0 µg/L.

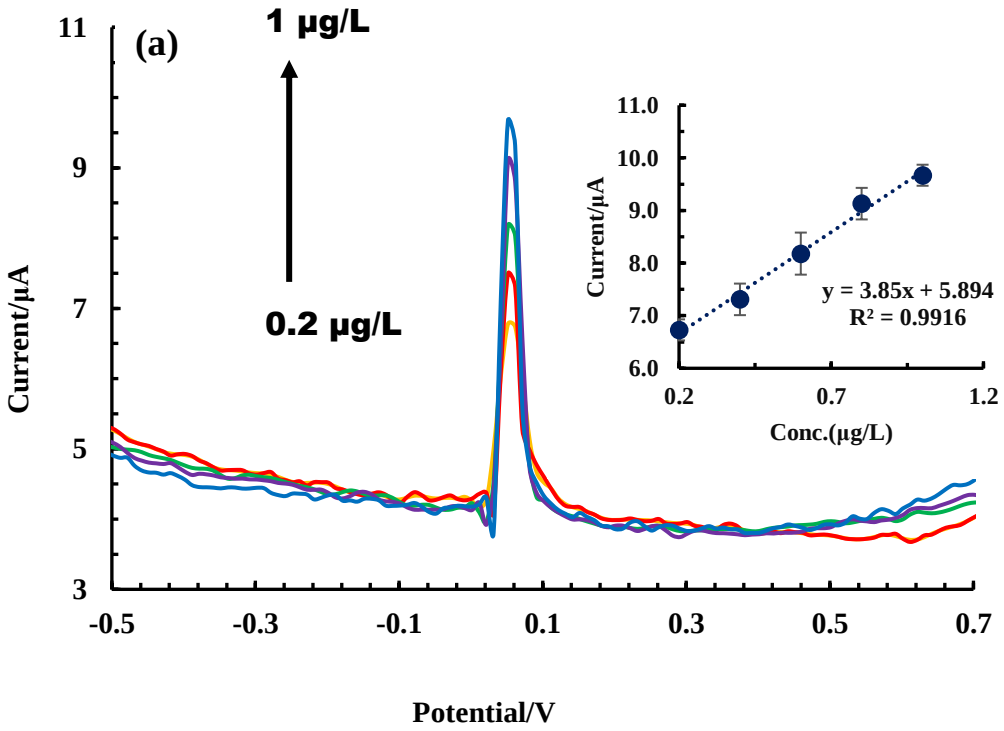

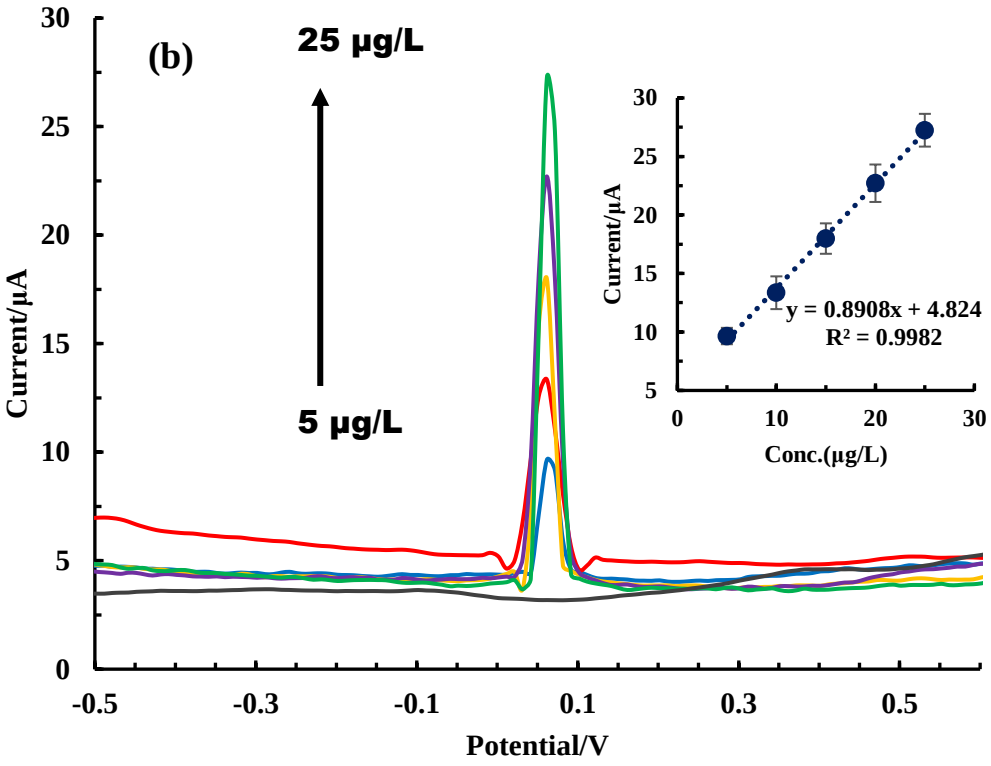

Figure 3.15: The differential pulse anodic stripping voltammograms are obtained for the As(III) concentration range (a) 0.2 to 1.0 µg/L; and (b) 5.0 to 25.0 µg/L; Insets: Calibration lines obtained for the oxidative peak current of As(III) at a concentration range of (a) 0.2 to 1.0 µg/L; and (b) 5.0 to 25.0 µg/L.

Table 3.3 compares the LOD values for As(III) utilizing different materials in the literature. The table reveals that the Ti-MOF showed an enhanced detection limit for the detection of As(III) compared to several other materials.

Table 3.3: Detection of As(III) using different materials.

Materials	**Method**	**pH**	**Linear range (µg/L)**	**LOD (µg/L)**	**Reference**
Au-PANI-Fe-CNF	SWASV	5	5-400	0.5	(Tang et al., 2020)
Fe_3O_4/Co_3S_4	SWASV	6	1–10	0.69	(Huang et al., 2022)
Mn_2O_3/CeO_2	SWASV	4	10-80	3.35	(Ren et al., 2018)
Fe_3O_4/rGO	DPASV	3	1-20	1.19	(Hu et al., 2021)
SnO_2 Nano sheets	SWASV	5	5-300	4.6	(Jiang et al., 2016)
ZrO_2/Nafion/Au electrode	CV	7.4	5-60	5	(Bhanjana et al., 2016)
Gold film/plastic electrode	DPASV	3	5-150	5	(Wang et al., 2019)
Ti-MOF	**DPASV**	**3**	**0.2- 25**	**0.01**	**Present studies**

3.3.7. Effect of co-existing ions

The study further investigates the effect of several co-existing cation/anions (each 250.0 µg/L in detecting the As(III) (25.0 µg/L). Figure 3.16 depicts the As(III) peak current in the presence of these ions (Ca^{2+}, Mg^{2+}, Cu^{2+}, F^-, Cl^-, and NO_3^-) along with the blank As(III). The results demonstrate that fluoride and copper cause a slight increase in peak current for As(III), which is due to the comparable deposition potential of $Cu^{2+}$and F^- ions at similar potential, increasing the oxidative peak current (Thiruppathi et al., 2023). However, the presence of other ions *viz*., Ca^{2+}, Mg^{2+}, Cl^-, and NO_3^- did not influence the detection of As(III) in an aqueous medium. The obtained results demonstrate the specificity of Ti-MOF/GCE in detecting As(III) in an aqueous solution. Moreover, the Ti-MOF/GCE is reasonably selective in detecting the As(III) at a trace level.

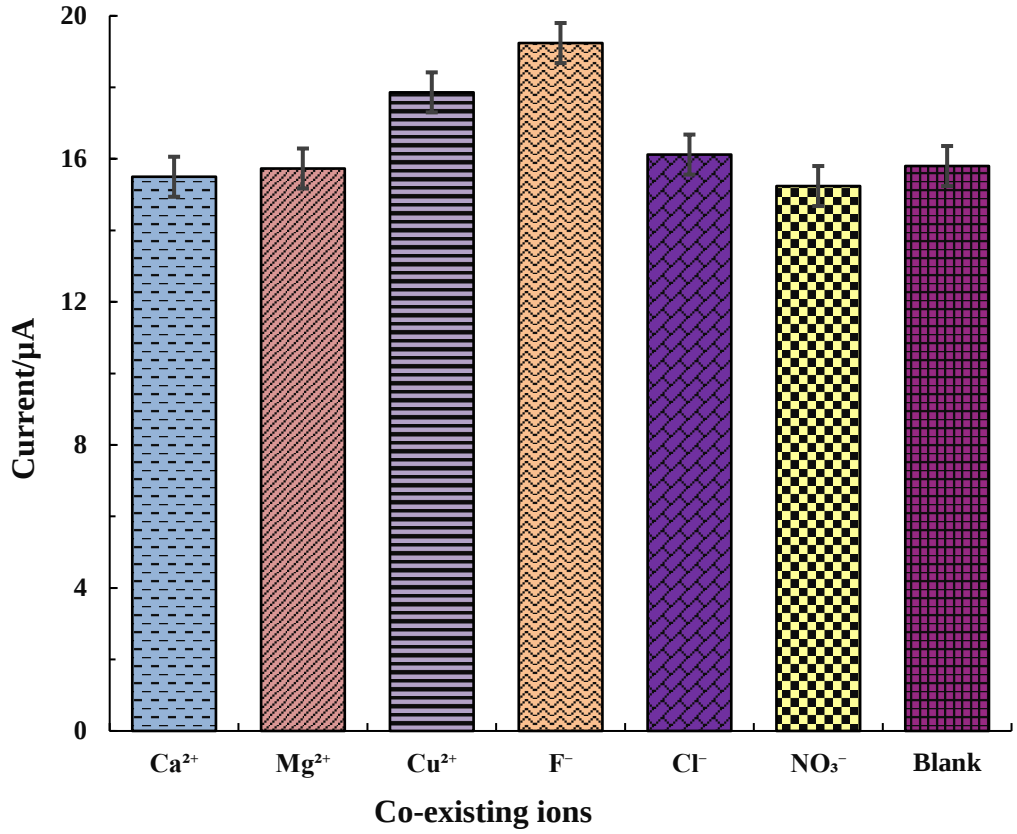

Figure 3.16: The detection of As(III) in the presence of several co-existing ions using the Ti-MOF/GCE ([As(III): 25.0 µg/L; [Interfering ion]: 250.0 µg/L).

3.3.8. Reproducibility and stability electrode

The reproducibility/repeatability test is conducted by taking 10 repeated detections (n=10) of As(III) (25.0 µg/L) using the Ti-MOF/GCE probe under previously optimized conditions of DPASV. The relative standard deviation (RSD(%)) is determined, which is always less than 2.52%. The low value of RSD(%) suggests that the electrochemical probe has the potential to be reused for repeated detection of As(III) in aqueous medium. Figure 3.17 shows the electrode's reusability tests for various time intervals i.e., 0, 12, 24, and 48 hrs in the detection of As(III) 25.0 µg/L. Each time, five consecutive detections of As(III) are conducted, and again the RSD (%) is obtained and shown in Table 3.4. The low value of RSD (%) infers the stability

of the Ti-MOF/GCE probe for repeated and prolonged use in the detection of As(III). Previously, the reusability performance of NH_2-MIL-125(Ti) was performed by immersing the electrode in the Cu(II) solution for 5 minutes, followed by extensive washings with ethanol and water. Results showed that the peak currents were not significantly altered for five successive cycles for Cu(II) detection. These results thereby confirm that titanium does not leach from NH_2-MIL-125(Ti) post-quantification of Cu(II) ions confirming the stability of Ti-MOF (Kaur et al., 2020).

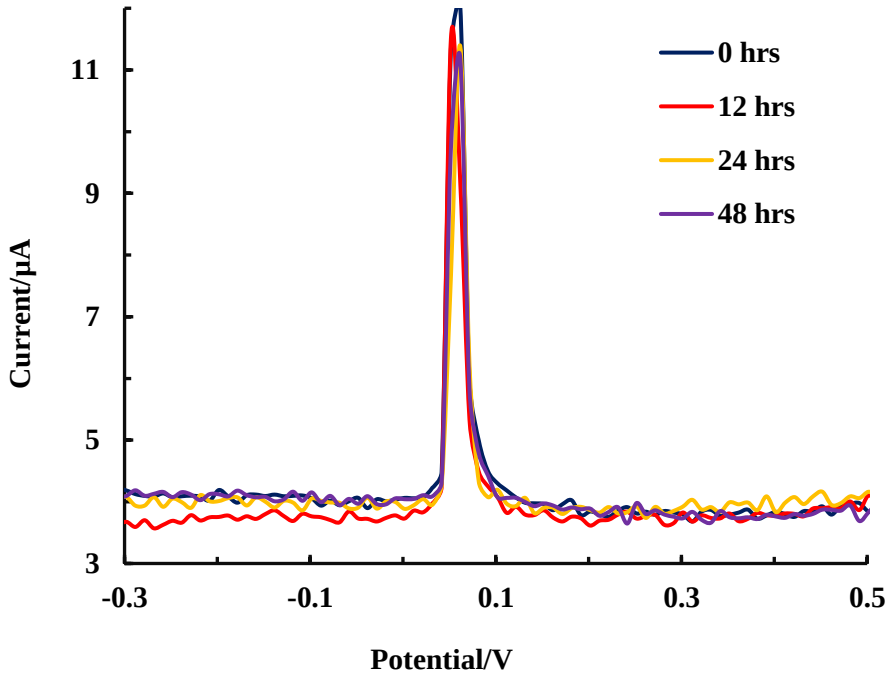

Figure 3.17: The detection of As(III) for different time intervals using the Ti-MOF/GCE (As(III): 25.0 μg/L, pH 3.0).

Table 3.4: Relative standard deviations (%) for the detection of As(III) at different time intervals for the detection of As(III) (25.0 μg/L) from aqueous solution.

Time duration (hrs)	RSD (%)
0	0.210
12	0.345
24	0.170
48	0.255

3.3.9. Natural water sample analysis

The Ti-MOF/GCE assesses the implacability of As(III) detection in real water samples. Table 3.5 shows various physicochemical parametric results of Chite River water. Table 3.5 shows that the water sample contains substantial quantities of calcium and nitrate. Moreover, the TOC analysis reveals that the water sample contains a significant amount of inorganic and organic carbon contents. The presence of inorganic carbon with a higher content of calcium indicated that the sample contains the carbonates or bicarbonates of calcium. These findings suggest that the river water sample exhibits water hardness. A known amount of As(III) is spiked in the river water sample for various As(III) concentrations (5.0 – 25.0 μg/L) at pH 3.0. Figure 3.18 shows the differential pulse response for varied concentrations of As(III), which infers that an increase in As(III) concentrations causes a gradual increase in peak currents. Further, figure 3.18(inset) depicts the linear calibration line with the linear equation of y (μA) = 0.5577 x (mg/L) + 9.5905 (R^2 = 0.992). Further, the LOD and LOQ of detection are 0.07 μg/L and 0.24 μg/L, respectively. These results infer that the Ti-MOF/GCE is promising in As(III) detection in real water samples.

Additionally, the percentage of As(III) recovery is computed for the river water sample, and returned in table 3.6. Table 3.6 demonstrates that the device detects As(III) efficiently with relatively very high recovery rates. The recovery percentage ranged from 88.4% to 107.5% for As(III) in river water samples. The Cu3P50@NH2-MIL-125(Ti)/GCE detects the hydrazine in the three different water samples *viz.*,. Distilled water, tap water, and river water spiked with known concentrations of 100, 300, and 500 µM hydrazine. The average recovery rates were achieved at 90.3% and 103.3% for distilled water, 96.0% to 105.1% for tap water, and 99.6% to 106.2% for river water, with a relative standard deviation (RSD) below 3.94% (Wang et al., 2018).

Table 3.5: Various parametric studies of Chite river water samples using different analytical tools.

Parameters Studied	**Analytical Results**
pH	7.28
Conductivity	127 mS/cm
Resistivity	0.0085 mOhm.cm
Salinity	0.69 PSU
Ox. Red. Potential	204.3 mV
Alkalinity	151 mg/L
Al^{3+}	0.03 mg/L
NO_3^-	39.1 mg/L
SO_4^{2-}	17.0 mg/L
PO_4^{3-}	1.80 mg/L
F^-	BDL

AAS analysis	
Mg	16 mg/L
Ca	203 mg/L
Ni	BDL
TOC Analysis (mg/L)	
Inorganic Carbon	36.40
NPOC	39.35

BDL: Below detection limit

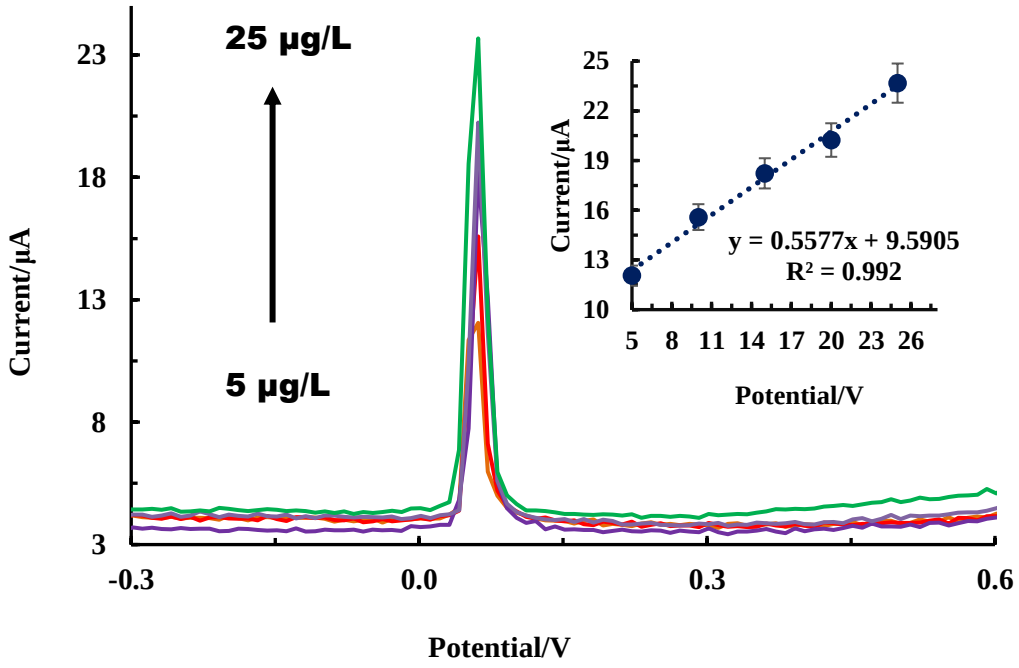

Figure 3.18: Real water sample spiked with As(III) having concentrations from 5.0 to 25.0 µg/L (Acetate buffer 0.1 M; pH 3), DPASV of As(III) using the groundwater; Inset: Calibration lines obtained for groundwater samples.

Table 3.6: The recovery of As(III) in the spiked spring water and groundwater using Ti-MOF/GCE.

Real sample	Spiked amount (µg/L)	Found (µg/L)	Recovery (%)
Groundwater	5.0	4.42	88.4
	10.0	10.75	107.5
	15.0	15.48	103.2
	20.0	19.08	95.4
	25.0	25.24	100.1

3.3.10. Conclusion

A facile hydrothermal one-pot method synthesizes a novel titanium-based metal organic framework precursor to the titanium and 2-amino terephthalic acid. Highly porous Ti-MOF possesses a very high surface area of 1040.83 m^2/g and shows that TiO_2's monoclinic cubic structure primarily possesses the anatase phase. The average geometric particle size is 6.36 nm and the geometric mean surface roughness is 8.03 nm, and the synthesized solid is thermally stable until 600°C. Ti exists with a +4 oxidation state i.e., Ti(IV) in the Ti-MOF and bonded with the 2-amino terephthalic acid. Ti-MOF fabricated electrode showed *Ca* 2 times higher electroactive surface area and *Ca.* 3 times lower charge transfer resistance than the GCE, which enabled to significant enhancement of the electrochemical response for As(III). The DPASV optimizes the As(III) detection at pH, deposition potential, and deposition time, 3.0, -1.2 V, and 60 sec, respectively. Electrochemical detection of As(III) within the concentration range (5 - 25) µg/L showed a good calibration line with the straight line equation of $y(\mu A) = 0.8908x(mg/L) + 4.824$ ($R^2 = 0.9982$) with LOD and LOQ of 0.04

and 0.15 µg/L respectively. Similarly for the As(III) concentration range (0.1-1.0 µg/L), a separate calibration line is obtained with a linear equation of y(µA) =3.85x(mg/L) +5.894 (R^2 = 0.9916). The LOD and LOQ are 0.01 and 0.03 µg/L, respectively. The presence of several ions *viz.*, Ca^{2+}, Mg^{2+}, Cl^-, and NO_3^- could not affect significantly the As(III) detection. However, the presence of Cu^{2+}, and F^- affected the detection of As(III) using the Ti-MOF/GCE. Further, the recovery rate of As(III) in river water lies between 88.4% to 107.5%, and the Ti-MOF electrode is stable for 10 repeated detection cycles. The studies infer the potential of Ti-MOF for miniaturized device development for detecting the As(III).

3.4. ELECTROCHEMICAL DETERMINATION OF Pb(II) and Cd(II) USING Ti-MOF MATERIAL

3.4.1. Electrochemical behaviour of Pb(II) and Cd(II) at Ti-MOF/ GCE under DPASV

The electrochemical response of 25.0 µg/L Pb(II) and Cd(II) in 0.1 M acetate buffer electrolyte using the bare GCE and Ti-MOF/ GCE under the DPASV is obtained and shown in Figure 3.19. Figure 3.19(a & b) reveals that the GCE showed no oxidative peak current of Pb(II) and Cd(II), which infers that the Pb(II) and Cd(II) show poor affinity towards the GCE hence, no significant oxidation occurs at the electrode surface. However, Ti-MOF/GCE shows a pronounced oxidative peak current of Pb(II) and Cd(II) at an applied potential of *Ca.* -0.5 V and *Ca.* -0.8 V, respectively. The high oxidative peak current using the Ti-MOF/GCE infers that the Pb(II) and Cd(II) have high affinity towards the Ti-MOF material hence, giving a fairly good electrochemical response at the electrode surface. The presence of amino and hydroxyl functional groups of the functionalized material chelating the heavy metals enables efficient oxidation at the electrode surface (Zheng et al., 2024). The high specific surface enables the Pb(II) and Cd(II) to occupy the pores, which undergo efficient oxidation at the electrode surface (Cheng et al., 2021). A high oxidative peak current of Pb(II) and Cd(II) using the Ti-MOF/GCE is due to the combined effect i.e., the high

surface area and conductivity of Ti-MOF, which facilitates the efficient charge transfer reactions at the electrode surface.

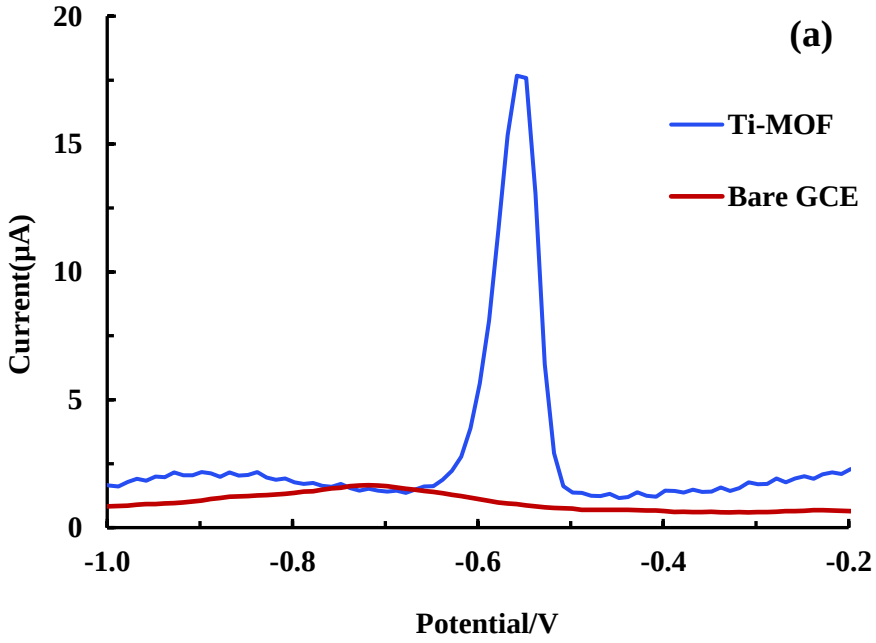

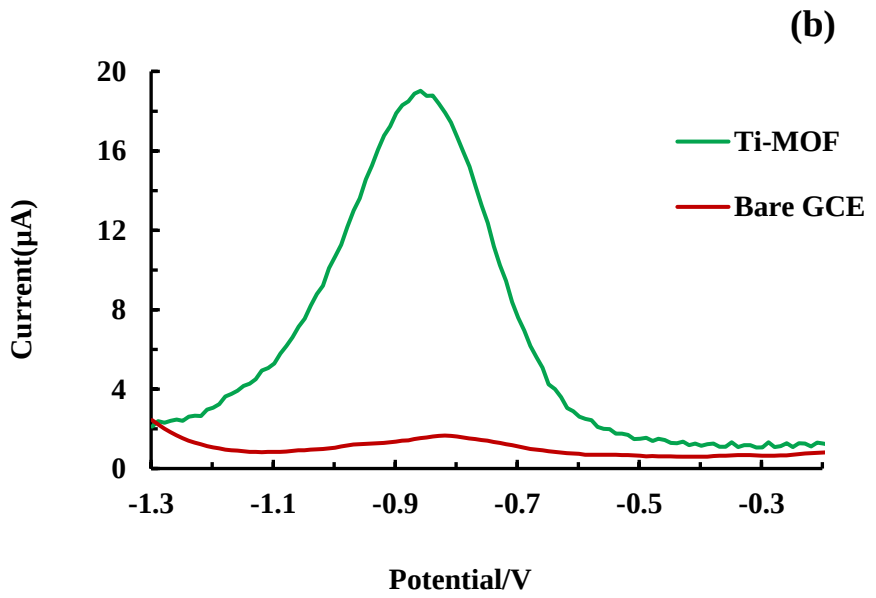

Figure 3.19: (a) DPASV curves obtained for Pb(II) (25.0 µg/L at pH 4.5; acetate buffer (0.1 M)) using the bare GCE and Ti-MOF/GCE; (b) DPASV curves obtained for Cd(II) (25.0 µg/L at pH 4.5; acetate buffer (0.1 M)) using the bare GCE and Ti-MOF/GCE.

3.4.2. Optimization of the stripping parameters

The pH dependence detection of Pb(II) and Cd(II) (each 25.0 µg/L) in acetate buffer (0.1 M) is studied using a Ti-MOF/GCE probe. The other parameters are deposition potential -1.2 V (*vs.* Ag/AgCl (3M)), deposition time 60 sec. The pH is varied from 3.5 to 5.5 and the corresponding oxidative peak current is recorded and results are shown in Figure 3.20(a). Figure 3.20(a) shows that an increase in pH from 3.5 to 4.5 caused an increase in the oxidative peak current from 20.4 to 24.2 µA (for Cd(II)) and from 12.2 to 16.7 µA (for Pb(II), respectively. However, further increases in pH from 4.5 to 5.5 caused for decrease in oxidative peak current from 20.4 to 18.8 µA for Cd(II) and from 16.7 to 14.4 µA for Pb(II), respectively. The pH_{PZC} of the Ti-MOF is 4.2, which indicates that the surface of the solid carries a net negative charge below pH 4.2 and carries net positive charges at pH>4.2. On the other hand, the speciation of the Cd(II) and Pb(II) is depicted in Figure 3.20 (b & c). At pH lower than 6.0, Cd(II) and Pb(II) predominantly exist in their ionic forms, specifically as Cd^{2+} and Pb^{2+}. Conversely, as pH increased from 6-8, Pb(II) tends to form hydroxo species ($Pb(OH)^{+}$ and $(Pb(OH)_2$ while cadmium is still in its ionic form at pH<8. At pH>8, the dominant species shift toward complex hydroxides due to the high concentration of OH^{-} and insoluble cadmium hydroxide precipitates, reducing dissolved cadmium concentrations. Therefore, the relatively high peak current observed at pH 4.5 is due to the enhanced sorption of positively charged species of metal ions by the negatively charged solid surface. However, pH>4.5 has caused for slight decrease in the peak current possibly due to the slight increase in the hydroxo species of Pb(II), which was relatively less sorbed on the surface. The hydroxo species do not exhibit attraction to the electrode surface, resulting in a diminished current response at elevated pH levels (Hu et al., 2024). In addition, the increase in hydroxyl species at higher pH values in

aqueous solutions diminishes the oxidation of Pb(II) and Cd(II) at the electrode surface. It was reported previously that a more pronounced peak current is observed at slightly acidic or lower pH levels, approximately 4.5, while higher pH conditions correspond to a decrease in peak current (Zhang et al., 2023). Therefore, pH 4.5 was selected for the electrochemical detection of Pb(II) and Cd(II) in an aqueous medium.

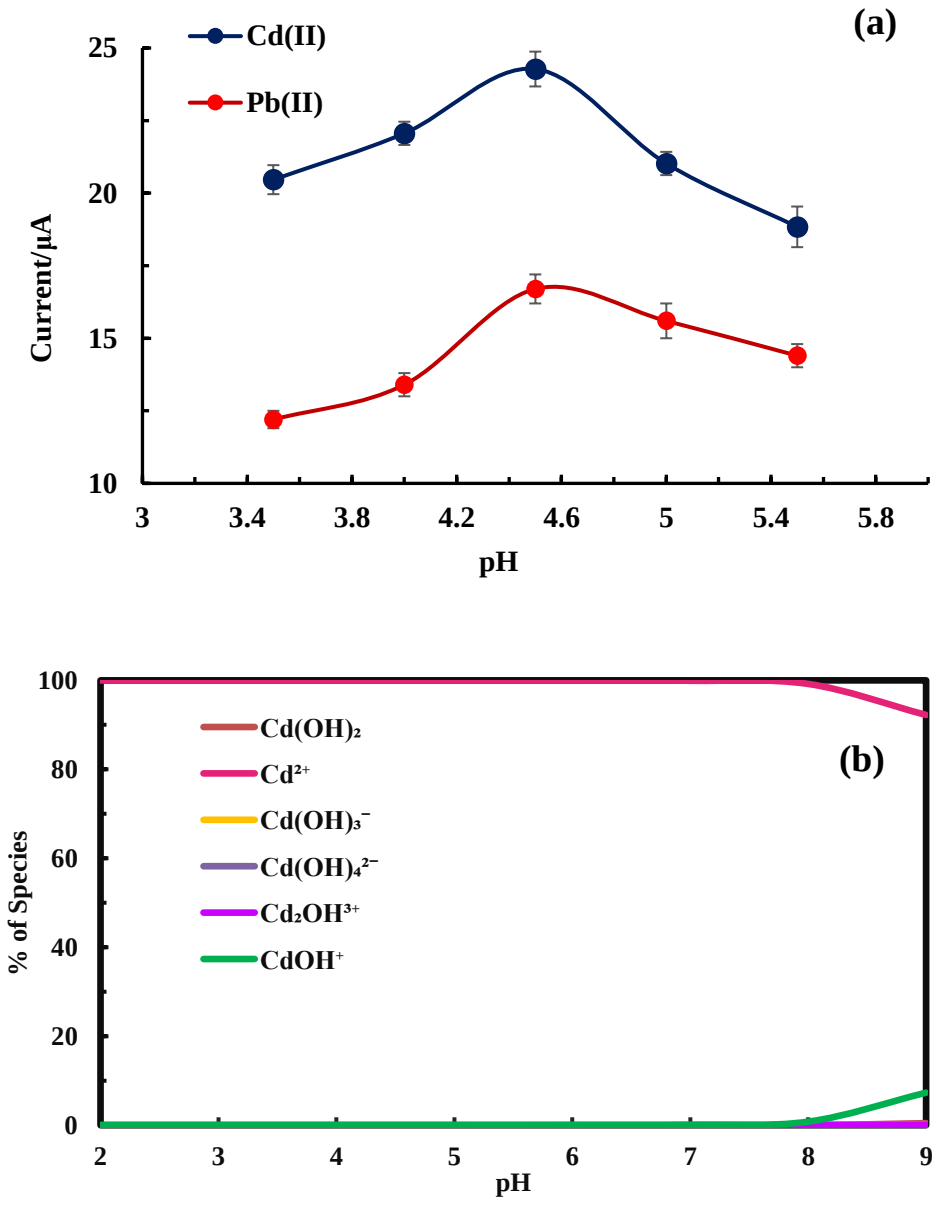

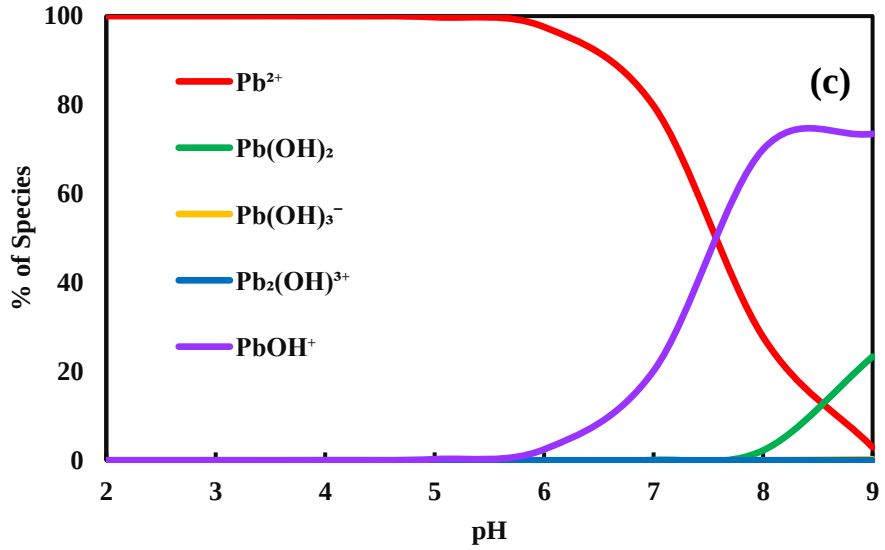

Figure 3.20: (a) Effect of pH in the electrochemical detection of Pb(II) and Cd(II) (each 25.0 µg/L) in the Pb(II) & Cd(II) in 0.1 M acetate buffer; (b) Speciation of Cd(II); (c) Speciation of Pb(II).

Deposition or the accumulation potential is a crucial parameter in the stripping voltammetry since it significantly affects the sensitivity of the working electrode. The deposition potential is varied from -1.4 V to -1.0 V and the corresponding peak current is presented in figure 3.21. The oxidation peak current is maximum at a deposition potential of -1.2 V for Pb(II) and -1.3 V for Cd(II). Therefore, the optimum deposition potential for Pb(II) and Cd(II) detection is 1.2 V and -1.3 V, respectively using the Ti-MOF/GCE fabricated electrode.

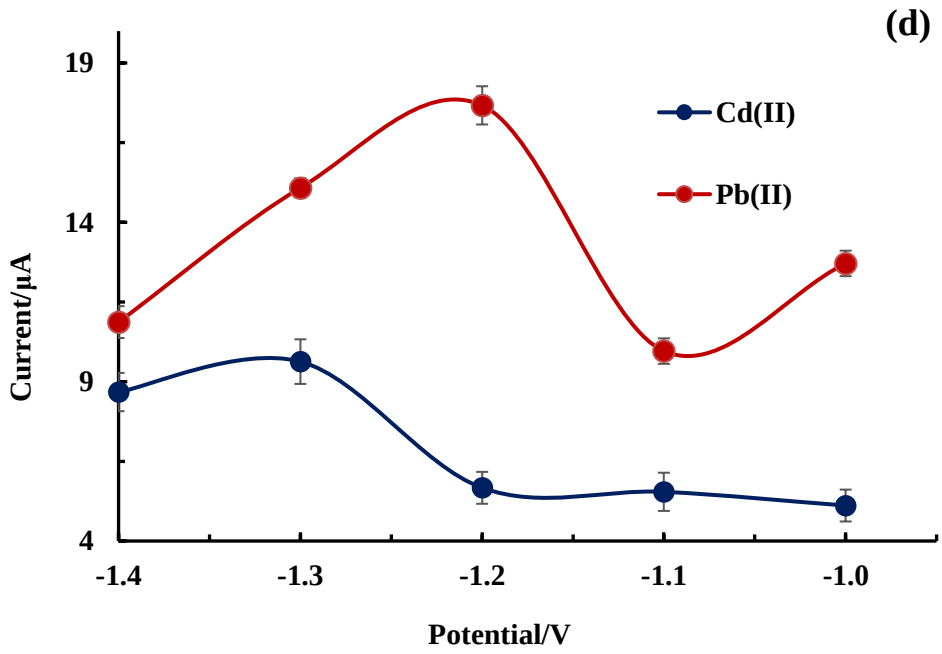

Figure 3.21: The dependence of oxidative peak current for Pb(II) and Cd(II) (each 25.0 µg/L in 0.1 M acetate buffer; pH 4.5) as a function of deposition potential.

The deposition time at various time intervals ranging from 30 sec to 160 sec is conducted and the oxidative peak current for Pb(II) and Cd(II) (25.0 µg/L) is shown in Figure 3.22. An increase in the deposition time from 30 sec to 90 sec has caused a gradual increase in peak current for Pb(II) and Cd(II). However, a further increase in deposition time from 90 to 160 sec caused a significant decrease in the oxidative peak current, which is due to the saturation of electroactive sites at the electrode surface (*Cf* Figure 3.22). Therefore, 60 and 90 sec are used as deposition time for efficient and trace detection of Pb(II) and Cd(II) in aqueous medium.

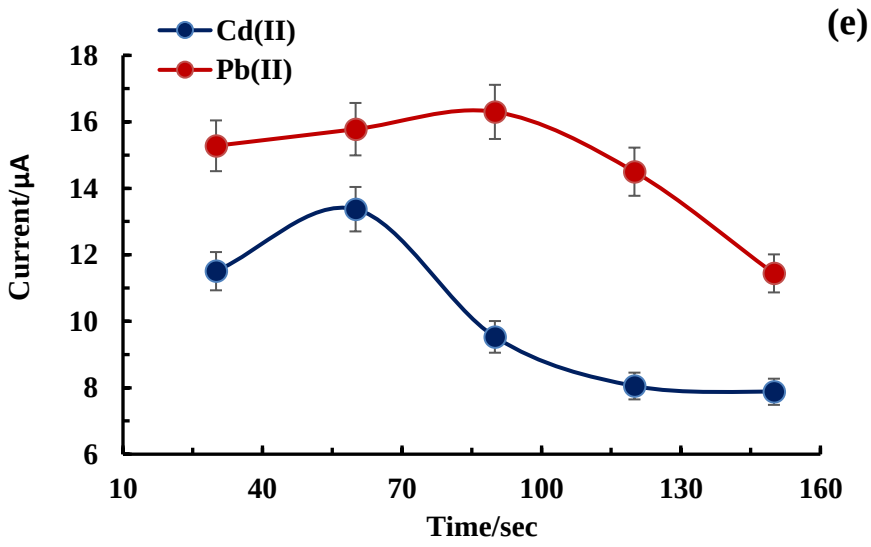

Figure 3.22: Parametric studies carried out at 25.0 µg/L Pb(II) & Cd(II) (0.1 M acetate buffer; pH 4.5); The oxidative peak current of Pb(II) & Cd(II) as a function of time.

3.4.3. Electrochemical determination of Pb(II)

The DPAS voltammograms of Pb(II) under optimized stripping conditions are recorded using the Ti-MOF/GCE probe. Figure 3.23 shows the voltammograms of Pb(II) at varied concentrations of Pb(II). It is evident from the figure that increasing the Pb(II) concentration from 5.0 to 25.0 µg/L caused a gradual increase in the oxidative peak current. Moreover, the oxidative peak current occurs at a potential of -0.5 V. Further, a linear relationship is obtained between the concentration of Pb(II) against the oxidative peak current values. Therefore, the calibration linear line is represented with a linear equation: y (µA) =0.4372 x (µg/L) + 6.438 (R^2= 0.9995) (*Cf* Figure 3.23 (Inset)). Further, the LOD and LOQ are obtained and found to be 0.09 µg/L and 0.32 µg/L, respectively, for Pb(II) using the Ti-MOF/GCE. The LOD value is considerably less than the 10.0 µg/L in drinking water, the permissible level suggested by the WHO. Similarly a low-cost copper (Cu)-based MOF detects the Pb(II) using the electrochemical sensor with LOD of 4.40 µg/L (Kang et al., 2017).

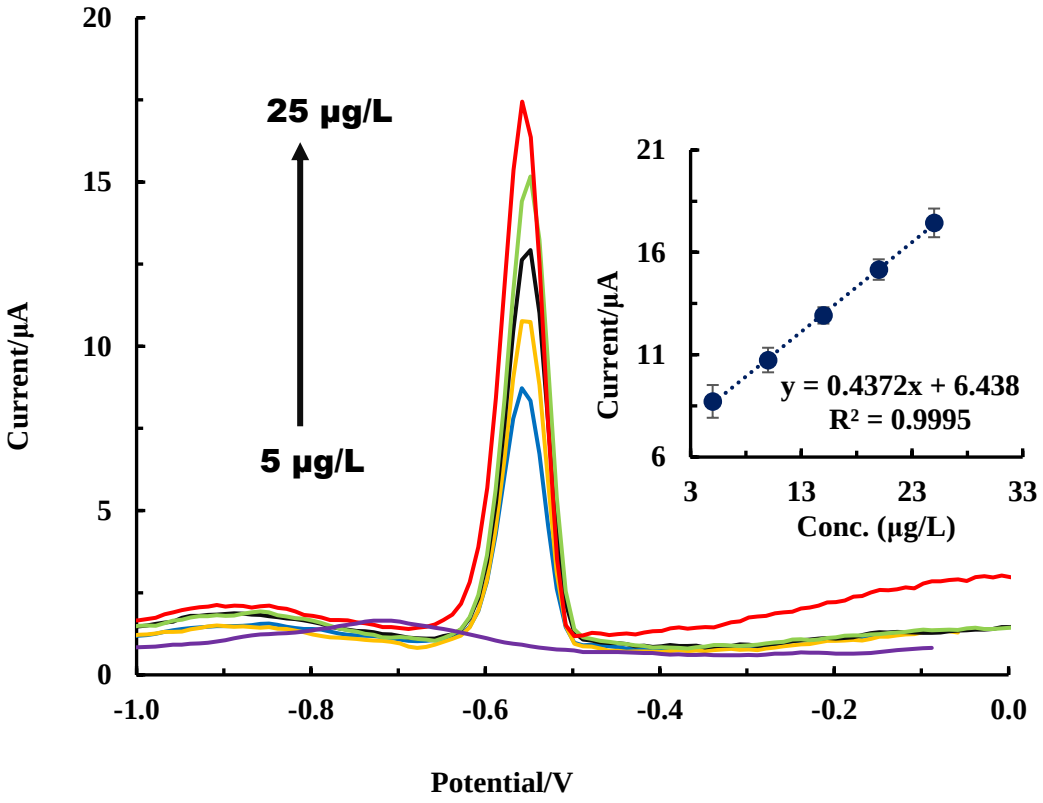

Figure 3.23: The DPASV of Pb(II) as a function of Pb(II) concentrations; [Inset: Calibration line obtained for the oxidative peak current of Pb(II) as a function of Pb(II) concentration].

3.4.4. Electrochemical detection of Cd(II)

The detection of Cd(II) as a function of Cd(II) concentrations is obtained under optimized stripping conditions and utilizing the Ti-MOF/GCE probe. Figure 3.24 shows the Cd(II) voltammograms at varied Cd(II) concentrations and evident that increasing the Cd(II) concentration from 5.0 to 25.0 µg/L caused an increase in the oxidative peak current. The Cd(II) peak current is observed at *Ca*. The potential of -0.9 V. A calibration line is obtained between the concentration of Cd(II) against the oxidative peak current values and found a good linear relationship. The calibration line is represented as: *y* (µA) =0.412 x (µg/L) + 15.166 with R^2= 0.996 (*Cf* Figure 3.24 (Inset)). The LOD and LOQ are found to be 0.09 µg/L and 0.56 µg/L for Cd(II) using

the Ti-MOF/GCE probe. The LOD value is considerably less than the 3.0 µg/L in drinking water, the permissible level suggested by the WHO. The hybrid material precursors to the hexadecyltrimethylammonium bromide (HDTMA) and bentonite incorporated carbon paste electrode showed high affinity towards the Cd(II) and the probe detects the Cd(II) with the limit of detection of 1.36 µg/L. Moreover, the probe detects satisfactorily the Cd(II) with a high recovery rate in the tap water samples (Lee et al., 2016).

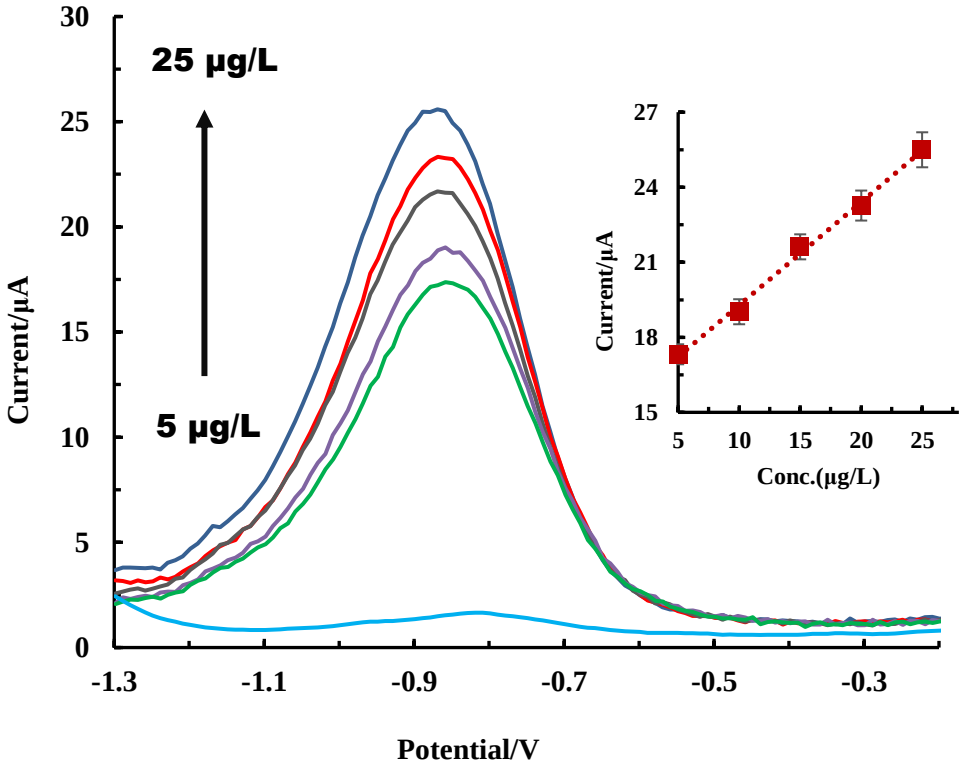

Figure 3.24: The DPASV of Cd(II) as a function of Cd(II) concentrations; Inset: Calibration line obtained for the oxidative peak current of Cd(II) as a function of Cd(II) concentration.

3.4.5. Simultaneous detection of Pb(II) and Cd(II)

The advantage of using the electrochemical method is the possible simultaneous detection of multiple heavy metal toxic ions. The studies are extended

for the detection of Pb(II) and Cd(II) simultaneously. The DPASV voltammograms of Pb(II) and Cd(II) under optimized stripping conditions are recorded using the Ti-MOF/GCE and the results are shown in Figure 3.25. Figure 3.25 shows distinct oxidative peaks are recorded for Pb(II) and Cd(II) at an applied potential of -0.8 V and -0.6 V, respectively. Further, it is evident from the figure that increasing the Pb(II) and Cd(II) concentration from 5.0 to 25.0 µg/L has caused for increase in the oxidative peak currents. These results enabled us to draw the calibration lines separately for the Pb(II) and Cd(II) since a fairly good linear relationship is obtained between the concentration of Pb(II) and Cd(II) against the oxidative peak currents. The calibration lines are represented with the linear equations: y(µA) =0.0636x (µg/L) + 3.496 (R^2= 0.9998) and y(µA) =0.0282x (µg/L) + 3.186 (R^2= 0.9966), respectively, for Pb(II) and Cd(II) (*Cf* Figure 3.25 (Inset)). These linear equations enabled to obtain the LOD and LOQ values for the simultaneous detection of Pb(II) and Cd(II) using the Ti-MOF/GCE probe. The LOD is found to be 1.02 µg/L and 0.59 µg/L for Pb(II) and Cd(II), respectively. Similarly, the LOQ values are 3.42 µg/L and 1.98 µg/L, respectively, for the Pb(II) and Cd(II). These results suggest that microelectrode is promising in detecting simultaneously the Pb(II) and Cd(II) at trace levels and perhaps useful in devising the miniature device.

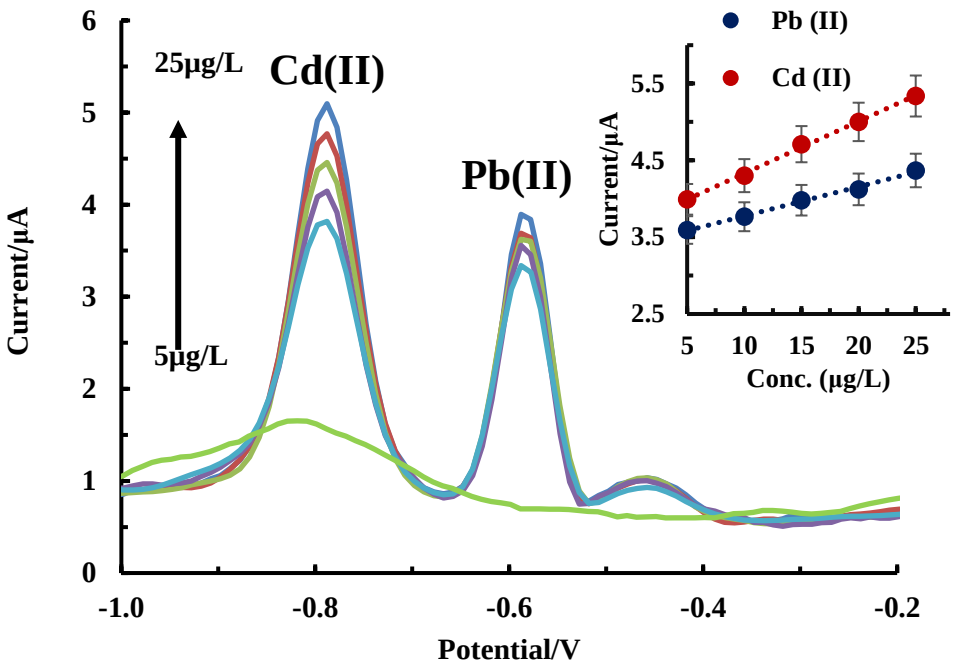

Figure 3.25: The simultaneous detection of Pb(II) and Cd(II) at varied concentrations of Pb(II) and Cd(II) concentrations; [Inset: Calibration lines obtained for the oxidative peak currents of Pb(II) and Cd(II) vs Pb(II) and Cd(II) concentrations].

Further, table 3.7 comprises the use of various materials in the simultaneous detection of Cd(II) and Pb(II) under the electrochemical methods, and the LOD values are compared with our present work. Indeed the probe utilized in the present study showed a significantly lower detection limit compared to several other studies utilizing different materials. These results infer that the Ti-MOF has greater potential in detecting these two ions at trace levels.

Table 3.7: Analytical performance comparison of Cd(II) and Pb(II) ion stripping.

Material	**Method**	**Linear range (µg/L)**		**LOD (µg/L)**		**Reference**
		Pb(II)	**Cd(II)**	**Pb(II)**	**Cd(II)**	

GCE/CN-polymer	DPASV	0.2 - 50	1.2 - 90	2.27	0.8	(Philips et al., 2012)
SWCNTs-CO-Biomass	DPASV	0 – 1.0	0 – 1.2	0.1	1.0	(Dali et al., 2018)
HGNPs/SPEd	SWASV	5 – 100	-	3.0	3.2	(Aragay et al., 2011)
Poly(ANI-co-DDS)	SWASV	2.0 – 20	-	0.4	0.5	(Vedhi et al., 2009)
PANI/GC	SWASV	0 - 0.06	0 – 0.05	33	33	(Wang et al., 2011)
Pt/MWCNT/P1,5-DAN	SWASV	4 – 150	-	2.1	3.2	(Vu et al., 2015)
PDPA/GC–ME	DPASV	0.3 – 15.0	2.5 – 230	2.8	1.2	(Mikuła et al., 2009)
Ti-MOF	**DPASV**	**5 - 25**	**-**	**1.02**	**0.59**	**This work**

3.4.6. Effect of co-existing ions in Pb (II) and Cd (II) detection

The reliability of the Ti-MOF/GCE probe in the detection of Pb(II) and Cd(II) is evaluated in the presence of several cations and anions. The interfering co-ions chosen are Cl^-, NO_3^-, F^-, Mg^{2+}, and Ca^{2+}. The concentration of co-existing ions is 10-fold (250.0 µg/L) than the analyte (Pb(II) and Cd(II)) concentrations, i.e., 25.0 µg/L

each. Figure 3.26 shows the oxidative peak currents of Pb(II) and Cd(II) in the presence of these cations/anions. It is interesting to observe that these ions show no effect in the detection of Pb(II) and Cd(II). Therefore, the Ti-MOF/GCE showed fairly good selectivity for the low-level detection of Pb(II) and Cd(II). Therefore, the results indicated that the selectivity of the material is good, at least for the detection of Pb(II) and Cd(II) in aqueous media. Glassy carbon electrodes (GCEs) are modified with the metal-organic framework ZIF-8, along with a bismuth complex and carboxylated multi-walled carbon nanotubes, to investigate the influence of several ions in the detection of Pb(II) and Cd(II). The introduction of 5 mg/L of Na^{+}, Mg^{2+}, Cu^{2+}, Ca^{2+}, Cl^{-}, and SO_4^{2-} did not affect significantly the detection of these ions suggesting that the selectivity of this electrode is quite favorable (Hu et al., 2024).

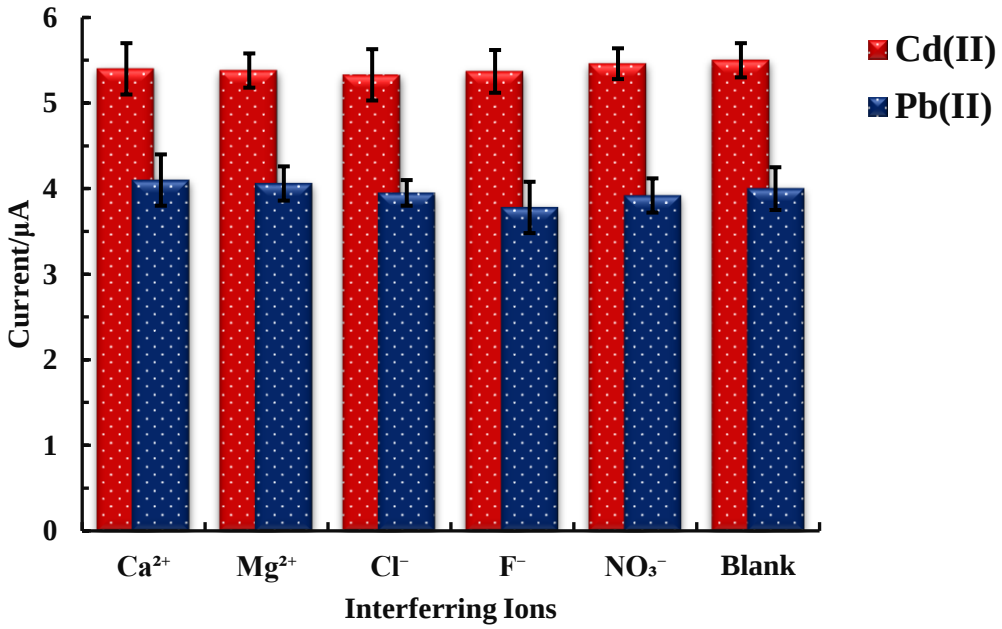

Figure 3.26: The detection of Pb(II) and Cd(II) in the presence of several co-existing ions using the Ti-MOF/GCE probe ([Pb(II) and Cd(II)]: 25.0 μg/L; [Interfering ion]: 250.0 μg/L.

3.4.7. Simultaneous detection of Pb(II) and Cd(II) in the natural water samples

The Ti-MOF working electrode was employed for the simultaneous detection of Pb(II) and Cd(II) in the river water samples. The water was collected from the Tlawng River (Sairang village; Mizoram, India; latitude N23.814238 and longitude E92.651924). The water samples are filtered using filter paper (11μm) to remove the suspended particles and subjected to various physicochemical parametric studies. Table 3.8 shows the analyzed results using several analytical tools. It is evident from Table 3.8 that the river water contained relatively higher concentrations of NO_3^- with higher alkalinity. Similarly, the water contains high concentrations of Ca and Mg i.e., 163, and 58 mg/L, respectively. Similarly, the NPOC and IC values are 34.66 and 29.80, respectively. The higher values of IC with Ca and Mg indicated the presence of calcium and magnesium carbonates and bicarbonates in the water samples.

Table 3.8: Analysis of real water samples using different analytical methods.

Parameters Studied	**Analytical Results**
pH	7.07
Conductivity	133 μS/cm
Resistivity	0.0076 μOhm.cm
Salinity	0.55 PSU
Ox. Red. Potential	281 mV
Alkalinity	147 mg/L
Al	0.06 mg/L
NO_3^-	33.6 mg/L
SO_4^{2-}	15.6 mg/L

PO_4^{3-}	1.44 mg/L
F	ND
AAS analysis	
Mg	58 mg/L
Ca	163 mg/L
Ni	0.088 mg/L
TOC Analysis (mg/L)	
Inorganic Carbon (IC)	29.80
Non-purgeable organic carbon (NPOC)	34.66

Note: ND-Not detected

The acetate buffer (pH 4.5) is prepared using the river water and further spiked with various concentrations (5.0 to 25.0 µg/L) of Pb(II) and Cd(II). Furthermore, under the optimized conditions differential pulse voltammograms are obtained for these solutions using the Ti-MOF/GCE probe. Figure 3.27 shows the voltammograms of Cd(II) and Pb(II), which demonstrates the distinct Pb(II) and Cd(II) oxidative peaks at the potential of *Ca.* -0.79 and -0.58 V, respectively. The increase in Pb(II) and Cd(II) bulk concentrations from 5.0 to 25.0 µg/L caused the increase in the oxidative peak currents from 3.95 to 5.19 µA for Cd(II) and from 3.45 to 4.10 µA for Pb(II), respectively. Further, figure 3.27(Inset) shows reasonably a good linear relationship is obtained between the pollutant concentrations and the corresponding oxidative peak currents using the Tlawng River and utilizing the Ti-MOF/GCE probe. The calibration lines are represented with the linear equations: y(µA) =0.058x (µg/L) + 3.6367 (R^2= 0.8972) for Cd(II) with the LOD 0.69 µg/L and LOQ 2.31 µg/L. Similarly, linear

equation obtained is *y*(µA) =0.033x (µg/L) + 3.375 (R^2= 0.784) for Pb(II) with the LOD of 1.22 µg/L and LOQ of 4.07 µg/L. These results infer that the Ti-MOF/GCE is useful in detecting the Pb(II) and Cd(II) even in the natural water samples, which indicates the selectivity of the probe for the low-level detection of these two pollutants.

Additionally, the percentage of Pb(II) and Cd(II) recovery is computed in the spiked river water sample, and results are returned in Table 3.9. Table 3.9 demonstrates that the Ti-MOF/GCE detects the Pb(II) and Cd(II) efficiently with relatively very high recovery rates. The recovery percentages ranged from 90% to 114% and 102% to 112%, respectively for Cd(II) and Pb(II), in river water samples. A comparable investigation was conducted earlier utilizing the nanocomposite material (silane grafted and Ag(NP) decorated bentonite (Ag(N)@Bt/TC)) in the detection of Pb(II) and Cd(II) in spring water sample and the recovery rate was found to be 93% to 108% and 99% to 113%, respectively, for the Cd(II) and Pb(II) (Lalmalsawmi et al., 2022).

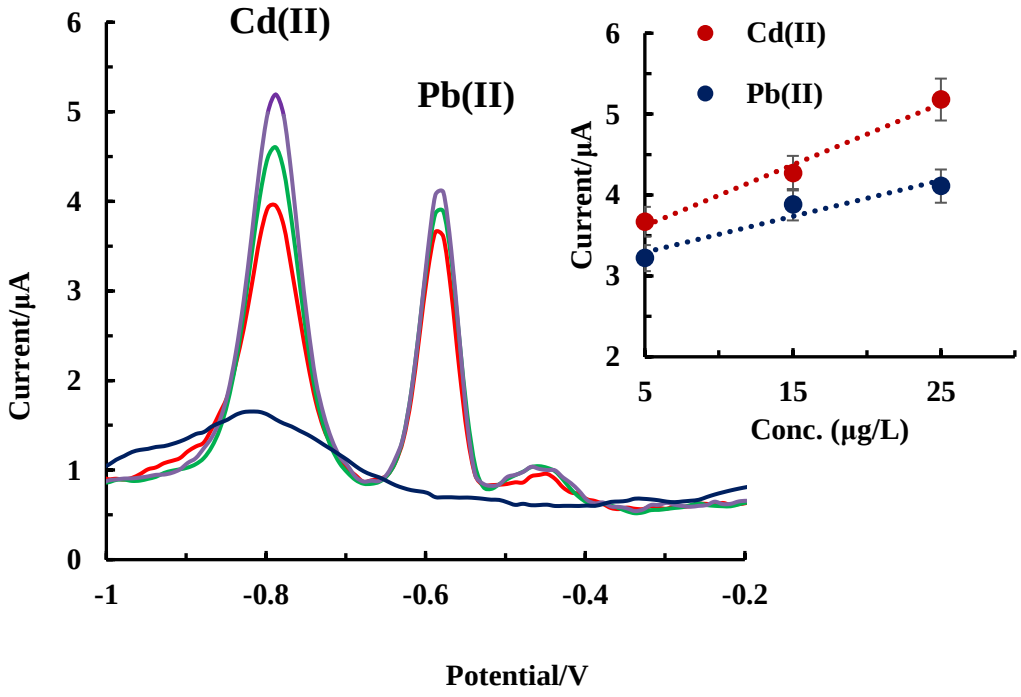

Figure 3.27: Real water sample spiked with Pb(II) and Cd(II) concentrations from 5.0 to 25.0 µg/L; Inset: Calibration line obtained for the oxidative peak current of Pb(II) and Cd(II) using the Tlawng river water.

Table 3.9: The recovery of Pb(II) and Cd(II) in the spiked spring water and groundwater using Ti-MOF/GCE.

Spiked amount(ppb)	Found(ppb)		Recovery (%)	
	Cd(II)	Pb(II)	Cd(II)	Pb(II)
5	5.68	5.53	113.69	110.64
15	13.63	16.33	90.87	108.88
25	25.68	25.53	102.73	102.128

3.4.8. Conclusion

The DPAS voltammograms show intense oxidative peaks for the Pb(II) and Cd(II) at an applied potential of -0.54 V and -0.85 V, respectively, using the Ti-MOF/GCE. However, the GCE shows no significant oxidative peak of Pb(II) and Cd(II) in the DPASV measurements. The detection of Pb(II) under the DPASV is optimized at pH, deposition potential, and deposition time of 4.5, -1.2 V, and 60 sec, respectively. Similarly, the pH, deposition potential, and deposition time are optimized to 4.5, -1.3 V, and 90 sec for Cd(II). The Pb(II) and Cd(II) were detected using the Ti-MOF both individually and simultaneously at a wide range of analyte concentrations varied from 5.0 µg/L to 25.0 µg/L for Pb(II) and Cd(II). Good linear calibration lines are obtained for the simultaneous detection of Pb(II) and Cd(II) correlation between concentration and peak current. The calibration lines are

represented with the linear equations: $y(\mu A) = 0.0636x\ (\mu g/L) + 3.496$ ($R^2 = 0.9998$) and $y(\mu A) = 0.0282x\ (\mu g/L) + 3.186$ ($R^2 = 0.9966$), respectively, for Pb(II) and Cd(II). Moreover, the LOD is found to be 1.02 µg/L and 0.59 µg/L for Pb(II) and Cd(II), respectively. The Ti-MOF/GCE demonstrates high sensitivity and selectivity for simultaneous detection of Pb(II) and Cd(II), even in the presence of high concentrations of co-existing ions *viz.*, Cl^-, NO_3^-, F, Mg^{2+}, and Ca^{2+}. The Ti-MOF/GCE demonstrated significant efficacy in the simultaneous detection of Pb(II) and Cd(II) in the river water samples. The recovery percentages ranged from 90% to 114% and 102% to 112%, respectively for Cd(II) and Pb(II), in river water samples. Therefore, the fabricated Ti-MOF/GCE probe showed potential in developing the miniaturized device for the selective and sensitive detection of Pb(II) and Cd(II) simultaneously in aqueous medium.

3.5. ELECTROCHEMICAL DETERMINATION OF CIPROFLOXACIN (CFX) AND CARBAMAZEPINE (CBZ)

3.5.1. Electrochemical behavior of CFX and CBZ at Zr-MOF/ GCE under DPASV

The electrochemical response of 50.0 µg/L CFX and CBZ in 0.1 M (pH=7) phosphate buffer is obtained using the bare GCE and Zr-MOF/GCE under the DPASV. Figure 3.28(a & b) shows the DPAS voltammograms of the CFX and CBZ. It is evident from Figure 3.28(a & b) that the bare GCE showed no oxidation peak current of CFX and CBZ, which implies that the CFX and CBZ are poorly sorbed at the electrode surface and insignificantly oxidized at the GCE. However, on the other hand, a pronounced oxidative peak current of CFX and CBZ is obtained at potential *Ca.* 0.25 V and 1.13 V, respectively, using the Zr-MOF/GCE probe. The high oxidative peak current using the Zr-MOF/GCE infers that the CFX and CBZ show fairly high affinity towards the Zr-MOF material, and undergoes readily the oxidation of these pollutants. Therefore, the oxidation of these compounds gives an enhanced oxidative peak current. The Zr-MOF has higher hydrophobic behavior with an enhanced organophilic

nature enabling it to attract the CFX and CBZ molecules (Hu et al., 2018). Moreover, the high surface area with the micro-porous structure of Zr-MOF sorbs these molecules efficiently and facilitates in electrode oxidation of these compounds at the Zr-MOF surface (Ebrahim et al., 2024). More quantitatively, the CFX and CBZ show the oxidative peak currents of 11.73 and 13.28 μA, respectively using the Zr-MOF probe. Moreover, the Zr-MOF causes *Ca.* 8 and 2-fold increase in the oxidative peak currents, respectively, for the CFX and CBZ, compared to the bare GCE. The electrochemical oxidation of ciprofloxacin showed two electron transfers as shown in scheme 3.1 (Tajik et al., 2021). It was reported previously that the CBZ oxidizes irreversibly at the electrode surface and proposed that the oxidation of nitrogen atoms in the central ring forms cation radicals (*Cf* Scheme 3.2). Further, the CBZ oxidation is a complex reaction and the loss of electrons in two steps occurs simultaneously (Daneshvar, 2022). The porous-Nafion/BDD electrode demonstrated an approximate 2-fold increase in the oxidative peak current for ciprofloxacin, reaching to 11 μA, compared to the bare/BDD electrode (Gayen et al., 2016).

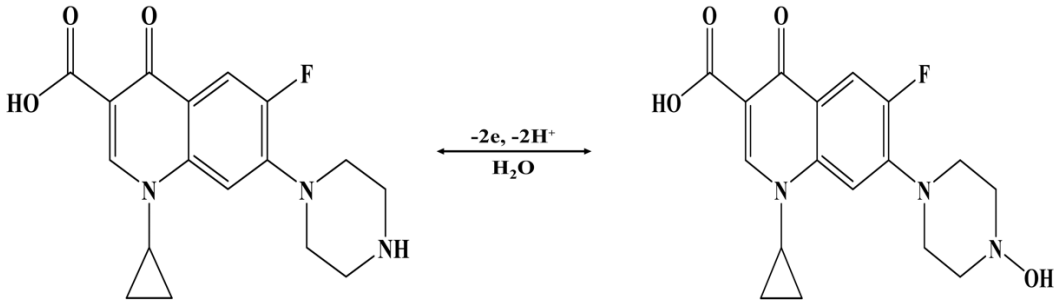

Scheme 3.1: Electrochemical oxidation step of ciprofloxacin.

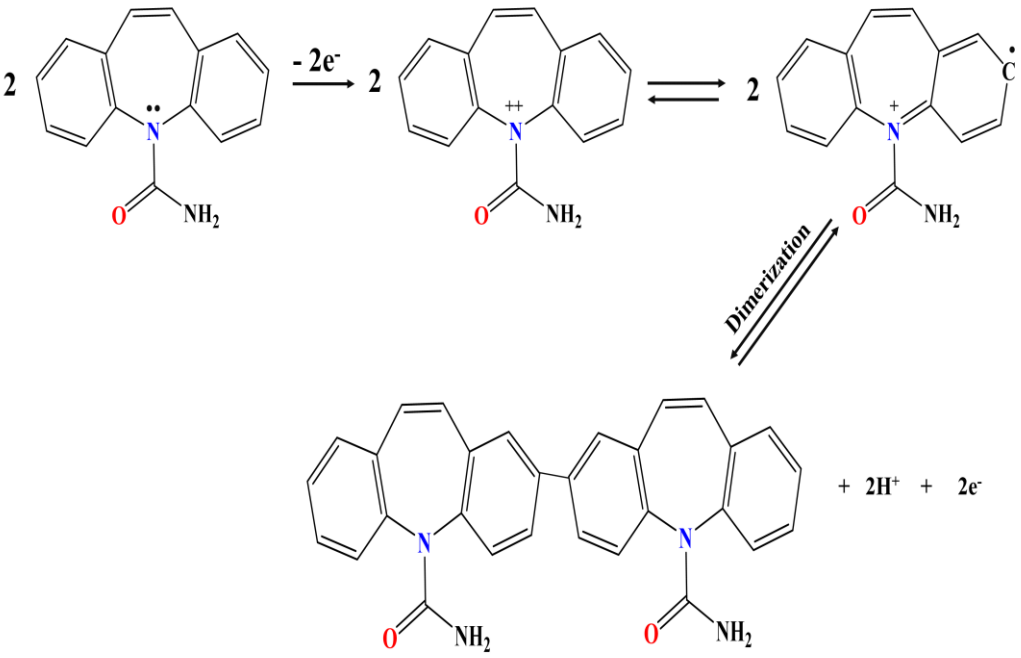

Scheme 3.2: Electrochemical oxidation steps of carbamazepine.

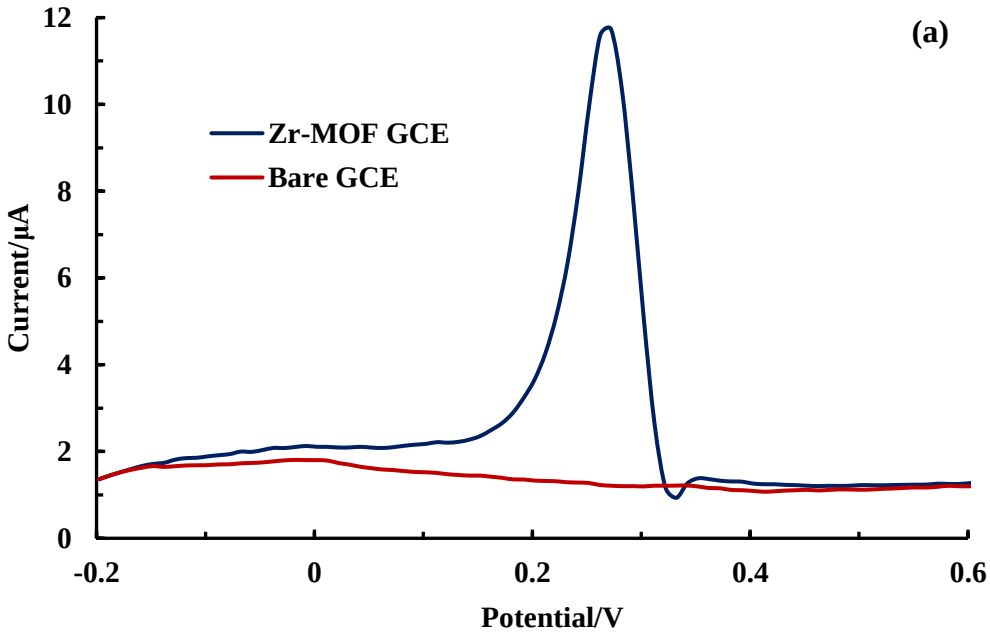

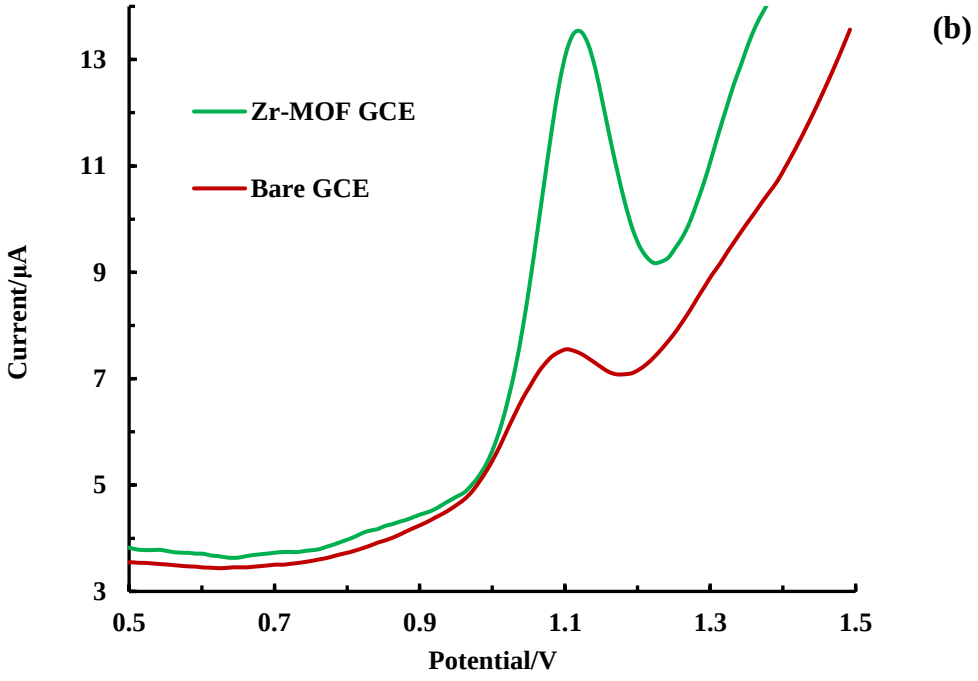

Figure 3.28: (a) DPASV curves for (a) CFX; and (b) CBZ ([CFX/CBZ]: 50.0 µg/L at pH 7.0; phosphate buffer (0.1 M)) using the bare GCE and Zr-MOF/GCE.

3.5.2. Optimization of the experimental parameters

The parametric studies, i.e., the effect of pH, deposition potential, and deposition time optimize the oxidation of CFX and CBZ using the Zr-MOF probe in an aqueous solution.

Figure 3.29(a) depicts the oxidative peak current of CFX and CBZ (50.0 µg/L each in phosphate buffer (0.1 M)) against the solution pH using a Zr-MOF/GCE probe. The other parameters were taken as deposition potential -0.2 V (*vs.* Ag/AgCl), deposition time 150.0 sec. Figure 3.29 (a) shows that an increase in pH from 5.0 to 7.0 caused an increase in the oxidative peak current. However, a further increase in pH caused for gradual decrease in the oxidative peak current for CFX and CBZ.

Further, the speciation studies of CFX is conducted using the pka values of 6.05 and 8.37 (Tan et al., 2015), and the results is given in Figure 3.29 (b). The speciation studies reveal that the CFX molecule exists to the CFX^{+} molecule within

the pH region 2.0-6.0 and dominates the zwitterionic state ($CFX^{\pm}$) within the pH region 6.0-8.5. However, further increase in pH (pH>8.5) the CFX molecule dissociates and forms the negatively charged species of $CFX^{-\cdot}$ On the other hand, the Zr-MOF shows a pH_{PZC} of 5.8. Therefore, the surface carries a net positive charge at pH<5.8 and a net negative charge at pH>5.8. Therefore, a relatively high peak current at pH (~7.0) is explicable with the fact that the zwitterionic form of CFX preferably sorbs at the electrode surface by the organophilic attraction between the CFX and solid surface forming the π-π bonding. Previously, it was reported that the zwitterionic form of CFX sorbs relatively at a higher extent by biochar within the pH region of 5.8 to 8.6 (Shi et al., 2023).

The lower peak current within the pH region 2.0-7.0 is due to the strong electrostatic repulsion between the positively charged CFX molecule and Zr-MOF solid, which restricted the sorption of the CFX molecule at the surface of the solid. Similarly, pH>7.0, the CFX molecule dissociates the carboxyl group ($-COO^-$) forming negatively charged species and the solid surface carries the negative charges, hence; repels each other resulting in low peak current (Xu et al., 2019). Therefore, pH 7.0 was selected for the electrochemical detection of CFX in an aqueous medium.

Similar to the CFX, the CBZ shows a gradual increase in oxidative peak current by increasing the pH from 5.0 to 70. However, a further increase in pH from 7.0 to 9.0 caused for gradual decrease in peak currents. Therefore, a relatively higher peak current is recorded at pH 7.0. Figure 3.29 (c) shows the speciation of CBZ as a function of pH. The CBZ predominates the neutral species within the pH region 2.3 to 13.9. However, pH 5.8. Therefore, the hydrophobic interaction dominates the adsorption of CBZ onto the surface around neutral pH, which caused for relatively higher peak current (Viegas et al., 2024; Yu et al., 2022).

The deposition potential was varied from -0.5 V to -0.1 V (for CFX) and -1.3 to -0.9 V (for CBZ) and the corresponding peak current is presented in Figure 3.29 (d). The oxidative peak current achieves its maxima at a deposition potential of -0.2 V for CFX and -1.1 V (for CBZ). The generation of hydrogen gas at lower deposition potential caused a decrease in peak current (García-García et al., 2009). These results

suggested that the optimum deposition potentials are -0.2 V and -1.1 V for the CFX and CBZ, respectively.

The deposition time at various time intervals ranging from 60 to 240 sec (for CFX) and 30 to 210 sec (for CBZ) is conducted and the oxidative peak current is presented in Figure 3.29 (e). Figure 3.29(e) shows an increase in the deposition time favored by the peak currents for CFX and CBZ. Further, the deposition time of 150 sec and 120 sec gives relatively higher peak currents for the CFX and CBZ, respectively. Therefore, the 150.0 sec. for CFX and 120.0 sec. for CBZ is used as the deposition time for efficient and trace detection of CFX and CBZ in aqueous medium.

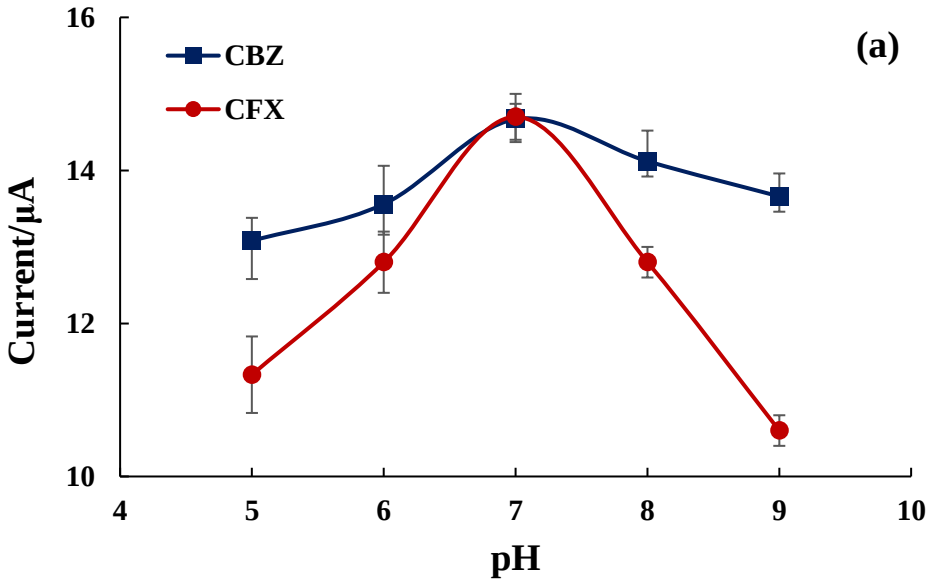

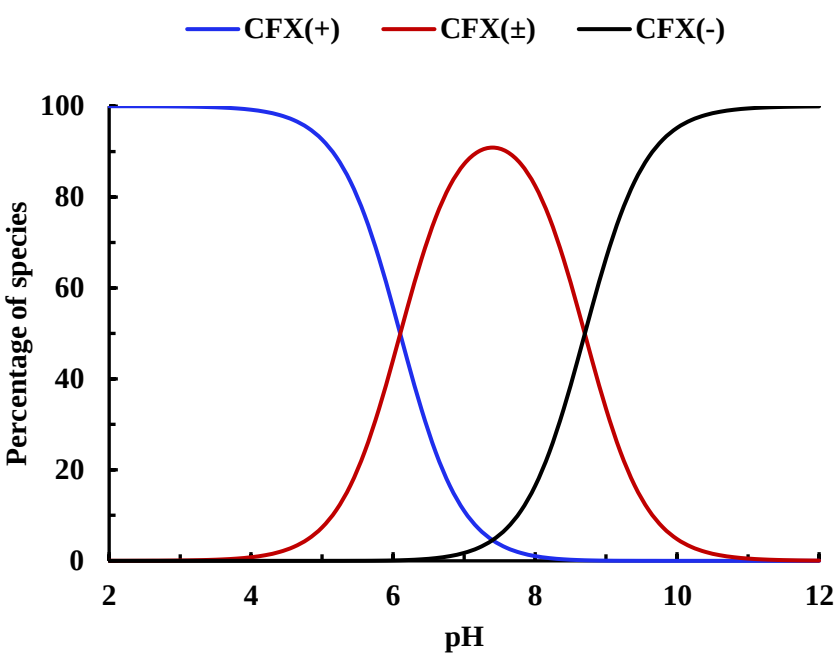
(b)
CFX(+)
CFX(±)
CFX(-)
Percentage of species
100
80
60
40
20
0
2
4
6
8
10
12
pH

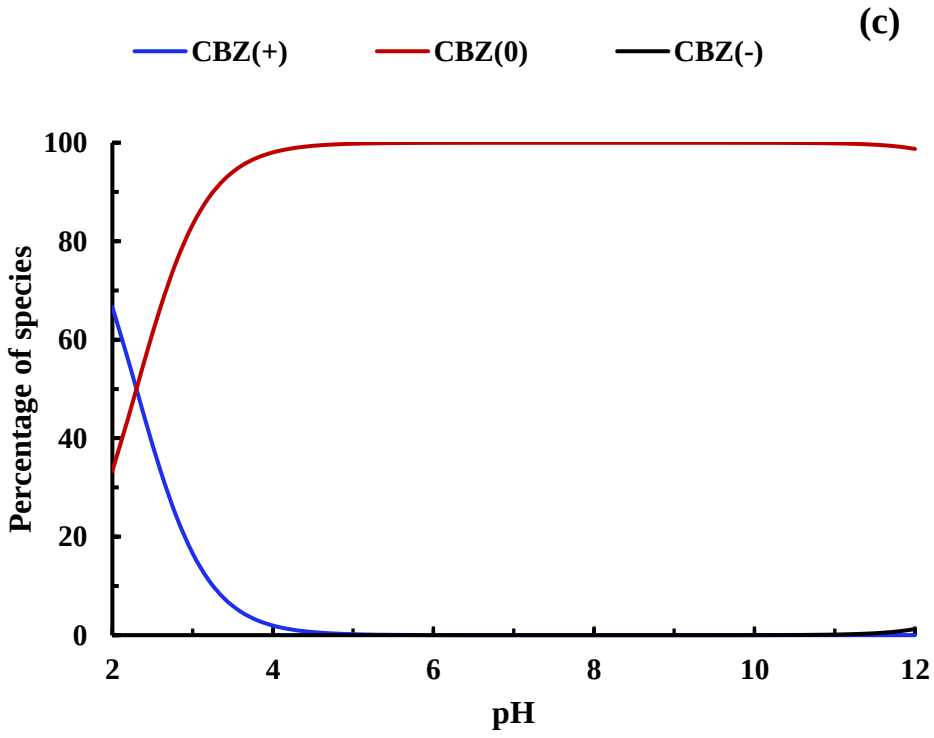
(c)
CBZ(+)
CBZ(0)
CBZ(-)
Percentage of species
100
80
60
40
20
0
2
4
6
8
10
12
pH

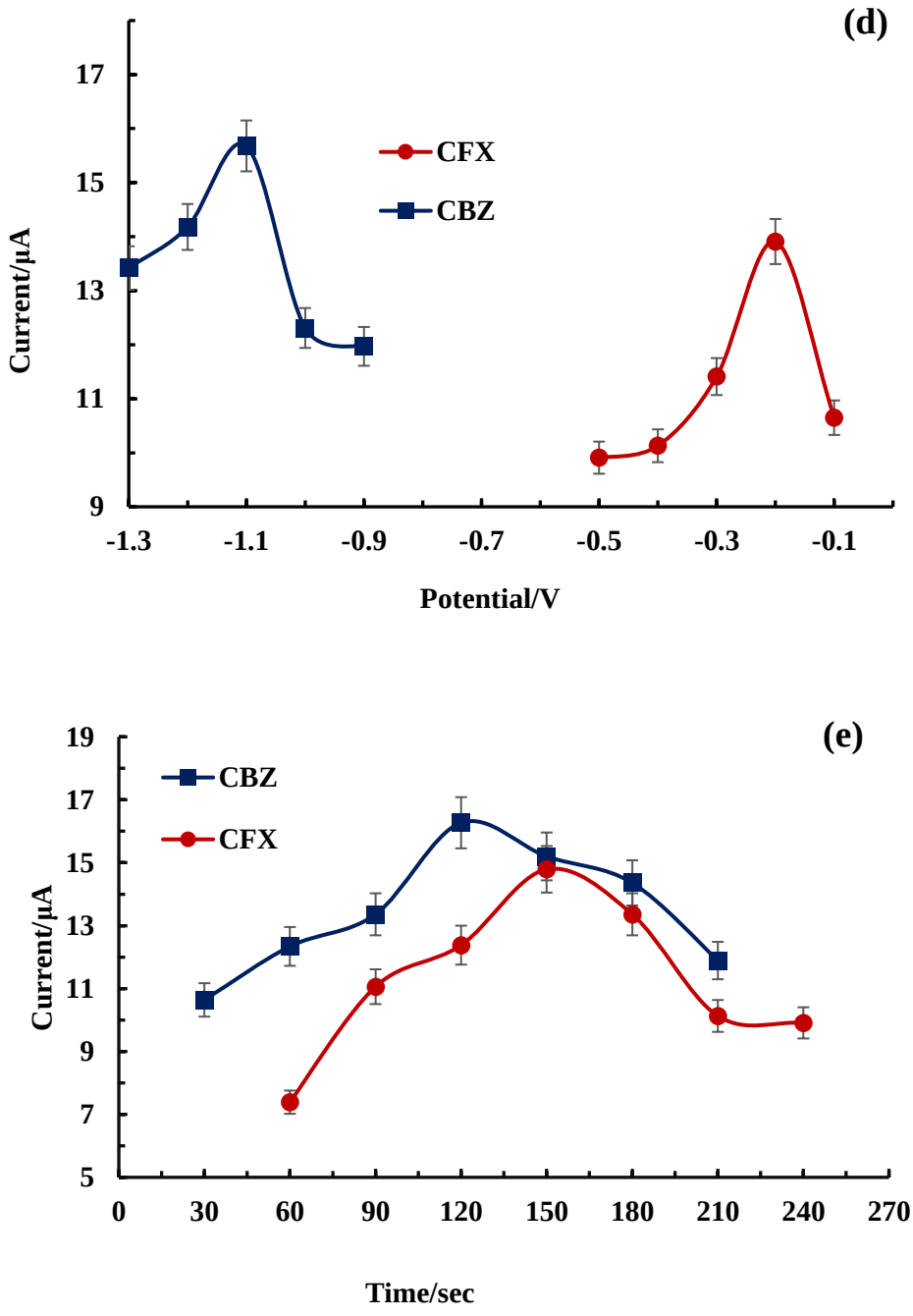

Figure 3.29: Parametric studies carried out for the detection of CFX and CBZ (50.0 µg/L) (a) the pH values; (b) Speciation of CFX; (c) Speciation of CBZ; (d) deposition potential; and (e) deposition time.

3.5.3. Concentration dependence studies

Low-level determination of CFX and CBZ are studied under the optimized experimental conditions, utilizing Zr-MOF/GCE with a concentration of CFX and CBZ ranging from 10.0 to 250.0 µg/L. Figure 3.30(a&b) shows the DPAS voltammograms against the concentration of CFX and CBZ. The oxidative peak currents occur at the potential of *Ca*. 0.64 V and *Ca*. 1.1 V for the CFX and CBZ, respectively. The increase in concentration caused for gradual increase in the oxidative peak current for these two analytes. Further, the oxidative peak current is plotted against the CFX and CBZ concentrations and shown in Figure 3.30(a&b) [Inset]. It si evident that a good linear relationship was obtained between the CFX or CBZ concentrations against the peak currents. Therefore, the calibration line for CFX is shown in Figure 3.30(a) (Inset). The linear regression equation is: y (µA) = 0.058 x (µg/L) + 11.9 with the correlation coefficient R^2 = 0.9992. Further, LOD and LOQ are computed and found to be 0.25 µg/L and 0.84 µg/L, respectively. Similarly, the calibration line for CBZ is shown in Figure 3.30(b)(Inset). The linear regression equation is: y (µA) = 0.0425 x (µg/L) + 11.254 (R^2= 0.9967). The LOD and LOQ for CBZ are 0.34 µg/L and 1.15 µg/L, respectively.

Further, Table 3.10 and Table 3.11 display the comparison of LOD for the electrochemical detection of ciprofloxacin and carbamazepine utilizing different advanced materials.

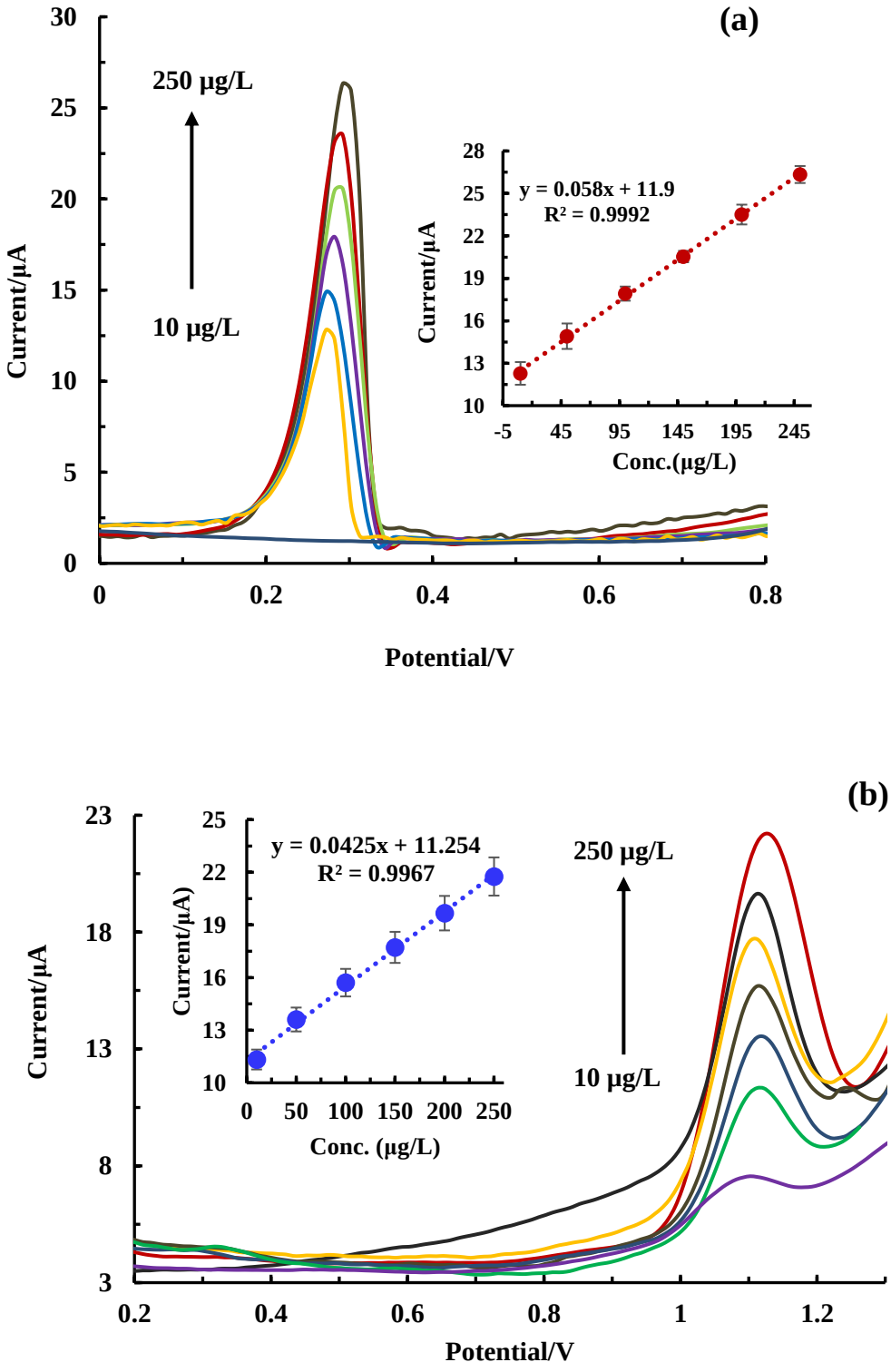

Figure 3.30: (a)The DPASV of CFX as a function of CFX concentrations; Inset: Calibration line obtained for the oxidative peak current of CFX as a function of CFX concentration; (b) The DPASV of CBZ as a function of CBZ concentrations; Inset:

Calibration line obtained for the oxidative peak current of CBZ as a function of CBZ concentration.

Table 3.10: Electrochemical detection of ciprofloxacin using different materials.

Materials	**Method**	**pH**	**Linear range**	**LOD**	**Reference**
$Au/C_3N_4/GN$	SWV	7	0.6-120 µmol/L	0.42 µmol/L	(Yuan et al., 2018)
TiO_2/PVA	DPASV	7	10-120 µmol/L	0.04 µmol/L	(Zhao et al., 2021)
$MgFe_2O_4$-MWCNTs	CV	3	0.1-1000 µmol/L	0.01 µmol/L	(Ensafi et al., 2012)
Fe@g-C_3N_4	DPASV	7	0.001-1 µmol/L	0.0054 µmol/L	(Vedhavathi et al., 2022)
Zr-MOF	**DPASV**	7	**10-250** µg/L	**0.25** µg/L	**Present studies**

Table 3.11: Electrochemical detection of carbamazepine using different materials.

Materials	**Method**	**pH**	**Linear range**	**LOD**	**Reference**
ZSM-5/TiO_2	DPASV	5	2.5-100 µmol/L	0.86 µmol/L	(Hassaninejad-Darzi & Shajie, 2018)
Fe–SnO_2	SWV	7	0.5-100 µmol/L	0.092 µmol/L	(Lavanya et al., 2016)
TiO_2NPs/	DPASV	8	0.4-100 µmol/L	0.054 µmol/L	(Tarahomi et al., 2018)

$CuO/ZnFe_2O_4$	DPASV	9	0.01-90 µmol/L	0.003 µmol/L	(Ghalkhani et al., 2022)
Zr-MOF	**DPASV**	7	**10-250** µg/L	**0.34** µg/L	**Present studies**

3.5.4. Interfering ion study

The reliability of the Zr-MOF/GCE for the electrochemical detection of CFX and CBZ is evaluated in the presence of several cations and anions *viz*., Cl^-, NO_3^-, F^-, Mg^{2+}, Pb^{2+}, Cu^{2+}, Ca^{2+} and As(III). The concentrations of these ions are taken 10-fold (500.0 µg/L) to the analyte concentration (CFX and CBZ), i.e., 50.0 µg/L (Blank). Figure 3.31, shows the interfering ions results in the detection of CFX and CBZ. It is interesting to observe that the presence of these ions does not affect significantly the detection of CFX and CBZ. The maximum percentage error lies within ±4% in the detection of CFX and CBZ. Therefore, the Zr-MOF/GCE showed fairly good selectivity for the low-level detection of CFX and CBZ. Previously it was reported that the rGO/PPR/GCE (reduced graphene oxide poly(phenol red) modified glassy carbon electrode) exhibited no interference in the presence of several heavy metals, with the maximum error percentage is less than ±5.0% about the detection of CFX (Chauhan et al., 2020).

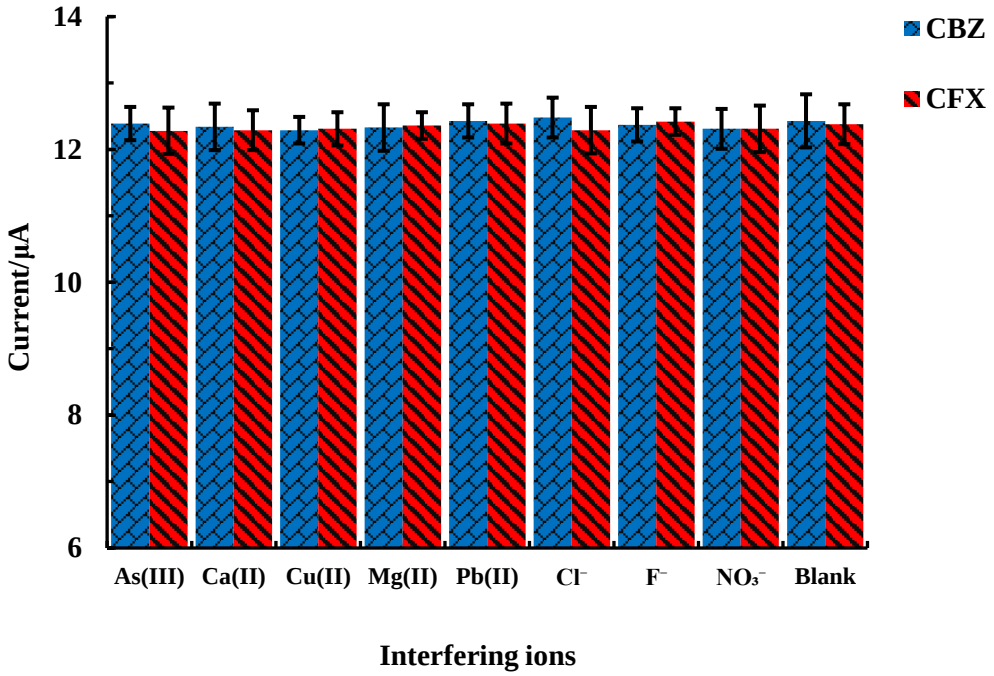

Figure 3.31: The detection of CFX and CBZ in the presence of several interfering ions using the Zr-MOF/GCE.

3.5.5. Stability of fabricated electrode

Similarly, the stability of the Zr-MOF/GCE is studied for long-term detection of CFX and CBZ (50.0 µg/L) in aqueous medium. The study is conducted for a prolonged duration, i.e., the time interval is varied from 0 hrs to 168 hrs. Each time the detection of these analytes is conducted for five replicated times and the average peak current is considered for stability tests. After each operation, the electrode was washed with distilled water and kept at room temperature for the next cycle of detection. The RSD(%) for the five replicates at different time intervals are shown in Table 3.12. Table 3.12 suggests that the shelf life of Zr-MOF/GCE is reasonably good and enables to detection of the CFX and CBZ efficiently with low RSD values. Further, the DPAS voltammograms are shown in Figure 3.32 (a&b) at different time intervals. It is evident from the figures that the peak current for these two analytes is almost identical and the

%RSD lies within 1%. These results infer that the Zr-MOF/GCE possessed long-term stability for analyte detection.

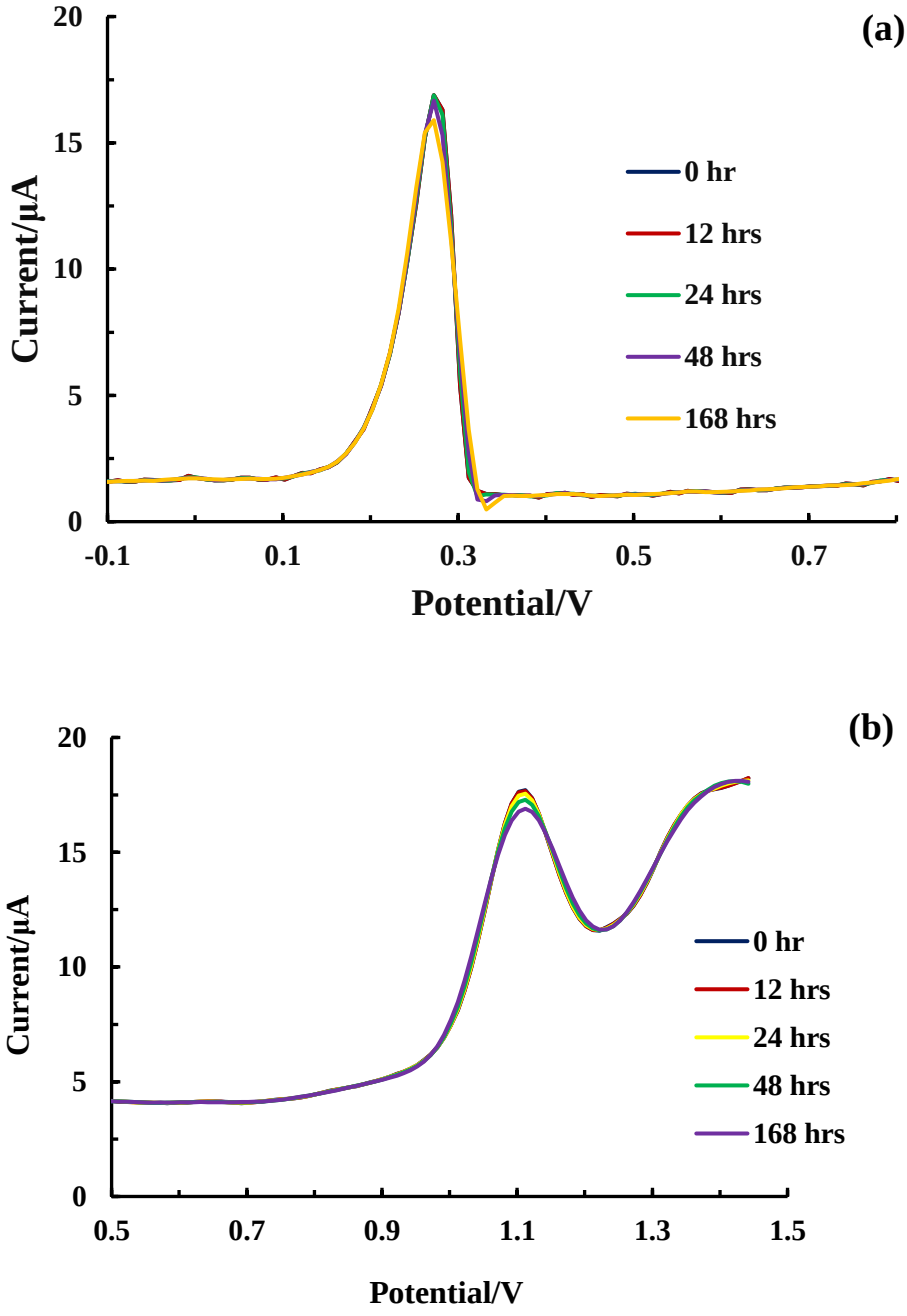

Figure 3.32: The detection of (a) Ciprofloxacin; and (b) Carbamazepine for different time intervals using the Zr-MOF/GCE.

Table 3.12: Calculation of %RSD (relative standard deviation) in different time durations of prepared electrode in the determination of CFX and CBZ (50.0 µg/L) from aqueous solution.

Time (Hrs)	RSD (%)	
	CFX	**CBZ**
0	0.94	0.78
12	0.62	0.99
24	0.46	1.33
48	0.72	1.45
168	1.21	1.16

3.5.6. Real implication and recovery rate study

The practical application of the Zr-MOF/GCE is implemented in detecting the CFX and CBZ in the natural groundwater sample. The groundwater is collected from two different locations of Tanhril village, located near Mizoram University campus, at the geographical coordinates N23.737959 and E92.675085 for sample 1 and N23.744126 and E92.674198 for sample 2. The water samples are filtered and subjected to various physicochemical analyses. The parametric analytical results are given in Table 3.13. It is evident from Table 3.13 that both the samples are contained higher concentrations of Ca and Mg. Similarly, these samples have high contents of inorganic and organic carbon contents. These samples also show the presence of NO_3^- and SO_4^{2-} at moderate levels.

Table 3.13: Analysis of real water samples (CFX and CBZ) using different analytical methods.

Parameters Studied	**Analytical Results**	
	CFX (Sample 1)	**CBZ (Sample 2)**
pH	7.28	7.39
Conductivity	127 μS/cm	398 μS/cm
Resistivity	0.0085 μOhm.cm	0.0024 μOhm.cm
Salinity	0.69 PSU	0.25 PSU
Ox. Red. Potential	204.3 mV	223.9 mV
Alkalinity	151 mg/L	35 mg/L
Al	0.03 mg/L	0.03 mg/L
NO_3^-	39.1 mg/L	34.1 mg/L
SO_4^{2-}	17.0 mg/L	14.0 mg/L
PO_4^{3-}	1.80 mg/L	0.16 mg/L
F^-	BDL	BDL
AAS analysis		
Mg	16 mg/L	20 mg/L
Ca	203 mg/L	171 mg/L
Ni	0.095 mg/L	0.079 mg/L
TOC Analysis (mg/L)		
Inorganic Carbon	36.40	37.60
NPOC	39.35	24.40

BDL: Below detection limit.

The groundwater is spiked with the known concentrations (10.0-200.0 µg/L for CFX and 10.0-100.0 µg/L for CBZ) of CFX and CBZ in the 0.1 M phosphate buffer (pH 7.0). The DPASV at different concentrations of CFX and CBZ are obtained under the optimized experimental conditions and results are shown in Figure 3.33(a & b). It is evident from the figure that an increase in CFX and CBZ concentrations caused for gradual increase in the peak current of these analytes. Further, the calibration lines are drawn between the concentrations of CFX and CBZ against the oxidative peak currents and are shown in Figure 3.33(a & b) (Inset). The obtained linear equations with correlation coefficient are $y(\mu A) = 0.051\ (\mu g/L)\ x + 13.477$ (R^2=0.9972) (for CFX) and $y(\mu A) = 0.0678x\ (\mu g/L) + 10.913$ (R^2 = 0.9988) (for CBZ). Relatively, the high value of regression coefficients indicated that a good linear relationship is obtained between the concentrations of CFX and CBZ and the respective peak currents. Therefore, good calibration lines are obtained for low-level detection of CFX and CBZ at low levels even in the natural water samples using the Zr-MOF/GCE. Therefore, the material has shown potential in the determination of CFX and CBZ at trace levels in natural water samples. Furthermore, the spiked concentrations and the recovered concentrations of CFX and CBZ are calculated and shown in Table 3.14. It is evident from Table 3.14 that very high recovery percentages of CFX and CBZ are obtained using the Zr-MOF/GCE. The recovery percentages for the CFX ranged from 95.9 to 106.4% and for the CBZ from 97.6 to 111.9%. The high percentage recovery of CFX and CBZ using the Zr-MOF/GCE infers that the Zr-MOF/GCE is promising in detecting the CFX and CBZ in the natural water sample and showed higher selectivity towards the detection of CFX and CBZ at low-level concentrations in aqueous medium.

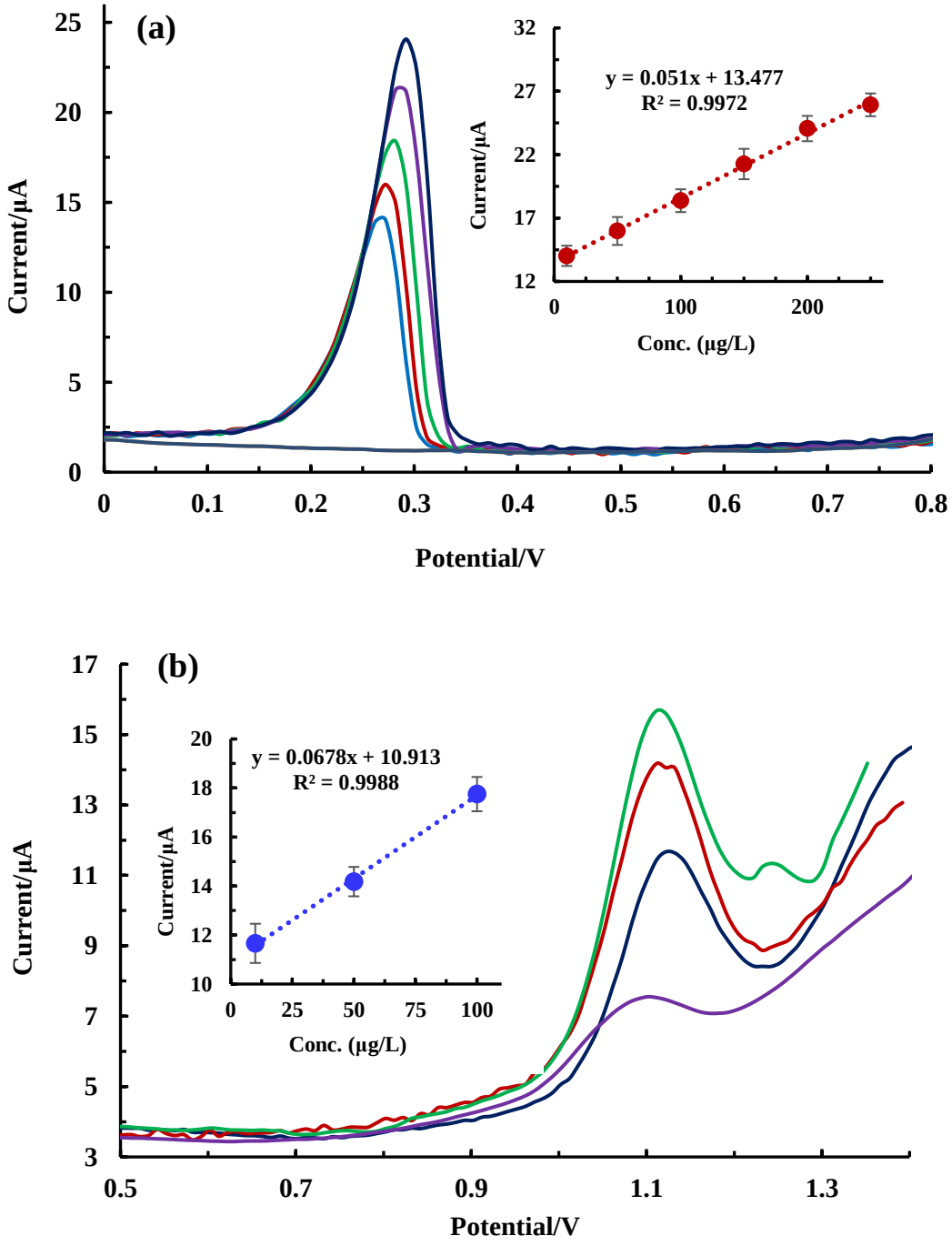

Figure 3.33: (a) DPASV of CFX using the groundwater; (Inset) Calibration lines obtained for groundwater; (b) DPASV of CBZ using the groundwater; and (Inset) Calibration lines obtained for groundwater.

Table 3.14: The recovery of CFX and CBZ in the spiked groundwater using Zr-MOF/GCE.

Real sample	Spiked amount (µg/L)	Found (µg/L)		Recovery (%)	
		CFX	CBZ	CFX	CBZ
Ground water	10	10.6	11.1	106.4	111.9
	50	49.0	48.8	98.1	97.6
	100	95.9	102.1	95.9	102.0
	150	152.6	-	101.7	-
	200	207.5	-	103.7	-

3.5.7. Conclusion

Electrochemical detection of CFX and CBZ is conducted using a Zr-MOF/GCE probe. The electrooxidation of CFX and CBZ occurred at *Ca.* 0.27 V and 1.2 V, respectively. Further, intense oxidative peaks are obtained using the Zr-MOF/GCE, however, no significant oxidation is observed using the bare GCE. Optimization parameters for DPASV measurements are: pH 7.0, deposition potential -0.2 V, and deposition time 150 sec for CFX, whereas pH 7.0, deposition potential -1.1 V, and deposition time 120 sec are optimized for the CBZ analysis. A concentration study from 10.0 µg/L to 250.0 µg/L of CFX shows an increase in peak current with an increase in concentration and obtains a good linear equation of *y* (µA) = 0.058 x (µg/L) + 11.9 (µA), and the LOD of 0.25 µg/L. Similarly, the CBZ shows the linear equation as *y* (µA) = 0.0425 x (µg/L) + 11.254 with the LOD of 0.34 µg/L. In presence of high concentrations of interfering ions such as Cl^-, NO_3^-, F^-, Mg^{2+}, Pb^{2+}, Cu^{2+}, $Ca^{2+,}$ and

As(III) show no significant change in the detection of CFX and CBZ using the Zr-MOF/GCE. The Zr-MOF/GCE is fairly stable for long-term use and showed reproducible detection results for CFX and CBZ until varied time intervals i.e., 0 to 168 hrs. The Zr-MOF/GCE showed practical implacability in the natural water samples (groundwater water) for CFX and CBZ detection. The recovery percentages for the CFX ranged from 95.9 to 106.4% and for the CBZ from 97.6 to 111.9%. The high percentage recovery of CFX and CBZ using the Zr-MOF/GCE infers that the Zr-MOF/GCE is promising in detecting the CFX and CBZ in the natural water sample and showed higher selectivity towards the detection of CFX and CBZ at low-level concentrations in an aqueous medium.

CHAPTER 4

CONCLUSIONS

4. CONCLUSION

A facile method synthesizes the Ti and Zr-based metal-organic frameworks. The Ti-MOF was obtained using the precursors of titanium butoxide and 2-amino terephthalic acid, whereas the Zr-MOF was obtained using zirconium chloride and terephthalic acid. These materials are extensively characterized using advanced analytical tools. The AFM analysis shows the heterogeneous surface of the Ti-MOF and Zr-MOF coated carbon plates. Moreover, the average roughness (R_a) of the bare glassy carbon sheet, Ti-MOF and Zr-MOF coated thin film glassy carbon plates are 1.18, 8.03, and 22.44 nm, respectively. Similarly, the SEM images of the bare carbon sheet possess a very smooth surface structure while the SEM images of the Ti-MOF and Zr-MOF coated glassy carbon plates show heterogeneous surface structure. Moreover, the Ti-MOF forms fine particles on the carbon plate surface, whereas, Zr-MOF forms a flower-like structure at the plate surface. The EDX spectra reveal that Ti-MOF shows very distinct peaks of Ti, C, N, and O elements having atomic percentages of 6.81, 60.21, 10.22, and 22.76, respectively. Similarly, the Zr-MOF shows the EDX peaks of Zr, C, and O with atomic percentages of 3.42, 66.62, and 29.96, respectively. The TEM images of these solids reveal that Ti-MOF and Zr-MOF form small-sized particles. Moreover, the TEM images show the fringes of the nanoparticles, and the d-spacings of the Ti-MOF and Zr-MOF are found to be 0.86 nm and 0.28 nm, respectively. These d spacings refer to the (110) lattice of TiO_2 and (111) lattice plane of ZrO_2, respectively, for the Ti-MOF and Zr-MOF solids. Moreover, the Image J software quantifies the mean particle size distribution of Ti-MOF and Zr-MOF, which are 6.36 nm and 5.70 nm, respectively.

The X-ray diffraction peaks at 24.71^o, 36.75^o, 47.49^o, 53.21^o, 55.11^o and 61.34^o correspond to (101), (004), (200), (211), (105), and (204) plane, respectively, confirms the presence of TiO_2 anatase phase (JCPDS card no. 21-1272). Similarly, the diffraction peaks of Zr-MOF occurred at 2θ values of 7.32° and 8.51° referring to the (111) and (200) crystal planes of ZrO_2, respectively (JCPDS no. 73-3458). The results indicate that the ZrO_2 possesses a face-cantered cubic lattice structure in the Zr-MOF. The N_2 adsorption-desorption isotherms showed that the Ti-MOF exhibits type (IV) isotherm having H3 hysteresis loop and the Zr-MOF exhibits type (I) isotherm having

H3 hysteresis loop. The specific surface area of the Ti-MOF and Zr-MOF are 1040.83 m^2g^{-1} and 840.98 $m^2\ g^{-1}$, respectively. Moreover, the pore volume and pore diameter of Ti-MOF are 0.31 cm^3g^{-1} and 3.30 nm, respectively. Similarly, the pore volume and pore diameter of Zr-MOF are 0.21 cm^3g^{-1} and 2.42 nm, respectively. The high specific surface area with low pore diameter of these two MOFs is attributed to the formation of a dense framework of Ti and Zr with the linker molecules.

The XPS survey spectrum of Ti-MOF revealed the presence of Ti, O, C, and N elements in the Ti-MOF solid. The deconvolution spectrum of Ti shows two distinct XPS peaks at the binding energies of 458.7 and 464.4 eV, referring to the Ti $2p_{1/2}$ and Ti $2p_{3/2}$, respectively, of the Ti(IV). The XPS spectra of Zr-MOF confirmed the presence of Zr, C, and O in the material. The Zr 3d spectra exhibit two distinct peaks at 182.8 and 185.2 eV, which have been identified as Zr $3d_{5/2}$ and $3d_{3/2}$, respectively, inferring the formation of Zr-O bonds within the metal cluster. The TGA curve of Ti-MOF reveals that below 200^0C, the solid loses its weight *Ca.* 10%, which is due to the elimination of remaining solvent molecules (DMF) from the pores, along with the removal of surface-absorbed moisture (H_2O). A substantial reduction in weight occurs within temperatures 350^0C to 470°C, which is ascribed to the breakdown and thermal decomposition of the organic linkers. On the other hand, the Zr-MOF displays three stages of weight loss. The first stage of weight loss (8.34%) occurred within a temperature range of 25-100^0C, which is due to the elimination of water or solvent from the solid. Further, a weight loss of 3.8% occurred within the temperature range of 100 to 420^0C due to the elimination of DMF and the dehydroxylation of the zirconium oxo-clusters. Moreover, the 41.6% weight loss of Zr-MOF occurred at temperature *Ca.* 500^0C, which is due to the thermal decomposition of organic linker molecules.

A robust drop casting method fabricates the thin film glassy carbon electrode (GCE) using these materials *viz*., Ti-MOF and Zr-MOF. Further, the two drop casted electrodes (Ti-MOF/GCE and Zr-MOF/GCE) are electrochemically characterized by using the cyclic voltammetry and electrochemical impedance spectroscopic methods and standard $[Fe(CN)_6]^{3-/4-}$ (0.002 M; prepared in 0.1 M KCl) redox couple. The diffusion-controlled redox reactions at the electrode surface showed a linear increase in redox peak current against the increase in the square root of the scan rate. The

electroactive surface area was found to be 8.95 x 10^{-4}, 14.55 x 10^{-4}, and 18.90 x 10^{-4} mm^2, respectively, for the bare GCE, Ti-MOF/GCE, and Zr-MOF/GCE. Furthermore, the ΔE value was lowered for composite and nanocomposite materials compared to the bare GCE. On the other hand, the EIS data is fitted well to the Nyquist plots. The R_{ct} values are significantly decreased using the Ti-MOF/GCE and Zr-MOF/GCE compared to the bare GCE. The R_{ct} values for the bare GCE, Ti-MOF/GCE, and Zr-MOF/GCE are 6696 Ω, 2198 Ω, and 539 Ω, respectively.

The thin film probes Ti-MOF/GCE is utilized in the trace detection of As(III), Pb(II), and Cd(II), whereas the Zr-MOF/GCE is utilized for the detection of ciprofloxacin and carbamazepine in the aqueous medium utilizing the differential pulse anodic stripping voltammetry. The DPASV optimizes the As(III) detection at the pH, deposition potential, and deposition time of 3.0, -1.2 V, and 60 sec, respectively. Electrochemical detection within the range (5 - 25) μg/L of As(III) concentration results in a good calibration line with a straight line equation of y(μA) = 0.8908x(mg/L) + 4.824 (R^2 = 0.9982). The LOD and LOQ of As(III) are 0.04 and 0.15 μg/L, respectively. Similarly, the concentration range of 0.1 to 1.0 μg/L of As(III) showed a separate calibration line with a straight line equation of y(μA) =3.85x(mg/L) +5.894 (R^2 = 0.9916) with the LOD and LOQ values are 0.01 and 0.03 μg/L, respectively. The presence of several co-existing ions viz., Mg(II), Ca(II), Cl^-, and NO_3^- do not significantly affect the detection of As(III). However, the Cu(II) and F^- affected the detection of As(III) in aqueous medium. The Ti-MOF/GCE showed fair stability for repeated and prolonged detection of As(III). Further, the recovery rate of As(III) in river water lies between 88.4% to 107.5%, and the Ti-MOF electrode is stable for 10 repeated detection cycles. The studies infer the potential of Ti-MOF for miniaturized device development for detecting the As(III).

The Ti-MOF/GCE probe detects the Pb(II) and Cd(II) at low-level concentrations in their single and simultaneous presence under the DPASV measurements. The DPAS voltammograms show intense oxidative peaks for the Pb(II) and Cd(II) at an applied potential of -0.54 V and -0.85 V, respectively. However, the GCE shows no significant oxidative peak for Pb(II) and Cd(II) in the DPASV measurements. The detection of Pb(II) under the DPASV is optimized at pH, deposition potential, and deposition time of 4.5, -1.2 V, and 60 sec, respectively.

Similarly, the pH, deposition potential, and deposition time are optimized to 4.5, -1.3 V, and 90 sec for Cd(II). Good linear calibration lines are obtained for the simultaneous detection of Pb(II) and Cd(II) between the analyte concentrations and peak current values. The calibration lines are represented with the linear equations: y(µA) =0.0636x (µg/L) + 3.496 (R^2= 0.9998) and y(µA) =0.0282x (µg/L) + 3.186 (R^2= 0.9966), respectively, for Pb(II) and Cd(II). Moreover, the LOD is found to be 1.02 µg/L and 0.59 µg/L for Pb(II) and Cd(II), respectively. The Ti-MOF/GCE demonstrates high sensitivity and selectivity for simultaneous detection of Pb(II) and Cd(II), even in the presence of high concentrations of co-existing ions *viz*., Cl^-, NO_3^-, F, Mg^{2+}, and Ca^{2+}. The Ti-MOF/GCE demonstrated significant efficacy in the simultaneous detection of Pb(II) and Cd(II) in the river water samples. The recovery percentages ranged from 90% to 114% and 102% to 112%, respectively for Cd(II) and Pb(II), in river water samples. Therefore, the fabricated Ti-MOF/GCE probe showed potential in developing the miniaturized device for the selective and sensitive detection of Pb(II) and Cd(II) simultaneously in an aqueous medium.

On the other hand, the Zr-MOF/GCE probe is utilized in the detection of some micro-pollutants *viz.*, ciprofloxacin (CFX) and carbamazepine (CBZ) in an aqueous medium. The electrooxidation of CFX and CBZ occurred at *Ca.* 0.27 V and 1.2 V, respectively. The intense oxidative peaks are obtained using the Zr-MOF/GCE, however, no significant oxidation is observed using the bare GCE. Optimization parameters for DPASV measurements are: pH 7.0, deposition potential -0.2 V and deposition time 150 sec for CFX, whereas pH 7.0, deposition potential -1.1 V and deposition time 120 sec are optimized for the CBZ analysis. A concentration study from 10.0 µg/L to 250.0 µg/L of CFX shows an increase in peak current with an increase in concentration and obtains a good linear equation of y (µA) = 0.058 x (µg/L) + 11.9 (µA), and the LOD of 0.25 µg/L. Similarly, the CBZ shows the linear equation as y (µA) = 0.0425 x (µg/L) + 11.254 with the LOD of 0.34 µg/L. In the presence of high concentrations of interfering ions such as Cl^-, NO_3^-, F^-, Mg^{2+}, Pb^{2+}, Cu^{2+}, $Ca^{2+,}$ and As(III) show no significant change in the detection of CFX and CBZ using the Zr-MOF/GCE. The Zr-MOF/GCE is fairly stable for long term use and showed reproducible detection results for CFX and CBZ until varied time intervals i.e., 0 to 168 hrs. The Zr-MOF/GCE showed practical implacability in the natural water

samples (groundwater water) for CFX and CBZ detection. The recovery percentages for the CFX ranged from 95.9 to 106.4% and for the CBZ is from 97.6 to 111.9%. The high percentage recovery of CFX and CBZ using the Zr-MOF/GCE infers that the Zr-MOF/GCE is promising in detecting the CFX and CBZ in the natural water sample and showed higher selectivity towards the detection of CFX and CBZ at low-level concentrations in aqueous medium.

Furthermore, the LOD values obtained for these pollutants using the Ti-MOF/GCE and Zr-MOF/GCE probes are summarized in Table 4.1 along with their respective maximum contamination levels prescribed by various regulatory bodies.

Table 4.1: LOD values of several contaminants obtained with modified electrodes compared to MCL levels established by WHO and the US-EPA.

Sl. No.	Working Electrode	Pollutant	LOD (µg/L)	MCL (µg/L)
1	Ti-MOF/GCE	As(III)	0.01	10 (WHO) 10 (USEPA)
2	Ti-MOF/GCE	Pb(II)	1.02	10 (WHO) 10 (USEPA)
3	Ti-MOF/GCE	Cd(II)	0.59	5 (USEPA)
4	Zr-MOF/GCE	Ciprofloxacin	0.25	-
5	Zr-MOF/GCE	Carbamazepine	0.34	-

MCL: Maximum contamination level

REFERENCES

Abdel Moneim, A. E., Dkhil, M. A., & Al-Quraishy, S. (2011). The protective effect of flaxseed oil on lead acetate-induced renal toxicity in rats. *Journal of Hazardous Materials*, *194*, 250–255. https://doi.org/10.1016/j.jhazmat.2011.07.097

Abdelkareem, M. A., Abbas, Qaisar., Mouselly, M., Alawadhi, H., & Olabi, A. G. (2022). High-performance effective metal-organic frameworks for electrochemical applications. *Journal of Science: Advanced Materials and Devices*, *7*(3), 100465. https://doi.org/10.1016/j.jsamd.2022.100465

Ahmed, S., Bakiro, M., & Alzamly, A. (2021). Photocatalytic Activities of $FeNbO_4/NH_2$-MIL-125(Ti) Composites toward the Cycloaddition of CO_2 to Propylene Oxide. *Molecules*, *26*. https://doi.org/10.3390/molecules26061693

Ali, H., Khan, E., & Ilahi, I. (2019). Environmental chemistry and ecotoxicology of hazardous heavy metals: Environmental persistence, toxicity, and bioaccumulation. *Journal of Chemistry*, *2019*, e6730305. https://doi.org/10.1155/2019/6730305

Al-Kutubi, H., Dikhtiarenko, A., Zafarani, H. R., Sudhölter, E. J. R., Gascon, J., & Rassaei, L. (2015). Facile formation of ZIF-8 thin films on ZnO nanorods. *CrystEngComm*, *17*(29), 5360–5364. https://doi.org/10.1039/C5CE00590F

Ameloot, R., Stappers, L., Fransaer, J., Alaerts, L., Sels, B. F., & De Vos, D. E. (2009). Patterned growth of metal-organic framework coatings by electrochemical synthesis. *Chemistry of Materials*, *21*(13), 2580–2582. https://doi.org/10.1021/cm900069f

An, H. K., Park, B. Y., & Kim, D. S. (2001). Crab shell for the removal of heavy metals from aqueous solution. *Water Research*, *35*(15), 3551–3556. https://doi.org/10.1016/s0043-1354(01)00099-9

Aragay, G., Pons, J., & Merkoçi, A. (2011). Enhanced electrochemical detection of heavy metals at heated graphite nanoparticle-based screen-printed electrodes. *Journal of Materials Chemistry*, *21*(12), 4326–4331. https://doi.org/10.1039/C0JM03751F

Bhanjana, G., Dilbaghi, N., Chaudhary, S., Kim, K.-H., & Kumar, S. (2016). Robust and direct electrochemical sensing of arsenic using zirconia nanocubes. *Analyst*, *141*(13), 4211–4218. https://doi.org/10.1039/C5AN02663F

Booth, A., Aga, D. S., & Wester, A. L. (2020). Retrospective analysis of the global antibiotic residues that exceed the predicted no effect concentration for antimicrobial resistance in various environmental matrices. *Environment International*, *141*, 105796. https://doi.org/10.1016/j.envint.2020.105796

Buha, A., Jugdaohsingh, R., Matovic, V., Bulat, Z., Antonijevic, B., Kerns, J. G., Goodship, A., Hart, A., & Powell, J. J. (2019). Bone mineral health is sensitively related to environmental cadmium exposure- experimental and human data. *Environmental Research*, *176*, 108539. https://doi.org/10.1016/j.envres.2019.108539

Callan, A. C., Winters, M., Barton, C., Boyce, M., & Hinwood, A. L. (2012). Children's exposure to metals: A Community-initiated study. *Archives of Environmental Contamination and Toxicology*, *62*(4), 714–722. https://doi.org/10.1007/s00244-011-9727-2

Carneiro, A. C. R., Meneguin, J. G., Santos, P. M. dos, Corazza, M. Z., Prete, M. C., Rinaldi, A. W., & Tarley, C. R. T. (2022). On-line micro-packed column solid-phase extraction of cadmium using metal-organic framework (MOF) UiO-66 with posterior determination by TS-FF-AAS. *Journal of the Brazilian Chemical Society*, *33*, 958–968. https://doi.org/10.21577/0103-5053.20220049

Carrington, M. E., Rampal, N., Madden, D. G., O'Nolan, D., Casati, N. P. M., Divitini, G., Martín-Illán, J. Á., Tricarico, M., Cepitis, R., Çamur, C., Curtin, T., Silvestre-Albero, J., Tan, J.-C., Zamora, F., Taraskin, S., Chapman, K. W., & Fairen-Jimenez, D. (2022). Sol-gel processing of a covalent organic framework for the generation of hierarchically porous monolithic adsorbents. *Chem*, *8*(11), 2961–2977. https://doi.org/10.1016/j.chempr.2022.07.013

Chakkarapani, L. D., Arumugam, S., & Brandl, M. (2024). Simultaneous electrochemical detection of L-dopa and hydrogen peroxide by poly (amido amine) dendrimer/poly (neutral red) modified sensor. *Journal of Food Composition and Analysis*, *126*, 105847. https://doi.org/10.1016/j.jfca.2023.105847

Chaturvedi, P., Shukla, P., Giri, B. S., Chowdhary, P., Chandra, R., Gupta, P., & Pandey, A. (2021). Prevalence and hazardous impact of pharmaceutical and personal care products and antibiotics in the environment: A review on emerging contaminants. *Environmental Research*, *194*, 110664. https://doi.org/10.1016/j.envres.2020.110664

Chauhan, R., Gill, A. A. S., Nate, Z., & Karpoormath, R. (2020). Highly selective electrochemical detection of ciprofloxacin using reduced graphene oxide/poly(phenol red) modified glassy carbon electrode. *Journal of Electroanalytical Chemistry*, *871*, 114254. https://doi.org/10.1016/j.jelechem.2020.114254

Chen, D., Zhao, J., Zhang, P., & Dai, S. (2019). Mechanochemical synthesis of metal–organic frameworks. *Polyhedron*, *162*, 59–64. https://doi.org/10.1016/j.poly.2019.01.024

Chen, M., Zhao, H., Liu, C.-S., Wang, X., Shi, H.-Z., & Du, M. (2015). Template-directed construction of conformational supramolecular isomers for bilayer porous metal-organic frameworks with distinct gas sorption behaviors. *Chemical Communications*, *51*(27), 6014–6017. https://doi.org/10.1039/C5CC00018A

Chen, X., Peng, X., Jiang, L., Yuan, X., Yu, H., Wang, H., Zhang, J., & Xia, Q. (2020). Recent advances in titanium metal-organic frameworks and their derived materials: Features, fabrication, and photocatalytic applications. *Chemical Engineering Journal*, *395*, 125080. https://doi.org/10.1016/j.cej.2020.125080

Cheng, H. (2023). One-Pot Preparation of HCPT@IRMOF-3 Nanoparticles for pH-responsive anticancer drug delivery. *Molecules*, *28*(23), 7703. https://doi.org/10.3390/molecules28237703

Cheng, X.-M., Dao, X.-Y., Wang, S.-Q., Zhao, J., & Sun, W.-Y. (2021). Enhanced Photocatalytic CO_2 reduction activity over NH_2-MIL-125(Ti) by facet regulation. *ACS Catalysis*, *11*(2), 650–658. https://doi.org/10.1021/acscatal.0c04426

Choi, J.-S., Son, W.-J., Kim, J., & Ahn, W.-S. (2008). Metal–organic framework MOF-5 prepared by microwave heating: Factors to be considered.

Microporous and Mesoporous Materials, *116*(1), 727–731. https://doi.org/10.1016/j.micromeso.2008.04.033

Chowdhury, M. A. Z., Banik, S., Uddin, B., Moniruzzaman, M., Karim, N., & Gan, S. H. (2012). Organophosphorus and carbamate pesticide residues detected in water samples collected from paddy and vegetable fields of the savar and dhamrai upazilas in bangladesh. *International Journal of Environmental Research and Public Health*, *9*(9), Article 9. https://doi.org/10.3390/ijerph9093318

Chowdhury, U. K., Biswas, B. K., Chowdhury, T. R., Samanta, G., Mandal, B. K., Basu, G. C., Chanda, C. R., Lodh, D., Saha, K. C., Mukherjee, S. K., Roy, S., Kabir, S., Quamruzzaman, Q., & Chakraborti, D. (2000). Groundwater arsenic contamination in Bangladesh and West Bengal, India. *Environmental Health Perspectives*, *108*(5), 393. https://doi.org/10.1289/ehp.00108393

Chu, Y., Gao, F., Gao, F., & Wang, Q. (2019). Enhanced stripping voltammetric response of Hg^{2+}, Cu^{2+}, $Pb^{2+,}$ and Cd^{2+} by ZIF-8 and its electrochemical analytical application. *Journal of Electroanalytical Chemistry*, *835*, 293–300. https://doi.org/10.1016/j.jelechem.2019.01.053

Chui, S. S.-Y., Lo, S. M.-F., Charmant, J. P. H., Orpen, A. G., & Williams, I. D. (1999). A chemically functionalizable nanoporous material $[Cu_3(TMA)_2\ (H_2O)_3](n)$. *Science*, *283*(5405), 1148–1150. Scopus. https://doi.org/10.1126/science.283.5405.1148

Clara, M., Strenn, B., & Kreuzinger, N. (2004). Carbamazepine as a possible anthropogenic marker in the aquatic environment: Investigations on the behaviour of Carbamazepine in wastewater treatment and during groundwater infiltration. *Water Research*, *38*(4), 947–954. https://doi.org/10.1016/j.watres.2003.10.058

Cohen, S. M. (2012). Postsynthetic methods for the functionalization of metal–organic frameworks. *Chemical Reviews*, *112*(2), 970–1000. https://doi.org/10.1021/cr200179u

Dali, M., Zinoubi, K., Chrouda, A., Abderrahmane, S., Cherrad, S., & Jaffrezic-Renault, N. (2018). A biosensor based on fungal soil biomass for electrochemical detection of lead (II) and cadmium (II) by differential pulse

anodic stripping voltammetry. *Journal of Electroanalytical Chemistry*, *813*, 9–19. https://doi.org/10.1016/j.jelechem.2018.02.009

Daneshvar, L. (2022). Recent advances in electrochemical screening of tricyclic drug carbamazepine: A mini-review. *Talanta Open*, *6*, 100147. https://doi.org/10.1016/j.talo.2022.100147

Deng, D., Wang, Y., Wen, S., Kang, Y., Cui, X., Tang, R., & Yang, X. (2023). Metal-organic framework composite Mn/Fe-MOF@Pd with peroxidase-like activities for sensitive colorimetric detection of hydroquinone. *Analytica Chimica Acta*, *1279*, 341797. https://doi.org/10.1016/j.aca.2023.341797

Devic, T., & Serre, C. (2014). High valence 3p and transition metal based MOFs. *Chemical Society Reviews*, *43*(16), 6097–6115. https://doi.org/10.1039/C4CS00081A

du Plessis, A. (2022). Persistent degradation: Global water quality challenges and required actions. *One Earth*, *5*(2), 129–131. https://doi.org/10.1016/j.oneear.2022.01.005

Du, Y., Xu, X., Ma, F., & Du, C. (2021). Solvent-free synthesis of iron-based metal-organic frameworks (mofs) as slow-release fertilizers. *Polymers*, *13*(4), 561. https://doi.org/10.3390/polym13040561

Duan, S., Dou, B., Lin, X., Zhao, S., Emori, W., Pan, J., Hu, H., & Xiao, H. (2021). Influence of active nanofiller ZIF-8 metal-organic framework (MOF) by microemulsion method on anticorrosion of epoxy coatings. *Colloids and Surfaces A: Physicochemical and Engineering Aspects*, *624*, 126836. https://doi.org/10.1016/j.colsurfa.2021.126836

Ebrahim, A., Ghali, M., & El-Moneim, A. A. (2024). Microporous Zr-metal-organic frameworks based-nanocomposites for thermoelectric applications. *Scientific Reports*, *14*(1), 13067. https://doi.org/10.1038/s41598-024-62317-3

El-Desoky, M. M., Morad, I., Wasfy, M. H., & Mansour, A. F. (2020). Synthesis, structural and electrical properties of PVA/TiO_2 nanocomposite films with different TiO_2 phases prepared by sol–gel technique. *Journal of Materials Science: Materials in Electronics*, *31*(20), 17574–17584. https://doi.org/10.1007/s10854-020-04313-7

Ensafi, A. A., Allafchian, A. R., & Mohammadzadeh, R. (2012). Characterization of $MgFe_2O_4$ nanoparticles as a novel electrochemical sensor: Application for the voltammetric determination of ciprofloxacin. *Analytical Sciences*, *28*(7), 705–710. https://doi.org/10.2116/analsci.28.705

Esrafili, L., Azhdari Tehrani, A., & Morsali, A. (2017). Ultrasonic assisted synthesis of two urea functionalized metal organic frameworks for phenol sensing: A comparative study. *Ultrasonics Sonochemistry*, *39*, 307–312. https://doi.org/10.1016/j.ultsonch.2017.04.039

Ettlinger, R., Lächelt, U., Gref, R., Horcajada, P., Lammers, T., Serre, C., Couvreur, P., Morris, R. E., & Wuttke, S. (2022). Toxicity of metal–organic framework nanoparticles: From essential analyses to potential applications. *Chemical Society Reviews*, *51*(2), 464–484. https://doi.org/10.1039/D1CS00918D

Fan, L., Zhang, J., Zhao, Y., Sun, C., Li, W., & Chang, Z. (2024). A robust Eu-MOF as a multi-functional fluorescence sensor for detection of benzaldehyde, Hg^{2+}, and Cr_2O72-/$CrO42$-. *Microchemical Journal*, *196*, 109712. https://doi.org/10.1016/j.microc.2023.109712

Fan, W. K., Sherryna, A., & Tahir, M. (2022). Advances in titanium carbide (Ti_3C_2Tx) mxenes and their metal-organic framework (MOF)-based nanotextures for solar energy applications: A Review. *ACS Omega*, *7*(43), 38158–38192. https://doi.org/10.1021/acsomega.2c05030

Fang, X., Wu, S., Wu, Y., Yang, W., Li, Y., He, J., Hong, P., Nie, M., Xie, C., Wu, Z., Zhang, K., Kong, L., & Liu, J. (2020). High-efficiency adsorption of norfloxacin using octahedral UIO-66-NH_2 nanomaterials: Dynamics, thermodynamics, and mechanisms. *Applied Surface Science*, *518*, 146226. https://doi.org/10.1016/j.apsusc.2020.146226

Fatema, K., Shoily, S. S., Ahsan, T., Haidar, Z., Sumit, A. F., & Sajib, A. A. (2021). Effects of arsenic and heavy metals on metabolic pathways in cells of human origin: Similarities and differences. *Toxicology Reports*, *8*, 1109–1120. https://doi.org/10.1016/j.toxrep.2021.05.015

Feng, L., Wang, K.-Y., Lv, X.-L., Yan, T.-H., & Zhou, H.-C. (2020). Hierarchically porous metal–organic frameworks: Synthetic strategies and applications.

National Science Review, *7*(11), 1743–1758. https://doi.org/10.1093/nsr/nwz170

Flora, G., Gupta, D., & Tiwari, A. (2012). Toxicity of lead: A review with recent updates. *Interdisciplinary Toxicology*, *5*(2), 47–58. https://doi.org/10.2478/v10102-012-0009-2

Fort, C. I., Cotet, L. C., Vulpoi, A., Turdean, G. L., Danciu, V., Baia, L., & Popescu, I. C. (2015). Bismuth doped carbon xerogel nanocomposite incorporated in chitosan matrix for ultrasensitive voltammetric detection of Pb(II) and Cd(II). *Sensors and Actuators B: Chemical*, *220*, 712–719. https://doi.org/10.1016/j.snb.2015.05.124

Gao, K., Huang, D., Hou, L., An, X., Takizawa, S., & Yang, Y. (2024). Efficient degradation of carbamazepine by sulfate doped LDO/CN in the photo-assisted peroxymonosulfate system. *Chemical Engineering Journal*, *482*, 149034. https://doi.org/10.1016/j.cej.2024.149034

Gao, X., Peng, W., Tang, G., Guo, Q., & Luo, Y. (2018). Highly efficient and visible-light-driven BiOCl for photocatalytic degradation of carbamazepine. *Journal of Alloys and Compounds*, *757*, 455–465. https://doi.org/10.1016/j.jallcom.2018.05.081

García-García, M. A., Domínguez-Renedo, O., Alonso-Lomillo, A., & Arcos-Martínez, M. J. (2009). Electrochemical methods of carbamazepine determination. *Sensor Letters*, *7*(4), 586–591. https://doi.org/10.1166/sl.2009.1114

Gayen, P., & Chaplin, B. P. (2016). Selective electrochemical detection of ciprofloxacin with a porous nafion/multiwalled carbon nanotube composite film electrode. *ACS Applied Materials & Interfaces*, *8*(3), 1615–1626. https://doi.org/10.1021/acsami.5b07337

Genchi, G., Sinicropi, M. S., Lauria, G., Carocci, A., & Catalano, A. (2020). The effects of cadmium toxicity. *International Journal of Environmental Research and Public Health*, *17*(11), Article 11. https://doi.org/10.3390/ijerph17113782

Ghalkhani, M., Khosrowshahi, E. M., Sohouli, E., Eskandari, K., Aghaei, M., Rahimi-Nasrabadi, M., Sobhani-Nasab, A., Banafshe, H., & Kouchaki, E. (2022). Electrochemical monitoring of carbamazepine in biological fluids by a glassy

carbon electrode modified with CuO/$ZnFe_2O_4$/rGO nanocomposite. *Surfaces and Interfaces*, *30*, 101943. https://doi.org/10.1016/j.surfin.2022.101943

Głowniak, S., Szczęśniak, B., Choma, J., & Jaroniec, M. (2021). Mechanochemistry: toward green synthesis of metal–organic frameworks. *Materials Today*, *46*, 109–124. https://doi.org/10.1016/j.mattod.2021.01.008

Godt, J., Scheidig, F., Grosse-Siestrup, C., Esche, V., Brandenburg, P., Reich, A., & Groneberg, D. A. (2006). The toxicity of cadmium and resulting hazards for human health. *Journal of Occupational Medicine and Toxicology*, *1*(1), 22. https://doi.org/10.1186/1745-6673-1-22

Ha, J., Lee, J. H., & Moon, H. R. (2019). Alterations to secondary building units of metal–organic frameworks for the development of new functions. *Inorganic Chemistry Frontiers*, *7*(1), 12–27. https://doi.org/10.1039/C9QI01119F

Halper, S. R., Do, L., Stork, J. R., & Cohen, S. M. (2006). Topological control in heterometallic metal−organic frameworks by anion templating and metalloligand design. *Journal of the American Chemical Society*, *128*(47), 15255–15268. https://doi.org/10.1021/ja0645483

Haque, E., Khan, N. A., Kim, C. M., & Jhung, S. H. (2011). Syntheses of metal–organic frameworks and aluminophosphates under microwave heating: quantitative analysis of accelerations. *Crystal Growth & Design*, *11*(10), 4413–4421. https://doi.org/10.1021/cg200594e

Hasani, A., Do, H. H., Tekalgne, M., Hong, S. H., Jang, H. W., & Kim, S. Y. (2020). Recent progress of two-dimensional materials and metal–organic framework-based taste sensors. *Journal of the Korean Ceramic Society*, *57*(4), 353–367. https://doi.org/10.1007/s43207-020-00047-8

Hassaninejad-Darzi, S. K., & Shajie, F. (2018). Simultaneous determination of acetaminophen, pramipexole and carbamazepine by ZSM-5 nanozeolite and TiO2 nanoparticles modified carbon paste electrode. *Materials Science and Engineering: C*, *91*, 64–77. https://doi.org/10.1016/j.msec.2018.05.022

He, Q., Liang, J.-J., Chen, L.-X., Chen, S.-L., Zheng, H.-L., Liu, H.-X., & Zhang, H.-J. (2020). Removal of the environmental pollutant carbamazepine using molecular imprinted adsorbents: Molecular simulation, adsorption properties,

and mechanisms. *Water Research*, *168*, 115164. https://doi.org/10.1016/j.watres.2019.115164

He, S., Wu, L., Li, X., Sun, H., Xiong, T., Liu, J., Huang, C., Xu, H., Sun, H., Chen, W., Gref, R., & Zhang, J. (2021). Metal-organic frameworks for advanced drug delivery. *Acta Pharmaceutica Sinica B*, *11*(8), 2362–2395. https://doi.org/10.1016/j.apsb.2021.03.019

He, Z. L., Yang, X. E., & Stoffella, P. J. (2005). Trace elements in agroecosystems and impacts on the environment. *Journal of Trace Elements in Medicine and Biology*, *19*(2), 125–140. https://doi.org/10.1016/j.jtemb.2005.02.010

Hendon, C. H., Tiana, D., Fontecave, M., Sanchez, C., D'arras, L., Sassoye, C., Rozes, L., Mellot-Draznieks, C., & Walsh, A. (2013). Engineering the optical response of the titanium-mil-125 metal–organic framework through ligand functionalization. *Journal of the American Chemical Society*, *135*(30), 10942–10945. https://doi.org/10.1021/ja405350u

Horcajada, P., Surblé, S., Serre, C., Hong, D.-Y., Seo, Y.-K., Chang, J.-S., Grenèche, J.-M., Margiolaki, I., & Férey, G. (2007). Synthesis and catalytic properties of MIL-100(Fe), an iron(III) carboxylate with large pores. *Chemical Communications*, *27*, 2820–2822. https://doi.org/10.1039/B704325B

Hossain, Md. S., Ahmed, Md. K., Sarker, S., & Rahman, M. S. (2020). Seasonal variations of trace metals from water and sediment samples in the northern Bay of Bengal. *Ecotoxicology and Environmental Safety*, *193*, 110347. https://doi.org/10.1016/j.ecoenv.2020.110347

Hosseini, H., Ahmar, H., Dehghani, A., Bagheri, A., Fakhari, A. R., & Amini, M. M. (2013). Au-SH-SiO_2 nanoparticles supported on metal-organic framework (Au-SH-SiO_2@Cu-MOF) as a sensor for electrocatalytic oxidation and determination of hydrazine. *Electrochimica Acta*, *88*, 301–309. https://doi.org/10.1016/j.electacta.2012.10.064

Hu, H., Lu, W., Liu, X., Meng, F., & Zhu, J. (2021). A high-response electrochemical As(III) sensor using Fe_3O_4–rGO nanocomposite materials. *Chemosensors*, *9*(6), Article 6. https://doi.org/10.3390/chemosensors9060150

Hu, S., Zhang, S., Qin, J., Cai, K., Peng, C., Luo, L., Gu, Y., & Mei, Y. (2024). Simultaneous determination of lead and cadmium in water by metal oxide

framework complex-modified glassy carbon electrodes. *Microchemical Journal*, *205*, 111154. https://doi.org/10.1016/j.microc.2024.111154

Hu, X., Qian, J., Yang, J., Hu, X., Zou, Y., & Yang, N. (2023). Construction of Ce-MOF@COF hybrid nanostructure with controllable thickness for the electrochemical sensitive detection of metol. *Journal of Electroanalytical Chemistry*, *947*, 117756. https://doi.org/10.1016/j.jelechem.2023.117756

Hu, Y., Dai, L., Liu, D., & Du, W. (2018). Rationally designing hydrophobic UiO-66 support for the enhanced enzymatic performance of immobilized lipase. *Green Chemistry*, *20*(19), 4500–4506. https://doi.org/10.1039/C8GC01284A

Huang, H.-Q., Li, Y.-Y., Chen, S.-H., Liu, Z.-G., Cui, Y.-M., Li, H.-Q., Guo, Z., & Huang, X.-J. (2022). Noble-metal-free Fe_3O_4/Co_3S_4 nanosheets with oxygen vacancies as an efficient electrocatalyst for highly sensitive electrochemical detection of As(III). *Analytica Chimica Acta*, *1189*, 339208. https://doi.org/10.1016/j.aca.2021.339208

Jacobo-Estrada, T., Cardenas-Gonzalez, M., Santoyo-Sánchez, M., Parada-Cruz, B., Uria-Galicia, E., Arreola-Mendoza, L., & Barbier, O. (2016). Evaluation of kidney injury biomarkers in rat amniotic fluid after gestational exposure to cadmium. *Journal of Applied Toxicology*, *36*(9), 1183–1193. https://doi.org/10.1002/jat.3286

Jiang, T.-J., Guo, Z., Liu, J.-H., & Huang, X.-J. (2016). Gold electrode modified with ultrathin SnO_2 nanosheets with high reactive exposed surface for electrochemical sensing of As(III). *Electrochimica Acta*, *191*, 142–148. https://doi.org/10.1016/j.electacta.2015.12.196

Jin, K. Y., & Aslam, M. S. (2019). The occurrence of pharmaceutical waste in different parts of the world*:* A scoping review (e27951v1). PeerJ Inc. https://doi.org/10.7287/peerj.preprints.27951v1

Jin, T., Hwang, Y. K., Hong, D.-Y., Jhung, S. H., Hwang, J.-S., Park, S.-E., Kim, Y. H., & Chang, J.-S. (2007). Microwave synthesis, characterization and catalytic properties of titanium-incorporated ZSM-5 zeolite. *Research on Chemical Intermediates*, *33*(6), 501–512. https://doi.org/10.1163/156856707782565804

Jomova, K., Makova, M., Alomar, S. Y., Alwasel, S. H., Nepovimova, E., Kuca, K., Rhodes, C. J., & Valko, M. (2022). Essential metals in health and disease.

Chemico-Biological Interactions, *367*, 110173. https://doi.org/10.1016/j.cbi.2022.110173

Joseph, J., Iftekhar, S., Srivastava, V., Fallah, Z., Zare, E. N., & Sillanpää, M. (2021). Iron-based metal-organic framework: Synthesis, structure and current technologies for water reclamation with deep insight into framework integrity. *Chemosphere*, *284*, 131171. https://doi.org/10.1016/j.chemosphere.2021.131171

Jung, K.-W., Choi, B. H., Lee, S. Y., Ahn, K.-H., & Lee, Y. J. (2018). Green synthesis of aluminum-based metal organic framework for the removal of azo dye Acid Black 1 from aqueous media. *Journal of Industrial and Engineering Chemistry*, *67*, 316–325. https://doi.org/10.1016/j.jiec.2018.07.003

Kajal, N., Singh, V., Gupta, R., & Gautam, S. (2022). Metal organic frameworks for electrochemical sensor applications: A review. *Environmental Research*, *204*, 112320. https://doi.org/10.1016/j.envres.2021.112320

Kang, W., Pei, X., Rusinek, C. A., Bange, A., Haynes, E. N., Heineman, W. R., & Papautsky, I. (2017). Determination of lead with a copper-based electrochemical sensor. *Analytical Chemistry*, *89*(6), 3345–3352. https://doi.org/10.1021/acs.analchem.6b03894

Kaur, G., Anthwal, A., Kandwal, P., & Sud, D. (2023). Mechanochemical synthesis and theoretical investigations of Fe (II) based MOF containing 4,4′-bipyridine with ordained intercalated p-aminobenzoic acid: Application as fluoroprobe for detection of carbonyl group. *Inorganica Chimica Acta*, *545*, 121248. https://doi.org/10.1016/j.ica.2022.121248

Kaur, M., Mehta, S. K., & Kansal, S. K. (2020). Amine-functionalized titanium metal-organic framework (NH2-MIL-125(Ti)): A novel fluorescent sensor for the highly selective sensing of copper ions. *Materials Chemistry and Physics*, *254*, 123539. https://doi.org/10.1016/j.matchemphys.2020.123539

kaur, R., Garkal, A., Sarode, L., Bangar, P., Mehta, T., Singh, D. P., & Rawal, R. (2024). Understanding arsenic toxicity: Implications for environmental exposure and human health. *Journal of Hazardous Materials Letters*, *5*, 100090. https://doi.org/10.1016/j.hazl.2023.100090

Kazemi, A., Moghadaskhou, F., Pordsari, M. A., Manteghi, F., Tadjarodi, A., & Ghaemi, A. (2023). Enhanced CO_2 capture potential of UiO-66-NH_2 synthesized by sonochemical method: Experimental findings and performance evaluation. *Scientific Reports*, *13*(1), 19891. https://doi.org/10.1038/s41598-023-47221-6

Keil, D. E., Berger-Ritchie, J., & McMillin, G. A. (2011). Testing for toxic elements: A focus on arsenic, cadmium, lead, and mercury. *Laboratory Medicine*, *42*(12), 735–742. https://doi.org/10.1309/LMYKGU05BEPE7IAW

Khan, M. S., Khalid, M., Ahmad, M. S., Shahid, M., & Ahmad, M. (2019). Three-in-one is really better: Exploring the sensing and adsorption properties in a newly designed metal–organic system incorporating a copper(II) ion. *Dalton Transactions*, *48*(34), 12918–12932. https://doi.org/10.1039/C9DT02578B

Khan, N. A., & Jhung, S.-H. (2009). Facile syntheses of metal-organic framework $Cu_3(BTC)_2(H_2O)_3$ under ultrasound. *Bulletin of the Korean Chemical Society*, *30*(12), 2921–2926. https://doi.org/10.5012/BKCS.2009.30.12.2921

Kraemer, S. A., Ramachandran, A., & Perron, G. G. (2019). Antibiotic pollution in the environment: From microbial ecology to public policy. *Microorganisms*, *7*(6), Article 6. https://doi.org/10.3390/microorganisms7060180

Kubra, K., Mondol, A. H., Ali, M. M., Palash, Md. A. U., Islam, Md. S., Ahmed, A. S. S., Masuda, M. A., Islam, A. R. Md. T., Bhuyan, Md. S., Rahman, Md. Z., & Rahman, Md. M. (2022). Pollution level of trace metals (As, Pb, Cr and Cd) in the sediment of Rupsha River, Bangladesh: Assessment of ecological and human health risks. *Frontiers in Environmental Science*, *10*. https://www.frontiersin.org/articles/10.3389/fenvs.2022.778544

Kujawa, J., Al-Gharabli, S., Muzioł, T. M., Knozowska, K., Li, G., Dumée, L. F., & Kujawski, W. (2021). Crystalline porous frameworks as nano-enhancers for membrane liquid separation – Recent developments. *Coordination Chemistry Reviews*, *440*, 213969. https://doi.org/10.1016/j.ccr.2021.213969

Kuppusamy, S., Jagadeesan, D., Mohan, A. M., Pavoor Veedu, A., Jiji, A. E., John, A. M., & Deivasigamani, P. (2023). NH2-MIL-125 MOF integrated translucent mesoporous polymer monolith as dual-light responsive new-generation photocatalyst for the expeditious decontamination of perennial

pharmaceuticals. *Journal of Environmental Chemical Engineering*, *11*(5), 110355. https://doi.org/10.1016/j.jece.2023.110355

Lakkis, N. A., Musharafieh, U. M., Issa, H. G., & Osman, M. H. (2023). Lung cancer and risk factors in lebanon: Epidemiology, temporal trends, and comparison to countries from different regions in the world. *Cancer Control*, *30*, 10732748231169596. https://doi.org/10.1177/10732748231169596

Lalmalsawmi, J., Sarikokba, Tiwari, D., & Kim, D.-J. (2022). Simultaneous detection of Cd^{2+} and Pb^{2+} by differential pulse anodic stripping voltammetry: Use of highly efficient novel Ag^0(NPs) decorated silane grafted bentonite material. *Journal of Electroanalytical Chemistry*, *918*, 116490. https://doi.org/10.1016/j.jelechem.2022.116490

Lalmalsawmi, J., Zirlianngura, Tiwari, D., & Lee, S.-M. (2020). Low cost, highly sensitive and selective electrochemical detection of arsenic (III) using silane grafted based nanocomposite. *Environmental Engineering Research*, *25*(4), 579–587. https://doi.org/10.4491/eer.2019.245

Lalmalsawmi, J., Zirlianngura, Tiwari, D., Lee, S.-M., & Kim, D.-J. (2021). Indigenously synthesized nanocomposite materials: Use of nanocomposite as novel sensing platform for trace detection of Pb^{2+}. *Journal of Electroanalytical Chemistry*, *897*, 115578. https://doi.org/10.1016/j.jelechem.2021.115578

Lavanya, N., Sekar, C., Ficarra, S., Tellone, E., Bonavita, A., Leonardi, S. G., & Neri, G. (2016). A novel disposable electrochemical sensor for determination of carbamazepine based on Fe doped SnO_2 nanoparticles modified screen-printed carbon electrode. *Materials Science & Engineering. C, Materials for Biological Applications*, *62*, 53–60. https://doi.org/10.1016/j.msec.2016.01.027

Lee, S. M., Zirlianngura, Anjudikkal, J., & Tiwari, D. (2016). Electrochemical sensor for trace determination of cadmium(II) from aqueous solutions: Use of hybrid materials precursors to natural clays. *International Journal of Environmental Analytical Chemistry*, *96*(5), 490–504. https://doi.org/10.1080/03067319.2016.1172220

Li, H., Eddaoudi, M., O'Keeffe, M., & Yaghi, O. M. (1999). Design and synthesis of an exceptionally stable and highly porous metal-organic framework. *Nature*, *402*(6759), 276–279. https://doi.org/10.1038/46248

Li, H., Wang, T., Chu, H., Rokhum, S. L., Zhang, Y., Yu, H., Xiao, Q., Guo, M., Ma, X., Li, S., & Li, G. (2024). In–situ modification of UiO–66(Zr) organic ligand to synthesize highly recyclable solid acid for biodiesel production. *Chemical Engineering Research and Design*, *205*, 713–721. https://doi.org/10.1016/j.cherd.2024.04.040

Li, M., Shah, N. H., Zhang, P., Chen, P., Cui, Y., Jiang, Y., & Wang, Y. (2023). Mechanism, modification and application of silver-based photocatalysts. *Materials Today Sustainability*, *22*, 100409. https://doi.org/10.1016/j.mtsust.2023.100409

Li, M., Zhang, G., Shi, Y., Zhou, H., Zhang, Y., & Pang, H. (2023). Progress and perspectives of conducting metal–organic frameworks for electrochemical energy storage and conversion. *Chemistry*, *5*(4), Article 4. https://doi.org/10.3390/chemistry5040161

Liang, J., & Liang, K. (2023). Nanobiohybrids: Synthesis strategies and environmental applications from micropollutants sensing and removal to global warming mitigation. *Environmental Research*, *232*, 116317. https://doi.org/10.1016/j.envres.2023.116317

Lin, J.-L., Lin-Tan, D.-T., Hsu, K.-H., & Yu, C.-C. (2003). Environmental lead exposure and progression of chronic renal diseases in patients without diabetes. *The New England Journal of Medicine*, *348*(4), 277–286. https://doi.org/10.1056/NEJMoa021672

Lin, X., Zeng, W., Liu, M., Zhong, Q., Su, T., Gong, L., & Liu, Y. (2023). Amino-modified Mg-MOF-74: Synthesis, characterization and CO_2 adsorption performance. *Environmental Engineering Research*, *28*(1). https://doi.org/10.4491/eer.2021.569

Liu, H., Zhao, Y., Zhou, C., Mu, B., & Chen, L. (2021). Microwave-assisted synthesis of Zr-based metal–organic framework (Zr-fum-fcu-MOF) for gas adsorption separation. *Chemical Physics Letters*, *780*, 138906. https://doi.org/10.1016/j.cplett.2021.138906

Liu, K., Hao, J., Zeng, Y., Dai, F., & Gu, P. (2013). Neurotoxicity and biomarkers of lead exposure: A review. *Chinese Medical Sciences Journal*, *28*(3), 178–188. https://doi.org/10.1016/S1001-9294(13)60045-0

Liu, X., Yang, H., Diao, Y., He, Q., Lu, C., Singh, A., Kumar, A., Liu, J., & Lan, Q. (2022). Recent advances in the electrochemical applications of Ni-based metal organic frameworks (Ni-MOFs) and their derivatives. *Chemosphere*, *307*, 135729. https://doi.org/10.1016/j.chemosphere.2022.135729

Loiseau, T., Volkringer, C., Haouas, M., Taulelle, F., & Férey, G. (2015). Crystal chemistry of aluminium carboxylates: From molecular species towards porous infinite three-dimensional networks. *Comptes Rendus. Chimie*, *18*(12), 1350–1369. https://doi.org/10.1016/j.crci.2015.08.006

Luo, Q., Guo, L., & Zhang, H. (2023). Electrochemical sensing based on metal–organic frameworks-derived carbon/molybdenum disulfide composites with superstructure and synergistic catalysis. *ACS Applied Materials & Interfaces*, *15*(44), 52021–52028. https://doi.org/10.1021/acsami.3c13740

Madivoli, E. S., Kareru, P. G., Makhanu, D. S., Wandera, K. S., Maina, E. G., Wanakai, S. I., & Kimani, P. K. (2020). Synthesis of spherical titanium dioxide microspheres and its application to degrade rifampicin. *Environmental Nanotechnology, Monitoring & Management*, *14*, 100327. https://doi.org/10.1016/j.enmm.2020.100327

Magesh, N. S., Krishnakumar, S., Chandrasekar, N., & Soundranayagam, J. P. (2013). Groundwater quality assessment using WQI and GIS techniques, Dindigul district, Tamil Nadu, India. *Arabian Journal of Geosciences*, *6*(11), 4179–4189. https://doi.org/10.1007/s12517-012-0673-8

Masiol, M., & Harrison, R. M. (2014). Aircraft engine exhaust emissions and other airport-related contributions to ambient air pollution: A review. *Atmospheric Environment (Oxford, England: 1994)*, *95*, 409–455. https://doi.org/10.1016/j.atmosenv.2014.05.070

Mikuła, B., Puzio, B., & Feist, B. (2009). Application of 1,10-phenanthroline for preconcentration of selected heavy metals on silica gel. *Microchimica Acta*, *166*(3), 337–341. https://doi.org/10.1007/s00604-009-0199-2

Min, H., Han, Z., Wang, M., Li, Y., Zhou, T., Shi, W., & Cheng, P. (2020). A water-stable terbium metal–organic framework as a highly sensitive fluorescent sensor for nitrite. *Inorganic Chemistry Frontiers*, *7*(18), 3379–3385. https://doi.org/10.1039/D0QI00780C

Mintz Hemed, N., Convertino, A., & Shacham-Diamand, Y. (2018). Alkaline phosphatase detection using electrochemical impedance of anti-alkaline phosphatase antibody (Ab354) functionalized silicon-nanowire-forest in phosphate buffer solution. *Sensors and Actuators B: Chemical*, *259*, 809–815. https://doi.org/10.1016/j.snb.2017.12.136

Mohan, B., Priyanka, Singh, G., Chauhan, A., Pombeiro, A. J. L., & Ren, P. (2023). Metal-organic frameworks (MOFs) based luminescent and electrochemical sensors for food contaminant detection. *Journal of Hazardous Materials*, *453*, 131324. https://doi.org/10.1016/j.jhazmat.2023.131324

Motegi, H., Yano, K., Setoyama, N., Matsuoka, Y., Ohmura, T., & Usuki, A. (2017). A facile synthesis of UiO-66 systems and their hydrothermal stability. *Journal of Porous Materials*, *24*(5), 1327–1333. https://doi.org/10.1007/s10934-017-0374-5

Muelas-Ramos, V., Sampaio, M. J., Silva, C. G., Bedia, J., Rodriguez, J. J., Faria, J. L., & Belver, C. (2021). Degradation of diclofenac in water under LED irradiation using combined g-C_3N_4/NH_2-MIL-125 photocatalysts. *Journal of Hazardous Materials*, *416*, 126199. https://doi.org/10.1016/j.jhazmat.2021.126199

Neto, O. J. de L., Frós, A. C. de O., Barros, B. S., Monteiro, A. F. de F., & Kulesza, J. (2019). Rapid and efficient electrochemical synthesis of a zinc-based nano-MOF for Ibuprofen adsorption. *New Journal of Chemistry*, *43*(14), 5518–5524. https://doi.org/10.1039/C8NJ06420B

Ngumba, E., Gachanja, A., & Tuhkanen, T. (2016). Occurrence of selected antibiotics and antiretroviral drugs in Nairobi River Basin, Kenya. *Science of The Total Environment*, *539*, 206–213. https://doi.org/10.1016/j.scitotenv.2015.08.139

Oprea, T. I. (2002). Current trends in lead discovery: Are we looking for the appropriate properties? *Journal of Computer-Aided Molecular Design*, *16*(5), 325–334. https://doi.org/10.1023/A:1020877402759

Pandey, A., Dhas, N., Deshmukh, P., Caro, C., Patil, P., Luisa García-Martín, M., Padya, B., Nikam, A., Mehta, T., & Mutalik, S. (2020). Heterogeneous surface architectured metal-organic frameworks for cancer therapy, imaging, and biosensing: A state-of-the-art review. *Coordination Chemistry Reviews*, *409*, 213212. https://doi.org/10.1016/j.ccr.2020.213212

Pandiyan, J., Mahboob, S., Govindarajan, M., Al-Ghanim, K. A., Ahmed, Z., Al-Mulhm, N., Jagadheesan, R., & Krishnappa, K. (2021). An assessment of level of heavy metals pollution in the water, sediment and aquatic organisms: A perspective of tackling environmental threats for food security. *Saudi Journal of Biological Sciences*, *28*(2), 1218–1225. https://doi.org/10.1016/j.sjbs.2020.11.072

Paraschiv, S., Paraschiv, L. S., & Serban, A. (2023). An overview of energy intensity of drinking water production and wastewater treatment. *Energy Reports*, *9*, 118–123. https://doi.org/10.1016/j.egyr.2023.08.074

Philips, M. F., Gopalan, A. I., & Lee, K.-P. (2012). Development of a novel cyano group containing electrochemically deposited polymer film for ultrasensitive simultaneous detection of trace level cadmium and lead. *Journal of Hazardous Materials*, *237–238*, 46–54. https://doi.org/10.1016/j.jhazmat.2012.07.069

Plum, L. M., Rink, L., & Haase, H. (2010). The Essential toxin: Impact of zinc on human health. *International Journal of Environmental Research and Public Health*, *7*(4), Article 4. https://doi.org/10.3390/ijerph7041342

Prieto-Rodriguez, L., Miralles-Cuevas, S., Oller, I., Agüera, A., Puma, G. L., & Malato, S. (2012). Treatment of emerging contaminants in wastewater treatment plants (WWTP) effluents by solar photocatalysis using low TiO_2 concentrations. *Journal of Hazardous Materials*, *211–212*, 131–137. https://doi.org/10.1016/j.jhazmat.2011.09.008

Prochowicz, D., Sokołowski, K., Justyniak, I., Kornowicz, A., Fairen-Jimenez, D., Friščić, T., & Lewiński, J. (2015). A mechanochemical strategy for IRMOF assembly based on pre-designed oxo-zinc precursors. *Chemical Communications*, *51*(19), 4032–4035. https://doi.org/10.1039/C4CC09917F

Qamar, K., Nchasi, G., Mirha, H. T., Siddiqui, J. A., Jahangir, K., Shaeen, S. K., Islam, Z., & Essar, M. Y. (2022). Water sanitation problem in Pakistan: A review on

disease prevalence, strategies for treatment and prevention. *Annals of Medicine and Surgery*, *82*, 104709. https://doi.org/10.1016/j.amsu.2022.104709

Qi, Y., Luo, F., Che, Y., & Zheng, J. (2008). Hydrothermal synthesis of metal−organic frameworks based on aromatic polycarboxylate and flexible bis(imidazole) ligands. *Crystal Growth & Design*, *8*(2), 606–611. https://doi.org/10.1021/cg700758c

Rafati-Rahimzadeh, M., Rafati-Rahimzadeh, M., Kazemi, S., & Moghadamnia, A. (2017). Cadmium toxicity and treatment: An update. *Caspian Journal of Internal Medicine*, *8*(3), 135–145. https://doi.org/10.22088/cjim.8.3.135

Rahim, M. A., Mostafa, M. G., Rahim, M. A., & Mostafa, M. G. (2021). Impact of sugar mills effluent on environment around mills area. *AIMS Environmental Science*, *8*(1), Article Environ-08-01-06. https://doi.org/10.3934/environsci.2021006

Rana, A., Baig, N., & Saleh, T. A. (2019). Electrochemically pretreated carbon electrodes and their electroanalytical applications – A review. *Journal of Electroanalytical Chemistry*, *833*, 313–332. https://doi.org/10.1016/j.jelechem.2018.12.019

Ren, B., Sudarsanam, P., Kandjani, A. E., Hillary, B., Amin, M. H., Bhargava, S. K., & Jones, L. A. (2018). Electrochemical detection of As (III) on a manganese oxide-ceria (Mn_2O_3/CeO_2) nanocube modified Au electrode. *Electroanalysis*, *30*(5), 928–936. https://doi.org/10.1002/elan.201700662

Ren, J., Langmi, H. W., North, B. C., & Mathe, M. (2015). Review on processing of metal–organic framework (MOF) materials towards system integration for hydrogen storage. *International Journal of Energy Research*, *39*(5), 607–620. https://doi.org/10.1002/er.3255

Ren, L., Ma, J., Chen, M., Qiao, Y., Dai, R., Li, X., & Wang, Z. (2022). Recent advances in electrocatalytic membrane for the removal of micropollutants from water and wastewater. *iScience*, *25*(5), 104342. https://doi.org/10.1016/j.isci.2022.104342

Rogowska, J., Cieszynska-Semenowicz, M., Ratajczyk, W., & Wolska, L. (2020). Micropollutants in treated wastewater. *Ambio*, *49*(2), 487–503. https://doi.org/10.1007/s13280-019-01219-5

Saha, N., Volpe, M., Fiori, L., Volpe, R., Messineo, A., & Reza, M. T. (2020). Cationic dye adsorption on hydrochars of winery and citrus juice industries residues: Performance, mechanism, and thermodynamics. *Energies*, *13*(18), Article 18. https://doi.org/10.3390/en13184686

Samsudin, M. F., Amin, M. F. M., Omar, S. A. S., Rasat, M. S. M., & Salam, M. A. (2020). Analysis of water stress index (WSI) for district surrounding ulu sat forest reserve, Kelantan, Malaysia. *IOP Conference Series: Earth and Environmental Science*, *549*(1), 012015. https://doi.org/10.1088/1755-1315/549/1/012015

Sarikokba, Lalmalsawmi, J., Kumar Prasad, S., & Tiwari, D. (2022). Development of a novel sensor with high sensitivity for electroanalytical determination of bisphenol A based on chitosan-3-mercaptopropyl trimethoxysilane modified glassy carbon electrode. *Microchemical Journal*, *181*, 107748. https://doi.org/10.1016/j.microc.2022.107748

Sarikokba, S., Lalmalsawmi, J., Lee, S. M., & Tiwari, D. (2022). Highly efficient functionalized chitosan in the development of electrochemical sensor for trace detection of Pb (II). *Journal of The Electrochemical Society*, *169*(6), 066513. https://doi.org/10.1149/1945-7111/ac77c4

Satarug, S. (2018). Dietary cadmium intake and its effects on kidneys. *Toxics*, *6*(1), Article 1. https://doi.org/10.3390/toxics6010015

Saturnino, C., Iacopetta, D., Sinicropi, M. S., Rosano, C., Caruso, A., Caporale, A., Marra, N., Marengo, B., Pronzato, M. A., Parisi, O. I., Longo, P., & Ricciarelli, R. (2014). N-Alkyl carbazole derivatives as new tools for alzheimer's disease: Preliminary studies. *Molecules*, *19*(7), Article 7. https://doi.org/10.3390/molecules19079307

Shakkthivel, P., & Singh, P. (2007). Role of PtO on the oxidation of arsenic (III) at Pt RDE in 1M H_2SO_4 and 1M Na_2SO_4 through linear sweep voltammetry technique. *International Journal of Electrochemical Science*, *2*(4), 311–320. https://doi.org/10.1016/S1452-3981(23)17076-3

Shi, G., Li, Y., Liu, Y., & Wu, L. (2023). Predicting the speciation of ionizable antibiotic ciprofloxacin by biochars with varying carbonization degrees. *RSC Advances*, *13*(15), 9892–9902. https://doi.org/10.1039/D3RA00122A

Shi, J., & Cai, Y. (2020). Environmental chemistry and toxicology of heavy metals. *Ecotoxicology and Environmental Safety*, *202*, 110926. https://doi.org/10.1016/j.ecoenv.2020.110926

Shu, Z., Zou, Y., Wu, X., Zhang, Q., Shen, Y., Xiao, A., Duan, S., Pi, F., Liu, X., Wang, J., & Dai, H. (2023). NH_2-MIL-125(Ti)/reduced graphene oxide enhanced electrochemical detection of fenitrothion in agricultural products. *Foods*, *12*(7), Article 7. https://doi.org/10.3390/foods12071534

Škoda, D., Kazda, T., Munster, L., Hanuliková, B., Stýskalík, A., Eloy, P., Debecker, D., Vyroubal, P., Šimoníková, L., & Kuřitka, I. (2019). Microwave-assisted synthesis of a manganese metal-organic framework and its transformation to porous MnO/carbon nanocomposite utilized as a shuttle suppressing layer in lithium-sulfur batteries. *54*(22). https://www.muni.cz/en/research/publications/1627837

Sohrabi, H., Ghasemzadeh, S., Ghoreishi, Z., Majidi, M. R., Yoon, Y., Dizge, N., & Khataee, A. (2023). Metal-organic frameworks (MOF)-based sensors for detection of toxic gases: A review of current status and future prospects. *Materials Chemistry and Physics*, *299*, 127512. https://doi.org/10.1016/j.matchemphys.2023.127512

Solís, R. R., Gómez-Avilés, A., Belver, C., Rodriguez, J. J., & Bedia, J. (2021). Microwave-assisted synthesis of NH_2-MIL-125(Ti) for the solar photocatalytic degradation of aqueous emerging pollutants in batch and continuous tests. *Journal of Environmental Chemical Engineering*, *9*(5), 106230. https://doi.org/10.1016/j.jece.2021.106230

Solís, R. R., Peñas-Garzón, M., Belver, C., Rodriguez, J. J., & Bedia, J. (2022). Highly stable UiO-66-NH_2 by the microwave-assisted synthesis for solar photocatalytic water treatment. *Journal of Environmental Chemical Engineering*, *10*(2), 107122. https://doi.org/10.1016/j.jece.2021.107122

Song, L., Xue, C., Xia, H., Qiu, S., Sun, L., & Chen, H. (2019). Effects of alkali metal (Li, Na, and K) incorporation in NH_2–MIL125(Ti) on the performance of CO_2 adsorption. *Materials*, *12*(6), Article 6. https://doi.org/10.3390/ma12060844

Sörengård, M., Campos-Pereira, H., Ullberg, M., Lai, F. Y., Golovko, O., & Ahrens, L. (2019). Mass loads, source apportionment, and risk estimation of organic

micropollutants from hospital and municipal wastewater in recipient catchments. *Chemosphere*, *234*, 931–941. https://doi.org/10.1016/j.chemosphere.2019.06.041

States, J. C., Srivastava, S., Chen, Y., & Barchowsky, A. (2008). Arsenic and cardiovascular disease. *Toxicological Sciences*, *107*(2), 312. https://doi.org/10.1093/toxsci/kfn236

Stentiford, G. D., Peeler, E. J., Tyler, C. R., Bickley, L. K., Holt, C. C., Bass, D., Turner, A. D., Baker-Austin, C., Ellis, T., Lowther, J. A., Posen, P. E., Bateman, K. S., Verner-Jeffreys, D. W., van Aerle, R., Stone, D. M., Paley, R., Trent, A., Katsiadaki, I., Higman, W. A., … Hartnell, R. E. (2022). A seafood risk tool for assessing and mitigating chemical and pathogen hazards in the aquaculture supply chain. *Nature Food*, *3*(2), Article 2. https://doi.org/10.1038/s43016-022-00465-3

Sun, X., Hu, D., Yang, L., Wang, N., Wang, Y.-G., & Ouyang, X. (2019). Efficient adsorption of Levofloxacin from aqueous solution using calcium alginate/metal organic frameworks composite beads. *Journal of Sol-Gel Science and Technology*, *91*(2), 353–363. https://doi.org/10.1007/s10971-019-05001-7

Tajik, S., Beitollahi, H., Zaeimbashi, R., Sheikhshoaei, M., Askari, M. B., & Salarizadeh, P. (2021). An electrochemical sensor based on V_2O_5 nanoparticles for the detection of ciprofloxacin. *Journal of Materials Science: Materials in Electronics*, *32*(13), 17558–17567. https://doi.org/10.1007/s10854-021-06288-5

Tan, Y., Guo, Y., Gu, X., & Gu, C. (2015). Effects of metal cations and fulvic acid on the adsorption of ciprofloxacin onto goethite. *Environmental Science and Pollution Research*, *22*(1), 609–617. https://doi.org/10.1007/s11356-014-3351-4

Tang, Q., Zhu, G., Ge, Y., Yang, J., Huang, M., & Liu, J. (2020). AuNPs-polyaniline nanosheet array on carbon nanofiber for the determination of As(III). *Journal of Electroanalytical Chemistry*, *873*, 114381. https://doi.org/10.1016/j.jelechem.2020.114381

Tarahomi, S., Rounaghi, G. H., Zavar, M. H. A., & Daneshvar, L. (2018). Electrochemical sensor based on TiO_2 nanoparticles/nafion biocompatible film modified glassy carbon electrode for carbamazepine determination in pharmaceutical and urine samples. *Journal of The Electrochemical Society*, *165*(16), B946. https://doi.org/10.1149/2.1061816jes

Tellez-Plaza, M., Jones, M. R., Dominguez-Lucas, A., Guallar, E., & Navas-Acien, A. (2013). Cadmium exposure and clinical cardiovascular disease: A systematic review. *Current Atherosclerosis Reports*, *15*(10), 10.1007/s11883. https://doi.org/10.1007/s11883-013-0356-2

Thiruppathi, M., Natarajan, T., & Zen, J.-M. (2023). Electrochemical detection of fluoride ions using 4-aminophenyl boronic acid dimer modified electrode. *Journal of Electroanalytical Chemistry*, *944*, 117685. https://doi.org/10.1016/j.jelechem.2023.117685

Thompson, L. J. (2012). Chapter 37—Lead. In R. C. Gupta (Ed.), *Veterinary Toxicology (Second Edition)* (pp. 522–526). Academic Press. https://doi.org/10.1016/B978-0-12-385926-6.00037-5

Tinkov, A. A., Filippini, T., Ajsuvakova, O. P., Skalnaya, M. G., Aaseth, J., Bjørklund, G., Gatiatulina, E. R., Popova, E. V., Nemereshina, O. N., Huang, P.-T., Vinceti, M., & Skalny, A. V. (2018). Cadmium and atherosclerosis: A review of toxicological mechanisms and a meta-analysis of epidemiologic studies. *Environmental Research*, *162*, 240–260. https://doi.org/10.1016/j.envres.2018.01.008

Tiwari, D., Jamsheera, A., Zirlianngura, & Lee, S. M. (2017). Use of hybrid materials in the trace determination of As(V) from aqueous solutions: An electrochemical study. *Environmental Engineering Research*, *22*(2), 186–192. https://doi.org/10.4491/eer.2016.045

Vaitsis, C., Kanellou, E., Pandis, P. K., Papamichael, I., Sourkouni, G., Zorpas, A. A., & Argirusis, C. (2022). Sonochemical synthesis of zinc adipate Metal-Organic Framework (MOF) for the electrochemical reduction of CO_2: MOF and circular economy potential. *Sustainable Chemistry and Pharmacy*, *29*, 100786. https://doi.org/10.1016/j.scp.2022.100786

Valenzano, L., Civalleri, B., Chavan, S., Bordiga, S., Nilsen, M. H., Jakobsen, S., Lillerud, K. P., & Lamberti, C. (2011). Disclosing the complex structure of UiO-66 metal organic framework: A synergic combination of experiment and theory. *Chemistry of Materials*, *23*(7), 1700–1718. https://doi.org/10.1021/cm1022882

Vedhavathi, H. S., Sanjay, B. P., Basavaraju, M., Madhukar, B. S., & Swamy, N. K. (2022). Development of ciprofloxacin sensor using iron-doped graphitic carbon nitride as transducer matrix: Analysis of ciprofloxacin in blood samples: Original scientific paper. *Journal of Electrochemical Science and Engineering*, *12*(1), Article 1. https://doi.org/10.5599/jese.1112

Vedhi, C., Selvanathan, G., Arumugam, P., & Manisankar, P. (2009). Electrochemical sensors of heavy metals using novel polymer-modified glassy carbon electrodes. *Ionics*, *15*(3), 377–383. https://doi.org/10.1007/s11581-008-0277-1

Viegas, R. M. A., Melo, M. L., Brandão Lima, L. C., Garcia, R. R. P., Filho, E. C. S., Osajima, J. A., & Chiavone-Filho, O. (2024). Carbamazepine adsorption with a series of organoclays: Removal and toxicity analyses. *Applied Water Science*, *14*(6), 133. https://doi.org/10.1007/s13201-024-02198-z

Vinoth, V., Wu, J. J., Asiri, A. M., & Anandan, S. (2017). Sonochemical synthesis of silver nanoparticles anchored reduced graphene oxide nanosheets for selective and sensitive detection of glutathione. *Ultrasonics Sonochemistry*, *39*, 363–373. https://doi.org/10.1016/j.ultsonch.2017.04.035

Vu, H. D., Nguyen, L.-H., Nguyen, T. D., Nguyen, H. B., Nguyen, T. L., & Tran, D. L. (2015). Anodic stripping voltammetric determination of Cd^{2+} and Pb^{2+} using interpenetrated MWCNT/P1,5-DAN as an enhanced sensing interface. *Ionics*, *21*(2), 571–578. https://doi.org/10.1007/s11581-014-1199-8

Wang, M., Yang, L., Hu, B., Liu, Y., Song, Y., He, L., Zhang, Z., & Fang, S. (2018). A novel electrochemical sensor based on Cu3P@NH_2-MIL-125(Ti) nanocomposite for efficient electrocatalytic oxidation and sensitive detection of hydrazine. *Applied Surface Science*, *445*, 123–132. https://doi.org/10.1016/j.apsusc.2018.03.144

Wang, W., Bao, N., Yuan, W., Si, N., Bai, H., Li, H., & Zhang, Q. (2019). Simultaneous determination of lead, arsenic, and mercury in cosmetics using a plastic based disposable electrochemical sensor. *Microchemical Journal*, *148*, 240–247. https://doi.org/10.1016/j.microc.2019.05.011

Wang, Z., Li, L., & Liu, E. (2013). Graphene ultrathin film electrodes modified with bismuth nanoparticles and polyaniline porous layers for detection of lead and cadmium ions in acetate buffer solutions. *Thin Solid Films*, *544*, 362–367. https://doi.org/10.1016/j.tsf.2013.02.098

Wang, Z., Liu, E., & Zhao, X. (2011). Glassy carbon electrode modified by conductive polyaniline coating for determination of trace lead and cadmium ions in acetate buffer solution. *Thin Solid Films*, *519*(15), 5285–5289. https://doi.org/10.1016/j.tsf.2011.01.176

Werber, J. R., Osuji, C. O., & Elimelech, M. (2016). Materials for next-generation desalination and water purification membranes. *Nature Reviews Materials*, *1*(5), Article 5. https://doi.org/10.1038/natrevmats.2016.18

Wu, Q., Zhou, X., Li, P., You, S., Ye, J., Bao, P., Chen, X., Tong, H., & Wang, S. (2023). Non-enzymatic electrochemical sensor based on Pt/$MoSe_2$ nanomesh for the detection of hydrogen peroxide. *Materials Chemistry and Physics*, *310*, 128496. https://doi.org/10.1016/j.matchemphys.2023.128496

Wu, Y., Wang, S., Ni, Z., Li, H., May, L., & Pu, J. (2021). Emerging water pollution in the world's least disturbed lakes on Qinghai-Tibetan Plateau. *Environmental Pollution*, *272*, 116032. https://doi.org/10.1016/j.envpol.2020.116032

Xiao, J.-D., Qiu, L.-G., Ke, F., Yuan, Y.-P., Xu, G.-S., Wang, Y.-M., & Jiang, X. (2013). Rapid synthesis of nanoscale terbium-based metal–organic frameworks by a combined ultrasound-vapour phase diffusion method for highly selective sensing of picric acid. *Journal of Materials Chemistry A*, *1*(31), 8745–8752. https://doi.org/10.1039/C3TA11517H

Xiao, P., Zhu, G., Shang, X., Hu, B., Zhang, B., Tang, Z., Yang, J., & Liu, J. (2022). An Fe-MOF/MXene-based ultra-sensitive electrochemical sensor for arsenic(III) measurement. *Journal of Electroanalytical Chemistry*, *916*, 116382. https://doi.org/10.1016/j.jelechem.2022.116382

Xin, J., Yan, S., Hong, X., Zhang, H., & Zha, J. (2021). Environmentally relevant concentrations of carbamazepine induced lipid metabolism disorder of Chinese rare minnow (*Gobiocypris rarus*) in a gender-specific pattern. *Chemosphere*, *265*, 129080. https://doi.org/10.1016/j.chemosphere.2020.129080

Xu, S., Hu, S., Zhu, L., & Wang, W. (2021). Haloquinone chloroimides as toxic disinfection byproducts identified in drinking water. *Environmental Science & Technology*, *55*(24), 16347–16357. https://doi.org/10.1021/acs.est.1c01690

Xu, X., Liu, Y., Wang, T., Ji, H., Chen, L., Li, S., & Liu, W. (2019). Co-adsorption of ciprofloxacin and Cu(II) onto titanate nanotubes: Speciation variation and metal-organic complexation. *Journal of Molecular Liquids*, *292*, 111375. https://doi.org/10.1016/j.molliq.2019.111375

Yadav, D. K., Ganesan, V., Sonkar, P. K., Gupta, R., & Rastogi, P. K. (2016). Electrochemical investigation of gold nanoparticles incorporated zinc based metal-organic framework for selective recognition of nitrite and nitrobenzene. *Electrochimica Acta*, *200*, 276–282. https://doi.org/10.1016/j.electacta.2016.03.092

Yaghi, O. M., & Li, H. (1995). Hydrothermal synthesis of a metal-organic framework containing large rectangular channels. *Journal of the American Chemical Society*, *117*(41), 10401–10402. https://doi.org/10.1021/ja00146a033

Yang, D., & Gates, B. C. (2024). Characterization, structure, and reactivity of hydroxyl groups on metal-oxide cluster nodes of metal–organic frameworks: Structural diversity and keys to reactivity and catalysis. *Advanced Materials*, *36*(5), 2305611. https://doi.org/10.1002/adma.202305611

Yang, L., Xu, C., Ye, W., & Liu, W. (2015). An electrochemical sensor for H_2O_2 based on a new Co-metal-organic framework modified electrode. *Sensors and Actuators B: Chemical*, *215*, 489–496. https://doi.org/10.1016/j.snb.2015.03.104

Yang, Q., Zhang, H.-Y., Wang, L., Zhang, Y., & Zhao, J. (2018). Ru/UiO-66 catalyst for the reduction of nitroarenes and tandem reaction of alcohol oxidation/knoevenagel condensation. *ACS Omega*, *3*(4), 4199–4212. https://doi.org/10.1021/acsomega.8b00157

Yang, S., Chen, S., Li, K., Luo, Q., Zhang, Y., Wang, L., Wu, S., & Zhu, M. (2023). A water-stable metal–organic framework Zn-MOF as a chemical sensor for efficient detection of Cr(VI) (Cr_2O72- and CrO42-) anions in water. *Inorganica Chimica Acta*, *558*, 121764. https://doi.org/10.1016/j.ica.2023.121764

Yang, X., Chen, Z., Zhao, W., Liu, C., Qian, X., Zhang, M., Wei, G., Khan, E., Hau Ng, Y., & Sik Ok, Y. (2021). Recent advances in photodegradation of antibiotic residues in water. *Chemical Engineering Journal*, *405*, 126806. https://doi.org/10.1016/j.cej.2020.126806

Yang, Y., Huang, W., Guo, Z., Zhang, S., Wu, F., Huang, J., Yang, H., Zhou, Y., Xu, W., & Gu, S. (2019). Robust fluorine-free colorful superhydrophobic PDMS/NH2-MIL-125(Ti)@cotton fabrics for improved ultraviolet resistance and efficient oil–water separation. *Cellulose*, *26*(17), 9335–9348. https://doi.org/10.1007/s10570-019-02707-3

Yang, Z., Tong, X., Feng, J., He, S., Fu, M., Niu, X., Zhang, T., Liang, H., Ding, A., & Feng, X. (2019). Flower-like BiOBr/UiO-66-NH_2 nanosphere with improved photocatalytic property for norfloxacin removal. *Chemosphere*, *220*, 98–106. https://doi.org/10.1016/j.chemosphere.2018.12.086

Yaou Balarabe, B. (2023). Green synthesis of gold-titania nanoparticles for sustainable ciprofloxacin removal and phytotoxicity evaluation on aquatic plant growth. *Hybrid Advances*, *4*, 100107. https://doi.org/10.1016/j.hybadv.2023.100107

Yin, H., Zhu, J., Chen, J., Gong, J., & Nie, Q. (2018). MOF-derived in situ growth of carbon nanotubes entangled Ni/NiO porous polyhedrons for high performance glucose sensor. *Materials Letters*, *221*, 267–270. https://doi.org/10.1016/j.matlet.2018.03.156

Yoosefian, M., Ahmadzadeh, S., Aghasi, M., & Dolatabadi, M. (2017). Optimization of electrocoagulation process for efficient removal of ciprofloxacin antibiotic using iron electrode; kinetic and isotherm studies of adsorption. *Journal of Molecular Liquids*, *225*, 544–553. https://doi.org/10.1016/j.molliq.2016.11.093

Yousefi, M., Ghoochani, M., & Hossein Mahvi, A. (2018). Health risk assessment to fluoride in drinking water of rural residents living in the Poldasht city,

Northwest of Iran. *Ecotoxicology and Environmental Safety*, *148*, 426–430. https://doi.org/10.1016/j.ecoenv.2017.10.057

Yu, K., Lee, Y.-R., Seo, J. Y., Baek, K.-Y., Chung, Y.-M., & Ahn, W.-S. (2021). Sonochemical synthesis of Zr-based porphyrinic MOF-525 and MOF-545: Enhancement in catalytic and adsorption properties. *Microporous and Mesoporous Materials*, *316*, 110985. https://doi.org/10.1016/j.micromeso.2021.110985

Yu, Y., Chen, D., Xie, S., Sun, Q., Zhang, Z.-X., & Zeng, G. (2022). Adsorption behavior of carbamazepine on Zn-MOFs derived nanoporous carbons: Defect enhancement, role of N doping and adsorption mechanism. *Journal of Environmental Chemical Engineering*, *10*(3), 107660. https://doi.org/10.1016/j.jece.2022.107660

Yuan, S., Qin, J.-S., Lollar, C. T., & Zhou, H.-C. (2018). Stable metal–organic frameworks with group 4 metals: Current status and trends. *ACS Central Science*, *4*(4), 440–450. https://doi.org/10.1021/acscentsci.8b00073

Yuan, Y., Zhang, F., Wang, H., Gao, L., & Wang, Z. (2018). A sensor based on au nanoparticles/carbon nitride/graphene composites for the detection of chloramphenicol and ciprofloxacin. *ECS Journal of Solid State Science and Technology*, *7*(12), M201. https://doi.org/10.1149/2.0111812jss

Yusof, N. F., Raffi, A. A., Yahaya, N. Z. S., Abas, K. H., Othman, M. H. D., Jaafar, J., & Rahman, M. A. (2023). Surface modification of UiO-66 on hollow fibre membrane for membrane distillation. *Membranes*, *13*(3), Article 3. https://doi.org/10.3390/membranes13030253

Zhang, H., Hu, X., Li, T., Zhang, Y., Xu, H., Sun, Y., Gu, X., Gu, C., Luo, J., & Gao, B. (2022). MIL series of metal organic frameworks (MOFs) as novel adsorbents for heavy metals in water: A review. *Journal of Hazardous Materials*, *429*, 128271. https://doi.org/10.1016/j.jhazmat.2022.128271

Zhang, H., Li, Y., Zhang, Y., Wu, J., Hu, J., Li, S., & Li, L. (2023). Simultaneous detection of lead and cadmium based on N-doped MoS_2/MWCNTs nanocomposites. *Journal of Materials Science*, *58*(15), 6643–6655. https://doi.org/10.1007/s10853-023-08424-4

Zhang, H., Nai, J., Yu, L., & Lou, X. W. (David). (2017). Metal-organic-framework-based materials as platforms for renewable energy and environmental applications. *Joule*, *1*(1), 77–107. https://doi.org/10.1016/j.joule.2017.08.008

Zhang, L., Li, S., Xin, J., Ma, H., Pang, H., Tan, L., & Wang, X. (2018). A non-enzymatic voltammetric xanthine sensor based on the use of platinum nanoparticles loaded with a metal-organic framework of type MIL-101(Cr). Application to simultaneous detection of dopamine, uric acid, xanthine and hypoxanthine. *Microchimica Acta*, *186*(1), 9. https://doi.org/10.1007/s00604-018-3128-4

Zhang, L., Wang, Y., Tong, L., & Xia, Y. (2014). Synthesis of colloidal metal nanocrystals in droplet reactors: The pros and cons of interfacial adsorption. *Nano Letters*, *14*(7), 4189–4194. https://doi.org/10.1021/nl501994q

Zhang, S., Fu, H., Liu, H., Wang, S., Yu, K., Chen, Z., Zhang, M., & Wang, L. (2023). Synergetic catalysis of ligand connecting MOFs@MOFs composites in electrochemical detection of P-Chlorophenols. *Microporous and Mesoporous Materials*, *360*, 112726. https://doi.org/10.1016/j.micromeso.2023.112726

Zhang, S., & Huang, W. (2001). Simultaneous determination of Cd^{2+} and Pb^{2+} using a chemically modified electrode. *Analytical Sciences: The International Journal of the Japan Society for Analytical Chemistry*, *17*(8), 983–985. https://doi.org/10.2116/analsci.17.983

Zhang, W., Liu, Y., Lu, G., Wang, Y., Li, S., Cui, C., Wu, J., Xu, Z., Tian, D., Huang, W., DuCheneu, J. S., Wei, W. D., Chen, H., Yang, Y., & Huo, F. (2015). Mesoporous metal–organic frameworks with size-, shape-, and space-distribution-controlled pore structure. *Advanced Materials*, *27*(18), 2923–2929. https://doi.org/10.1002/adma.201405752

Zhao, J., Huang, P., & Jin, W. (2021). Electrochemical sensor based on TiO_2/polyvinyl alcohol nanocomposite for detection of ciprofloxacin in rainwater. *International Journal of Electrochemical Science*, *16*(10), 211018. https://doi.org/10.20964/2021.10.01

Zheng, L., Sun, L., Qiu, J., Song, J., Zou, L., Teng, Y., Zong, Y., & Yu, H. (2024). Using NH2-MIL-125(Ti) for efficient removal of Cr(VI) and RhB from aqueous solutions: Competitive and cooperative behavior in the binary system.

Journal of Environmental Sciences, *136*, 437–450. https://doi.org/10.1016/j.jes.2023.02.013

Zhou, R., Zhuang, X., Wu, Q., Jin, M., Zheng, C., Jiang, Y., Lou, Y., & Zheng, L. (2022). Cu-MOF@Pt 3D nanocomposites prepared by one-step wrapping method with peroxidase-like activity for colorimetric detection of glucose. *Colloids and Surfaces B: Biointerfaces*, *216*, 112601. https://doi.org/10.1016/j.colsurfb.2022.112601

Zirlianngura, Tiwari, D., Ha, J.-H., & Lee, S.-M. (2017). Efficient use of porous hybrid materials in a selective detection of lead(II) from aqueous solutions: An electrochemical study. *Metals*, *7*(4), Article 4. https://doi.org/10.3390/met7040124

BIO-DATA

1. **NAME** : Ricky Lalawmpuia
2. **DATE OF BIRTH** : 10th November, 1991.
3. **FATHER'S NAME** : Zonunthara Kawlni
4. **PERMANENT ADDRESS** : Hmarveng, Kolasib – 796081
5. **EDUCATIONAL QUALIFICATIONS** : M.Sc. (Chemistry)

Qualification	**Year of Passing**	**Board/University**	**Subjects**	**% Of Marks**	**Div.**
HSLC	2008	Mizoram Board of School Education (MBSE)	Mathematics, Science, Social Science, English, Mizo	71.8	First
HSSLC	2010	Mizoram Board of School Education (MBSE)	Physic, Chemistry, Mathematics, English, Computer science	60	First
B.Sc. (Chemistry)	2016	Mizoram University	Chemistry	75.16	First
M.Sc. (Chemistry)	2018	Mizoram University	Physical Chemistry (Specialisation)	74	First

LIST OF PUBLICATIONS

A. Journals (Published)

1. **Ricky Lalawmpuia**, Melody Lalhruaitluangi, Lalhmunsiama, and Diwakar Tiwari. (2024). Metal Organic Framework (MOF): Synthesis and Fabrication for the Application of Electrochemical Sensing. ***Environmental Engineering Research,*** 29(5).

2. Sarikokba, Lalhmunsiama, **Ricky Lalawmpuia**, Diwakar Tiwari, and Dong-Jin Kim. (2023). Thin Film Electrode for Trace and Efficient Detection of Triclosan: Stability of Electrode and Real Matrix Analyses. ***Water, Air, & Soil Pollution,*** 234(7):423.
3. **Ricky Lalawmpuia**, Melody Lalhruaitluangi, Lalhmunsiama, Suk Soon Choi, Diwakar Tiwari (2025). Novel titanium-based metal organic framework (MOF) in efficient and ultra-trace electrochemical detection of arsenic (III). ***Journal of Applied Electrochemistry,*** https://doi.org/10.1007/s10800-025-02314-0.
4. **Ricky Lalawmpuia**, Melody Lalhruaitluangi, Diwakar Tiwari, Rama Dubey (2025). Nanocomposite material in the trace and simultaneouselectrochemical detection of As(III) and As(V). ***Environmental Engineering Research,*** 30(5):240663.

B. Journals (Communicated)

1. **Ricky Lalawmpuia**, Melody Lalhruaitluangi, Lalhmunsiama, Suk Soon Choi, Diwakar Tiwari. Highly sensitive Titanium based Metal Organic Framework for the simultaneous detection of Lead (II) and Cadmium (II) in aqueous media. ***Analytical and Bioanalytical Research (Communicated).***
2. **Ricky Lalawmpuia**, Lalhmunsiama, Diwakar Tiwari. Electrochemical sensor based on zirconium metal organic framework for the detection of ciprofloxacin and carbamazepine. ***Microchemical Journal (Communicated).***

CONFERENCES AND SEMINAR

1. **Ricky Lalawmpuia** and Diwakar Tiwari. Development of highly sensitive Zirconium based metal organic framework (MOF) sensor for the electrochemical detection of ciprofloxacin. International Conference on Recent Advance in mathematical, physical and chemical sciences (ICRAMPC-2024) during 21st – 23rd February, 2024, organised by the school of physical science, Mizoram University, Aizawl, India.
2. **Ricky Lalawmpuia** and Diwakar Tiwari. Heterogenous photocatalysis degradation of sulfamethoxazole. International Conference on Chemistry & environmental sustainability (ICCES) during 19th – 22nd February 2019, organized by Department of chemistry, Mizoram University, Aizawl, India.
3. **Ricky Lalawmpuia** and Diwakar Tiwari. Synthesis of metal organic framework (MOF): Use of MOF in the trace electrochemical detection of cadmium (II). International Conference on Science and technology for innovative and sustainable development (STISD) during 28th – 30th June 2023, organised by Department of chemistry and Department of Industrial chemistry, Mizoram University, Aizawl, India.
4. **Ricky Lalawmpuia** and Diwakar Tiwari. Synthesis of metal organic framework (MOF): Use of MOF in the trace electrochemical detection of arsenic (III). National Conference, at the physical science discipline in the 4th Mizoram science congress held at Aijal club during 24th – 25th November, 2022, Organised by Mizoram Science, technology and innovative council (MISTIC).
5. **Ricky Lalawmpuia** and Diwakar Tiwari. Electrochemical detection of Ciprofloxacin using highly sensitive Zirconium based Metal organic framework (MOF). National Conference on Chemical Physics (NCCP) during 18th – 19th March, 2024, organized by Department of Physics, Assam University, Assam, India.
6. **Ricky Lalawmpuia** and Diwakar Tiwari. Highly sensitive titanium-based MOF in the trace detection of lead (II) in aqueous media. National Conference on Functional Materials and Applications (NCFMA - 2019), Organised by Department of BS and HSS (Physic), National Institute of Technology Mizoram, Aizawl, Mizoram, India-796012, during 22nd – 23rd November, 2019.

PARTICULARS OF THE CANDIDATE

NAME OF CANDIDATE	**:** Ricky Lalawmpuia
DEGREE	**:** Doctor of Philosophy (Ph.D.)
DEPARTMENT	**:** Chemistry
TITLE OF THESIS	**:** Synthesis of Metal Organic Framework (MOF) in selective sensor development for trace detection of arsenic and some micropollutants
DATE OF ADMISSION	**:** 9th August, 2018
APPROVAL OF RESEARCH PROPOSAL:	
1. DRC	**:**16th April 2019
2. BOS	**:** 23rd April 2019
3. SCHOOL BOARD	**:** 8th May 2019
4. MZU REGN. NO.	**:** 4645 of 2013
5. Ph.D. REGISTRATION NO.& DATE	**:** MZU/Ph.D./1247of 09.08.2018
6. EXTENSION	**:** No. 12-4/MZU(Acad)/23/209 Dated. 23rd July, 2024

Head

Department of Chemistry

ABSTRACT

SYNTHESIS OF METAL ORGANIC FRAMEWORK (MOF) IN SELECTIVE SENSOR DEVELOPMENT FOR TRACE DETECTION OF ARSENIC AND SOME MICROPOLLUTANTS

AN ABSTRACT SUBMITTED IN PARTIAL FULFILMENT OF THE REQUIREMENTS FOR THE DEGREE OF DOCTOR OF PHILOSOPHY

RICKY LALAWMPUIA

MZU REGISTRATION NUMBER: 4645 of 2013

Ph.D. REGISTRATION NUMBER: MZU/Ph.D./1247 of 09.08.2018

DEPARTMENT OF CHEMISTRY

SCHOOL OF PHYSICAL SCIENCES

JANUARY, 2025

SYNTHESIS OF METAL ORGANIC FRAMEWORK (MOF) IN SELECTIVE SENSOR DEVELOPMENT FOR TRACE DETECTION OF ARSENIC AND SOME MICROPOLLUTANTS

BY

RICKY LALAWMPUIA

Department of Chemistry

Under the supervision of

Prof. DIWAKAR TIWARI

Submitted
In partial fulfilment of the requirement of the Degree of Doctor of Philosophy in Chemistry of Mizoram University, Aizawl

ABSTRACT

Water is the most essential natural resource on Earth. Nevertheless, the water resources are mistreated and unethically handled. In the recent past, the number of hazardous wastes dumped in aquatic environments and contaminating the water bodies significantly. Data published by the World Water Assessment Program (WWAP) reported that every year, millions of tonnes of heavy metals, solvents, toxic sludge, and pharmaceutical residues are dumped into aquatic environments by industry, and municipal wastes, which are either untreated or partially treated. This signifies human activities are undoubtedly the primary source of water pollution. The contamination of water causes widespread infectious disease transmission including cholera, severe diarrhea, legionellosis, and typhoid fever. Worldwide, 6.1% of all health-related fatalities are attributable to avoidable diarrheal diseases resulting from contaminated water and insufficient sanitation and hygiene.

In certain regions of India, groundwater is severely contaminated with highly toxic arsenic. Prolonged exposure to arsenic is linked to various forms of cancer, including skin, lung, bladder, and kidney cancers. Additionally, the ingestion of arsenic through drinking water heightens the risk of cardiovascular diseases. Additionally, lead is another hazardous element that poses significant health risks, particularly in children, as lead poisoning can severely damage the nervous system. Exposure to lead also adversely affects kidney function and elevates blood pressure, contributing to cardiovascular issues. India has encountered significant challenges related to lead contamination, primarily due to industrial emissions, the use of lead-based paints, and the improper recycling of lead-acid batteries. Cadmium is recognized for its tendency to accumulate in the kidneys over time, leading to significant damage and the potential development of kidney disease. Cadmium contamination is frequently linked to industrial discharges and poor waste management practices. Additionally, micro-pollutants have emerged as significant contaminants, raising serious environmental concerns. These micro-pollutants are only partially degraded in conventional wastewater treatment plants (WWTP), with residues escaping into the aquatic environment. Consequently, micropollutant levels in freshwater are detected in the range of µg/L to ng/L. Ciprofloxacin, an antibiotic from the fluoroquinolone

class, poses environmental and health risks due to its presence in water bodies. The presence of ciprofloxacin in aquatic ecosystems threatens non-target organisms and disrupts ecological balance. Furthermore, carbamazepine, a pharmaceutical used for treating epilepsy, bipolar disorder, and certain nerve pain conditions, is toxic to aquatic life, including fish, algae, and invertebrates, adversely affecting their physiological processes, growth, and reproductive systems. It is imperative to monitor these contaminants at low levels to protect both human health and aquatic organisms. Despite the effectiveness of advanced analytical tools in detecting these contaminants, their offsite operation and the substantial costs of the instruments limit their extensive use. On the other hand, electrochemical methods are beneficial for creating miniaturized devices that enable onsite detection of various contaminants in aqueous environments. Furthermore, employing advanced materials in the fabrication of microelectrodes enhances the efficiency and specificity of contaminant detection in aquatic ecosystems.

Metal-organic frameworks (MOFs) represent a fascinating class of crystalline materials and received greater interest during the past couple of decades. These materials are composed of metal ions or clusters coordinated with organic ligands, forming highly porous and often tuneable structures. Their potential for addressing global challenges in energy, environment, and technology underscores the significance of MOFs in diverse areas. Metal-organic frameworks (MOFs) have emerged as a highly versatile and promising class of materials for sensing applications. These hybrid crystalline structures are constructed from metal ions or clusters coordinated to organic ligands, forming porous networks with remarkable tunability and high surface areas. Among the various MOFs, titanium-based MOFs (Ti-MOFs) have garnered significant attention due to their high stability, biocompatibility, and photocatalytic abilities. These characteristics make Ti-MOFs promising in wider applications, including sensing. Similarly, zirconium-based MOFs (Zr-MOFs) showed unique chemical and physical properties and useful materials in detecting a wide range of analytes, including gases, organic compounds, and biomolecules. Zirconium-based MOFs are composed of zirconium clusters coordinated with organic linkers, forming highly stable crystalline frameworks. The stability of Zr-MOFs under various conditions,

including high temperatures and acidic or basic environments, sets them apart from other MOFs. Additionally, Zr-MOFs exhibit high chemical tunability, enabling precise control over pore size, functional groups, and electronic properties. These characteristics are essential for designing sensors with high sensitivity and selectivity.

Titanium-MOF is a hydrothermally synthesized precursor to the amino-1,4-benzene dicarboxylic acid (NH_2BDC) and titanium (IV) butoxide. The precursors to benzene-1,4-dicarboxylic acid (BDC) and zirconium chloride ($ZrCl_4$) are used in the hydrothermal synthesis of zirconium metal-organic framework (Zr-MOF). These materials are extensively characterized by several advanced analytical tools viz., XRD, TGA, AFM, BET, XPS, FE-SEM, and HR-TEM. The MOFs are utilized in the fabrication of the thin film glassy carbon electrode. Additionally, it was utilized in the electrochemical detection of toxic heavy metal ions such as arsenic (As(III)), cadmium (Cd(II)), lead (Pb(II)) along with selected micropollutants such as carbamazepine (CBZ) and ciprofloxacin (CFX) by the utilization of differential pulse anodic stripping voltammetry (DPASV). Studies utilizing cyclic voltammetry (CV) and electrochemical impedance spectroscopy (EIS) characterize the electrochemically thin film electrodes.

An Atomic Force Microscope (AFM) accurately measures the topography of a thin film surface. The average roughness (R_a) of the bare glassy carbon sheet, Ti-MOF and Zr-MOF coated thin film glassy carbon plates was 1.18 nm. 8.03 nm and 22.44 nm, respectively. The results clearly show that the MOF-coated carbon plate possesses significantly higher surface roughness compared to the bare carbon plate.

The SEM images of the bare carbon sheet possess a very smooth surface structure while the SEM images of the Ti-MOF and Zr-MOF coated glassy carbon plates show heterogeneous surface structure. The EDX spectra reveal that Ti-MOF shows very distinct peaks of Ti, C, N, and O elements having atomic percentages of 6.81, 60.21, 10.22, and 22.76, respectively. Similarly, the Zr-MOF shows the EDX peaks of Zr, C, and O with atomic percentages of 3.42, 66.62, and 29.96, respectively. These results show that the Ti-MOF and Zr-MOF contain significant contents of Ti and Zr elements, respectively, possibly with their oxide forms. TEM images of Ti-MOF and Zr-MOF solids show that the particles are distinctly dispersed within the

solid. Further, the TEM images show the fringes of the nanoparticles, and Gatan Digital micrograph (GDM) was utilized to obtain the d-spacings of the Ti-MOF and Zr-MOF and are found to be 0.86 nm and 0.28 nm, respectively. These d spacings refer to the (110) lattice of TiO_2 and (111) lattice plane of ZrO_2 respectively, for the Ti-MOF and Zr-MOF solids. Moreover, the Image J software quantifies the mean particle size distribution of Ti-MOF and Zr-MOF which were 6.36 nm and 5.70 nm, respectively.

X-Ray Diffraction (XRD) provides information about the crystalline structure and unit cell dimensions of these materials. The diffraction peaks at 24.71º, 36.75º, 47.49 º, 53.21º, 55.11º and 61.34º correspond to (101), (004), (200), (211), (105), and (204) plane respectively, confirms the presence of TiO_2 anatase phase (JCPDS card no. 21-1272). Similarly, the diffraction peaks of Zr-MOF occurred at 2θ values of 7.32° and 8.51° referring to the (111) and (200) crystal planes of ZrO_2, respectively (JCPDS no. 73-3458). The results indicate that the ZrO_2 possesses a face-cantered cubic lattice structure in the Zr-MOF. The N_2 adsorption-desorption isotherms showed that The Ti-MOF exhibits type (IV) isotherm having H3 hysteresis loop and the Zr-MOF exhibits type (I) isotherm having H3 hysteresis loop. The specific surface area of the Ti-MOF and Zr-MOF are 1040.83 m^2g^{-1} and 840.98 $m^2\ g^{-1}$, respectively. Moreover, the pore volume and pore diameter of Ti-MOF are 0.31 cm^3g^{-1} and 3.30 nm, respectively. Similarly, the pore volume and pore diameter of Zr-MOF are 0.21 cm^3g^{-1} and 2.42 nm, respectively. These results showed that these MOF solids possess relatively very high specific surface area which is attributed to the formation of framework with the linker molecules.

The XPS survey spectrum of Ti-MOF revealed the presence of Ti, O, C, and N elements in the Ti-MOF solid. The deconvolution spectrum of Ti shows two distinct XPS peaks at the binding energies of 458.7 and 464.4 eV, referring to the Ti $2p_{1/2}$ and Ti $2p_{3/2}$, respectively, of the Ti(IV). The XPS spectra of Zr-MOF confirmed the presence of Zr, C, and O in the synthesized substance. The Zr 3d spectra exhibit two distinct peaks at 182.8 and 185.2 eV, which have been identified as Zr $3d_{5/2}$ and $3d_{3/2}$, respectively. This signifies the accomplished formation of Zr-O bonds within the metal

cluster. The TGA curve of Ti-MOF reveals that below 200^0C, the solid loses its weight *Ca.* 10%, which is due to the elimination of remaining solvent molecules (DMF) from the pores, along with the removal of surface-absorbed moisture (H_2O). A substantial reduction in weight occurs within temperatures 350^0C to 470°C, which is ascribed to the breakdown and thermal decomposition of the organic linkers that constitute the MOF structure of the solid. On the other hand, the Zr-MOF displays three stages of weight loss. The first stage of weight loss (8.34%) occurred within the temperature range of 25-100^0C, which is due to the elimination of water or solvent from the solid. Further, a weight loss of 3.8% occurred within the temperature range of 100 to 420^0C due to the elimination of DMF and the dehydroxylation of the zirconium oxo-clusters. Moreover, the 41.6% weight loss of Zr-MOF occurred at temperature *Ca.* 500^0C, which is due to the thermal decomposition of organic linker molecules.

The electrochemical characterization of these thin film electrodes and bare glassy carbon electrodes was performed using cyclic voltammetry and electrochemical impedance spectroscopy. The cyclic voltammograms were obtained by measuring the electrical current as a function of the applied voltage using a conventional redox probe consisting of a 0.002 M solution of $[Fe(CN)_6]^{3-/4-}$ in 0.1 M KCl solution at a scan rate of 100 mV/s and an excitation potential window ranging from -1.0 to 1.5 V. The higher redox peak current observed for the Ti-MOF/GCE and Zr-MOF/GCE is attributed to the enhanced electrical conductivity and the functional groups present with the MOFs. Moreover, the high specific surface area of these MOFs facilitates the sorption and oxidation-reduction of iron ions at the MOFs. The redox peak potential difference (ΔE_p) values for the bare GCE, Ti-MOF/GCE, and Zr-MOF/GCE are 0.316, 0.285, and 0.254 V, respectively. The scan rate studies showed that the electroactive surface area of Bare/GCE Ti-MOF/GCE and Zr-MOF/GCE were 8.95 x 10^{-4}, 14.55 x 10^{-4} and 18.90 x 10^{-4} mm^2 respectively. The EIS study showed that the R_{ct} values for the bare GCE is 6696 Ω while that of Ti-MOF GCE is 2198 Ω which is three times less than bare GCE and finally, the R_{ct} values for the Zr-MOF GCE is 539 Ω which is twelve times less compared to bare GCE.

The differential pulse anodic stripping voltammetry (DPASV) is employed to analyze the presence of As(III) in aqueous solutions utilizing the Ti-MOF/GCE. The optimized parameters (pH 3; deposition potential -1.2 V, and deposition period 60.0 sec) were applied in the detection of As(III) in an aqueous medium. The Ti-MOF/GCE probe records the oxidative peak currents at different concentrations of As(III) and an intense and well-defined oxidative peak of As(III) is obtained at an applied potential of -1.2 V. A linear relationship is obtained between the oxidative peak current and the corresponding As(III) concentrations for two different concentration ranges viz., 5.0 to 25.0 µg/L and 0.2 to 1.0 µg/L. The LOD and LOQ values are 0.01 and 0.03 µg/L, respectively, for the As(III) concentration range of 0.2 to 1.0 µg/L. Similarly, for the As(III) concentration range 5.0 to 25.0 µg/L the LOD and LOQ values are 0.04 and 0.15 µg/L, respectively. These values are significantly below the permissible limit of lead in drinking water established by the World Health Organization (WHO), which is 10.0 µg/L. The presence of several ions *viz.*, Ca^{2+}, Mg^{2+}, Cu^{2+}, F^{-}, Cl^{-}, and NO_3^{-} unalters significantly As(III) detection. Further, the recovery rate of As(III) in river water lies between 88.4% to 107.5%, and the Ti-MOF electrode is stable for 10 repeated detection processes. The studies infer the potential of Ti-MOF for miniaturized device development for detecting the As(III).

The identification of trace amounts of Pb(II) and Cd(II) was carried out by utilizing a Glassy Carbon Electrode (GCE) that had been modified with a Titanium Metal-Organic Framework (Ti-MOF). The cyclic voltammetry (CV) study demonstrated the irreversibility of the electrooxidation of Pb(II) and Cd(II). An investigation was conducted to examine the electrochemical characteristics of Pb(II) and Cd(II) on a bare glassy carbon electrode (GCE) as well as a titanium-based metal-organic framework modified GCE (Ti-MOF/GCE). The findings demonstrated a notable enhancement in the oxidative peak current on the Ti-MOF/GCE electrode, attributed to the superior conductivity of the MOF material. The optimization experiments revealed that a pH of 4.5, a deposition potential of -1.2 V, and a deposition duration of 60.0 sec were the optimal parameters for accurately identifying the analyte. The study conducted simultaneously investigated the concentration range of 5.0 µg/L to 25.0 µg/L for Pb(II) and Cd(II) and discovered a positive correlation between the

peak current and the concentration level. The LOD for Cd(II) was found to be 0.059 µg/L, whereas for Pb(II) it was established to be 1.02 µg/L, while the LOQ for Cd(II) was found to be 1.98 µg/L, whereas for Pb(II) it was established to be 3.42 µg/L. The Ti-MOF/GCE demonstrates high sensitivity and selectivity for detecting Pb(II) and Cd(II) ions, even in the presence of high quantities of interfering ions including Cl^-, NO_3^-, F^-, Mg^{2+} and Ca^{2+}. The GCE coated with Ti-MOF demonstrated significant efficacy in the analysis of Pb(II) and Cd(II) in real water samples. Therefore, the Ti-MOF generated GCE demonstrates significant promise and advantageous attributes as electrodes for the accurate and efficient detection of Pb(II) and Cd(II) in aqueous solutions. Moreover, it could have wider use in the development of compact technology.

Electrochemical low-level determination of CFX and CBZ were conducted by Zr-MOF/GCE using DPASV. The electrooxidation of CFX and CBZ occurred at *Ca.* 0.27 V and 1.2 V, respectively. Optimization experiments show that pH 7.0, deposition potential -0.2 V, and deposition time 150.0 sec for CFX were the suited parameters for efficient determination of the analyte. While pH 7.0, deposition potential -1.1 V, and deposition time 120.0 sec was the suited parameter for CBZ analysis. The concentration study from 10.0 µg/L to 250.0 µg/L of CFX shows an increase in peak current with an increase in concentration and obtain a LOD of 0.25 µg/L. Whereas, CBZ shows an increase in peak current with an increase in concentration with the LOD of 0.34 µg/L. In the presence of high concentrations of interfering ions such as Cl^-, NO_3^-, F^-, Mg^{2+}, Pb^{2+}, Cu^{2+}, Ca^{2+} and As^{3+}, Zr-MOF/GCE show sensitivity and selectivity toward CFX and CBZ. Reproducibility and stability study show Zr-MOF/GCE long-term stability and repeatability till 168 hrs. The fabricated GCE with Zr-MOF showed practical implacability in the real water samples (groundwater water) for CFX and CBZ analysis. Therefore, Zr-MOF fabricated GCE shows potential and promising electrodes in the trace and efficient detection of CFX and CBZ in aqueous media and possibly a more extensive application in miniature device development.